POWER SYSTEM DYNAMIC MODELING AND SYNCHROPHASOR MEASUREMENTS

BY

KARL E. REINHARD

DISSERTATION

Submitted in partial fulfillment of the requirements
for the degree of Doctor of Philosophy in Electrical and Computer Engineering
in the Graduate College of the
University of Illinois at Urbana-Champaign, 2017

Urbana, Illinois

Doctoral Committee:

Professor Peter Sauer, Chair
Professor Thomas Overbye
Professor William Sanders
Associate Professor Alejandro Domínguez-García
Assistant Research Scientist Katherine Davis

Abstract

Electric power is fully interwoven into the fabric of American life. Its loss for extended periods has profound impacts upon public safety, health and welfare. The power system has been termed the most complex machine built by man. Not surprisingly, the measures to address the range of power system downtime causes are as diverse as the causes themselves. One important arc of effort is providing power system operators with full knowledge of the system's operating state, timely warning when changing conditions threaten system stability, and tools guiding control actions to maintain stable operations.

This research is motivated, in part, by the need to explore opportunities for leveraging nascent synchrophasor data streams against known power system stability challenges. Over the past half-decade, power system operators have aggressively installed large networks of phasor measurement units (PMUs) and phasor data concentrators (PDCs) across the United States and Canada. Today, the synchrophasor data network has reached a state of maturity that opens the door to useful application.

This dissertation investigates power system stability along three lines of effort. The first two efforts address steady-state power system stability – specifically methods for assessing system vulnerabilities arising from the phase angle difference between two buses connected by a transmission line. The third effort investigates the information that can be gleaned from synchrophasor measurements during a system's dynamic system response to changing system conditions.

The first line of investigation extends steady-state distribution factor theory. Distribution factors are computed from a known non-linear power system load flow solution. They

provide a computationally light method for estimating new system conditions under different operating circumstances. Distribution factors are extremely useful for very rapidly screening the impact of unexpected changes in power system configuration – e.g. a transmission line dropping out of service due to environmental conditions. The Line Outage Angle Factor (LOAF) developed herein provides a method for fast computation of bus voltage angle changes after a line outage. The Line Outage Generator Factor (LOGF) modifies the simulated circuit topology to include synchronous machine transient reactances, enabling rapid screening of operating states in which line opening (or re-closure) risks damaging equipment. The LOAF and LOGF provide promising results in MATLAB simulation of the Western System Coordinating Council 3-Machine, 9-Bus System.

The second investigative line seeks to develop a Thevenin equivalent model to be used in tandem with synchrophasor data streams to provide real-time bus angle difference information for buses connected by a transmission line. The appeal is that real-time bus angle difference information could be computed on-site and very rapidly – and significantly, independent of other network bus measurements. The results show that developing a Thevenin equivalent that provides a useful angle difference measure often works well on paper, but is challenging using actual synchrophasor data. Efforts to develop a Thevenin equivalent using Monte Carlo methods show promise, but require further investigation.

The third line of effort shifts to investigate the useful information that a PMU can produce during a power system disturbance event. A synchrophasor is defined at a specific frequency, i.e. the system steady-state operating frequency. Thus a PMU produces a data stream recording power system changes progressing slower than the nominal system frequency; consequently, this is an "off-label" synchrophasor data application. The test system is a generator with electrical and mechanical controls connected by a pair of identical transmission lines to an infinite bus. The synchronous generator is modeled as a three-damper-winding synchronous machine. A MATLAB simulation was written to simulate both the full 14 dynamic state and the reduced order 11 dynamic state system models.

A Real-Time Digital Simulator (RTDS) simulation emulating the test system provides the capability to produce real-time analog generator terminal waveforms to be sampled by a commercial off-the-shelf PMU to produce synchrophasor data. We find that the RTDS generated synchrophasor data stream is similar to the MATLAB reduced order model voltage and current generator terminal data in the *dqo* reference frame – reflecting parallel, but distinct, filtering processes.

In Memory of Sally Reinhard – Loving Wife and Dear Friend

Acknowledgments

Pursuing a PhD in Electrical Engineering is a monumental undertaking – and I did not do it on my own.

I owe an immense debt of gratitude to Professor Peter Sauer as my adviser and mentor over the course of my PhD studies that began in 1998. I greatly admire the depth of his engineering insights and his extraordinary leadership. He is a problem solver, patient, and unflappable. He smiled at me every time that I entered his office – a leadership lesson that has served me well.

He encouraged me to break from my PhD studies in 2000 to command the 3d Ordnance Battalion (Explosive Ordnance Disposal) – in his words, "a once in a lifetime opportunity – a PhD can be completed any time." He encouraged my return upon my Army retirement – and supported me through Sally's battle with cancer.

I was privileged to study under and with accomplished scholars including Professors Bill Sanders, Tom Overbye, Alejandro Domínguez-García and others both in the Power and Energy Systems group and DOE's Trustworthy Cyber Infrastructure for the Power Grid (TCIPG) and Cyber Resilient Energy Delivery Consortium (CREDC) projects. Thanks to Prosper Panumpabi, ITI's Testbed/RTDS engineer, for working with me to get my RTDS simulation up and running.

The Power and Energy Systems support staff – Kevin Colravy, Joyce Mast, and Robin Smith – provided exceptional support... and many great conversations. The ECE Machine shop – Scott McDonald, David Switzer, Greg Bennett, Skee Aldrich and Glen Hedin – did amazing work with a smile in support of my Engineering Open House projects over six and

a half years.

Thanks to my student colleagues over nearly eight years who are too numerous to name individually.

Thanks to my sons Shawn and Drew. And finally, thanks to Sally for her encouragement through 30 years ... I could not (and would not) have done it without her blessing and support. I regret that she did not see the crowning achievement.

Table of Contents

Chapter 1

Introduction

This dissertation investigates power system stability on three lines of effort. The research is motivated, in part, by the need to find new opportunities for leveraging nascent synchrophasor data streams against known power system stability challenges. The first two efforts address power system steady-state stability – specifically methods for assessing system vulnerabilities arising from the phase angle difference between two buses connected by a transmission line. The third effort investigates the information that can be gleaned from synchrophasor measurements during a system's dynamic system response to changing system conditions. These opportunities emerge as reliable and widespread synchrophasor data streams have become a reality. Over the past half-decade, power system operators have aggressively installed large networks of phasor measurement units (PMUs) and synchrophasor data concentrators across the United States and Canada. Today, the synchrophasor data network has reached a state of maturity that opens the door to useful application.

In steady-state, a power system is, broadly speaking, "stable" when the bus voltage angle difference between two buses connected by a transmission line is less than 90 degrees. To assure power system stability, system operators establish and enforce operating policies that sharply limit permissible operating bus voltage angle differences between buses connected by transmission lines – typically no greater than 45 degrees. These operating policies provide conservative operating safety margins designed to avoid system collapse consequent to the confluence operating conditions and events that unexpectedly push the system beyond stability limits.

The first line of investigation (Chapter 3) extends steady-state distribution factor theory.

Distribution factors are computed from a known non-linear power system load flow solution. They provide a computationally light method for estimating new system state under different (but not radically different) operating conditions. Distribution factors are extremely useful for very rapidly screening the impact of unexpected changes in power system configuration – e.g. a transmission line dropping out of service due to environmental conditions. The Line Outage Angle Factor (LOAF) developed herein provides a method for fast computation of bus voltage angle changes after a line outage.

The second line of investigation (Chapter 4) seeks to develop a Thevenin equivalent model to be used in tandem with synchrophasor data streams to provide real-time bus angle difference information for buses connected by a transmission line. The appeal is that real-time bus angle difference information could computed on-site and very rapidly – and significantly, independent of other network bus measurements. In contrast, the power system control center currently relies heavily upon a computationally intense state estimator solution incorporating hundreds or thousands of field measurements.

The third line of investigation (Chapter 5) shifts to power system dynamic response to a disturbance event. Specifically, this investigative effort pursues insights into the information that synchrophasor data streams can provide about dynamic behavior during the transition between steady-state operating conditions. This is an "off-label" synchrophasor data application. A synchrophasor is defined at a specific frequency, i.e. the system steady-state operating frequency. In contrast, voltage, current, and power measurements between equilibrium states are not periodic and as such do not have a well-defined, dominant fundamental frequency foundational to the phasor construct. However, synchrophasor data streams are being applied to system modeling and identification – hence, this effort investigating unforeseen possibilities to leverage existing data streams to good ends.

The "test system" is a synchronous generator connected to an infinite bus by a pair of identical transmission lines; the disturbance event occurs when one transmission line is suddenly opened. We developed MATLAB and Real-Time Digital Simulator (RTDS)

simulations to investigate the test system. The MATLAB simulation is entirely our own work leveraging MATLAB tools – as such, we had complete control and knowledge of the code's inner workings. The MATLAB simulation is completely digital. The RTDS simulation draws upon RTDS provided component simulation modules for the synchronous generator, buses, transmission lines, etc. The RTDS simulator provided the capability to produce real-time analog terminal waveforms to be sampled by a commercial-off-the-shelf (COTS) PMU to produce synchrophasor data; the Schweitzer Engineering Laboratory's SEL-421 Protection, Automation, and Control System, with built-in PMU functionality was integrated into the "test system." The RTDS simulator down-side is that the component simulation modules are in many respects "black boxes" with internal processes opaque to the user. Using the MATLAB and RTDS simulations in parallel provided the opportunity to simulate the "test system" during a disturbance, sample the RTDS-produced analog signal, generate COTS quality synchrophasor data, cross-check the simulation produced information, and ultimately investigate the value of synchrophasor data produced during a system disturbance.

The balance of Chapter 1 provides power system contextual information, an introduction to the phasor measurement unit (PMU), synchrophasor data (SynchDat), and a survey of relevant technical literature.

1.1 The Vulnerable Power System

Electric power is fully interwoven into the fabric of American life, and its loss for extended periods has profound impacts upon public safety, health and welfare. Stable power operation is not a given. On August 14, 2003, eight states (mid-western and northeastern) and eastern Canadian provinces experienced a major blackout, which affected 50 million people. Power in the United States was not fully restored for four days and more than a week in portions of Canada. Estimated costs ranged $6-12 billion. The US-Canadian System Outage Task Force found a series of systemic issues including communications, situational awareness, and

power system control among others that, in combination, contributed to the cascading power failure [1].

The estimated direct and indirect costs of power outages in 2002 were on the order $79 billion – approximately one-third the estimated electric industry revenue of $250 billion [2].[1] Power system conditions contributing to looming reliability challenges include:

- Aggravated grid congestion as demand increases without concomitant increases in generation or transmission capacity – largely due to public resistance and concerns.
- Large energy transfers over very long distances, which are driven, in part, by energy markets resulting from power system deregulation aimed at reducing energy costs.
- Market forces consolidating energy operators and creating larger, more complex operating systems.
- The increased use of wind and solar energy sources which are significantly less reliable due to the wind's unpredictable behavior and climate and variable sunlight [3].

Clearly, electric power system availability, reliability, and resiliency are vital national interests. In 2007, the United States enacted the Energy Independence and Security Act (EISA), which mandated modernizing the nation's electric power infrastructure. The initiative has become commonly known as the "Smart Grid." The following provisions, extracted from Section 1301 [4], highlight key objectives and constraints:

> It is the policy of the United States to support the modernization of the Nation's electricity transmission and distribution system to maintain a reliable and secure electricity infrastructure that can meet future demand growth and to achieve each of the following, which together characterize a Smart Grid:
>
> (1) Increased use of digital information and controls technology to improve reliability, security, and efficiency of the electric grid.

[1] The LaCommera and Eto study [2] estimated the cost to be $79B, but as high as $135B or as low as $22B depending upon the underlying sensitivity assumptions.

(2) Dynamic optimization of grid operations and resources, with full cyber-security.

(3) Deployment and integration of distributed resources and generation, including renewable resources.

(4) Development and incorporation of demand response, demand-side resources, and energy-efficiency resources ....

In its 2009 "Report to the NIST (National Institute Standards and Technology) on the Smart Grid Interoperability Standards Roadmap"[5], the Electric Power Research Institute (EPRI) noted broad Smart Grid stakeholder benefits as follows:

- Consumers enabled to balance their energy consumption with the real-time supply of energy. Variable pricing will provide consumer incentives to install their own infrastructure that supports the Smart Grid. Smart grid information infrastructure will support additional services not available today.

- Utilities enabled to provide more reliable energy, particularly during challenging emergency conditions, while managing their costs more effectively through efficiency and information.

- Society has improved power reliability for governmental services, businesses, and power-outage sensitive consumers. Renewable energy, increased efficiencies, and Plug-In Electric Vehicle (PEV) support will reduce environmental costs, including carbon footprint.

The U.S. electricity industry invested an estimated $18 billion in smart grid technologies in the four year period spanning 2010 to 2013 [6]. In 2011, EPRI estimated that the net investment to realize the envisioned power delivery system (including transmission, distribution, and consumer sub-systems) would approach $500 billion over 20 years [7].

The dollars and numbers of devices are seemingly large, yet represent a modest first step to modernizing the full power infrastructure valued at more than $1 trillion. Additionally,

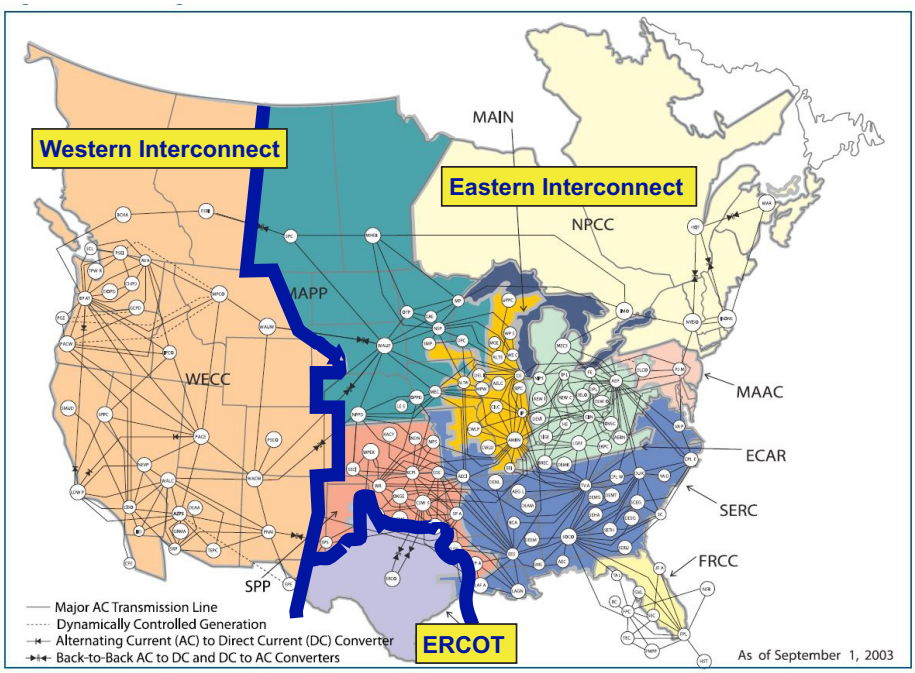

Figure 1.1: North American interconnections and major connecting transmission lines. The U.S. and Canada have charged the North American Electric Reliability Corp. and its 10 regional reliability entities (shaded) with responsibility for assuring power grid reliability. [1].

this list of investments does not adequately convey the undertaking's complexity. The electric power grid's infrastructure comprises over 17,000 power generation plants generating nearly 100,000 MW, 200,000 miles of transmission lines, 3,500 utility organizations, and 100 million customers [1].

As reflected in Fig. 1.1,[2] the United States has three distinct power grids – the Western, Eastern, and ERCOT interconnections. In each interconnection, all generators, transmission lines, and customers are interconnected in vast multi-state networks. These distinct power grids are tied by direct current transmission lines that allow power sharing between the interconnections. The law of conservation of energy requires that at each instant in time the energy generated equal the energy consumed, less transmission losses and comparatively inconsequential amounts of stored energy. Consequently, the electric power system is constantly adjusting the power generated to meet customer power demand. The system

[2]Adapted from Fig 2.6 of [1] by overlaying the interconnect boundaries

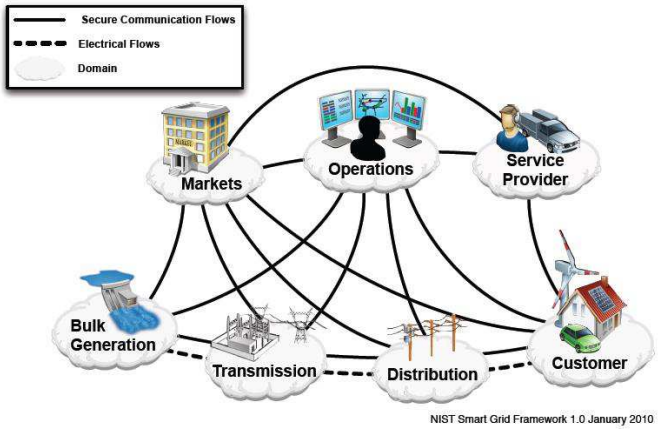

Figure 1.2: Power system's major conceptual actors and their inter-relationships [8].

is mathematically non-linear and consequently is computationally intensive to model in the steady-state. Dynamic system behavior is significantly more difficult to model, especially in real time, when a significant disturbance occurs. The high power system reliability that Americans experience and, indeed, expect is a result of intense and constant management. Power system availability, reliability, and resiliency depend upon an extensive portfolio of generation assets and reserve generation capacity to meet customers' continually changing demand. The generation portfolio contains capital assets – that are very costly to build, maintain, and operate; reserve capacity maintained in the margins waiting for demand spikes or system node failures is also very expensive. The smart grid initiative is intended to strengthen reliability while cutting costs, reducing requirements for costly reserve capacity, improving energy efficiency, and conserving the environment [1]. A significant challenge is balancing the often conflicting goals of availability, high reliability, and low cost.

1.2 Conceptual Power System Control in Brief

The reliable operation and control of the existing electric power system is highly dependent upon a complex network of computer, software, and communications technologies; Fig. 1.2 provides a visual representation of the key domains. This system of control and communications is often referred to as the energy management system (EMS). The EMS rides

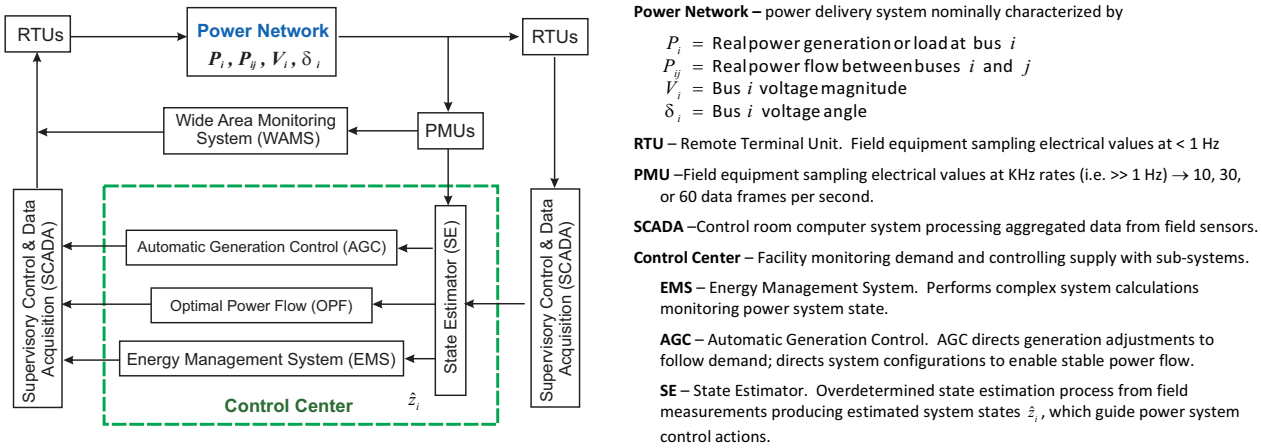

Figure 1.3: Power network schematic diagram depicting the relationships between the power system, field sensors and the System Control and Data Acquisition System (SCADA). Adapted and re-purposed from a Fig. 1 in [9].

on the backbone of existing communications systems including the internet, commercial-off-the-shelf (COTS) computer hardware and software systems. Power grid modernization will require significantly expanding the numbers of sensors, communications paths, and automatic control systems, with a corresponding increase in system complexity. With complexity, additional system vulnerabilities to operational failure, natural forces, and malicious attack emerge that demand accurate and timely knowledge of the system's physical state to avoid interruptions.

The power system schematic diagram (Fig. 1.3) provides context for the overall power system control structure. The control center uses State Estimator (SE), EMS, and Automatic Generation Control (AGC) sub-systems to make and implement control system decisions. The system relies upon a variety of two-way communication channels between distributed sub-control centers and the main control system.

The power system is controlled via a series of interconnected feedback loops. System operators adjust control parameters based upon field measurements. Prior to the widespread fielding of phasor measurement units (PMUs), voltage and current measurements were typically collected no faster than once per second and without precise interconnect-wide measurement time synchronization. The American Reinvestment and Recovery Act of 2009

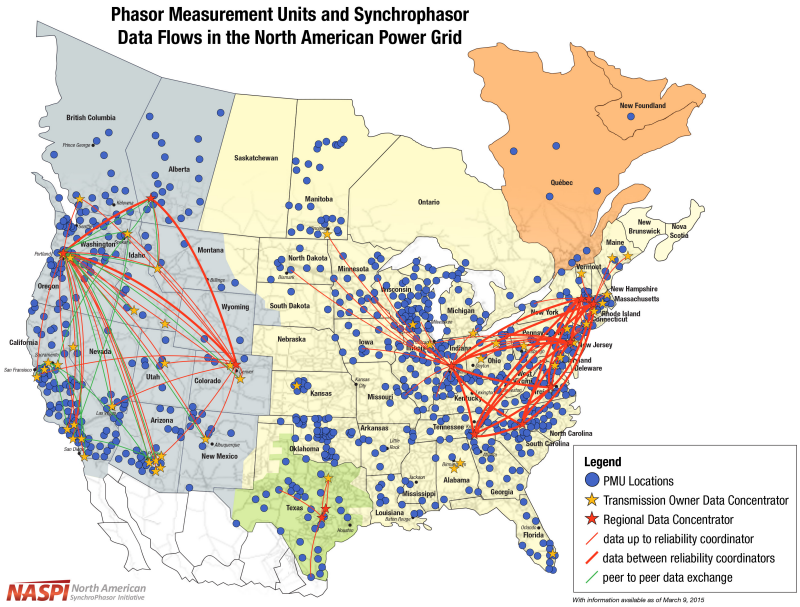

Figure 1.4: Phasor measurement units in the North American power grid, March 2015 [10].

stipulated $330 million in public and private investments to expand PMU installations from less than 200 in 2009 to more than 1700 in 2015 [6]. PMU locations and major synchrophasor data flows as of March 2015 are depicted in Fig. 1.4.[3] PMUs provide system state measurements up to 100 times faster than legacy sensors, opening possibilities for significantly improved power system control.

1.3 The Phasor Measurement Unit

The PMU is a physical instrument that samples currents and voltages at sub-second interval and computes time-stamped synchrophasor data at a field location. A typical PMU internal component diagram is shown in Fig. 1.5. PMUs sample voltage and current magnitudes at rates on the order of 100 times the nominal system frequency (60 Hz in North America, 50 Hz on other systems).

The conceptual relationship between the nominal power line signal and its phasor repre-

[3]Courtesy of the North American SynchroPhasor Initiative (www.naspi.org) and the U.S. Department of Energy.

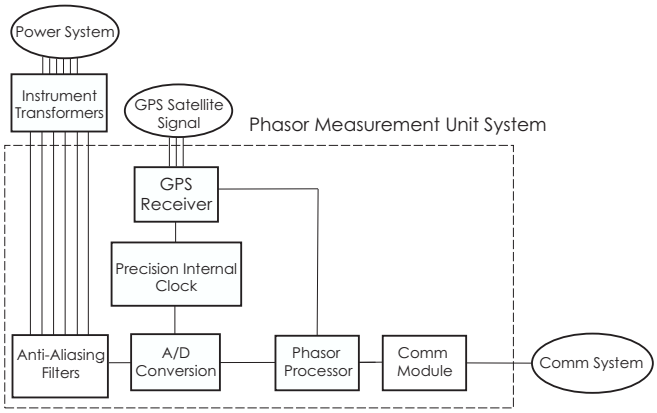

Figure 1.5: Phasor measurement unit (PMU) component diagram.

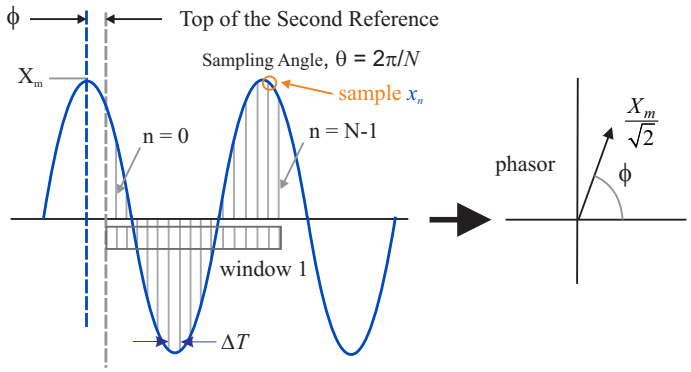

Figure 1.6: Phasor representation of a periodic signal.

sentation is illustrated in Fig. 1.6. The PMU samples a continuous and (ideally) sinusoidal power transmission waveform and computes a phasor that accurately characterizes the waveform by its magnitude and phase at the system's nominal frequency. A continuous sinusoidal signal can be represented

$$x(t) \quad = \quad X_m \cos(2\pi f_o t \ + \phi)$$

where

X_m = peak signal magnitude $\qquad\qquad$ ϕ = phase angle

f_o = fundamental frequency (60 Hz)

The signal is sampled N times over a data window (i.e. sampling period) such that the Nyquist criterion is satisfied. The signal's complex phasor representation is

$$X_k = \frac{\sqrt{2}}{N} \sum_{n=0}^{N-1} x_n \{\cos(k\, n\theta) - j \sin(k\, n\theta)\}$$

where

$n =$ sample number $\qquad N =$ number of samples

$x_n =$ sample value $\qquad \theta = \dfrac{2\pi}{N}$, sampling angle

$k = 1$ is the first harmonic (60 Hz)

with constituent cosine and sine sums

$$X_{1\,\cos} = \frac{\sqrt{2}}{N} \sum_{n=0}^{N-1} x_n \cos(1\, n\theta)$$

$$X_{1\,\sin} = \frac{\sqrt{2}}{N} \sum_{n=0}^{N-1} x_n \sin(1\, n\theta)$$

that, in-turn, define the phasor [4]

$$\begin{aligned} \mathbf{X}_1 &= X_{1\,\cos} + jX_{1\,\sin} \\ &= \sqrt{X_{1\,\cos}^2 + jX_{1\,\sin}^2} \angle \arctan\left(\frac{-X_{1\,\sin}}{X_{1\,\cos}}\right) \\ &= \frac{X_m}{\sqrt{2}} \angle \phi \end{aligned}$$

From the sample data window, the PMU applies signal processing algorithms to compute voltage and current phasors (magnitude and phase angle) and actual system frequency referenced to the Global Positioning System (GPS) top-of-the-second timing signal, which

[4] This notation and phasor definition are adapted from Phadke and Thorp [11] and IEEE Standard C37.118.1-2011[12].

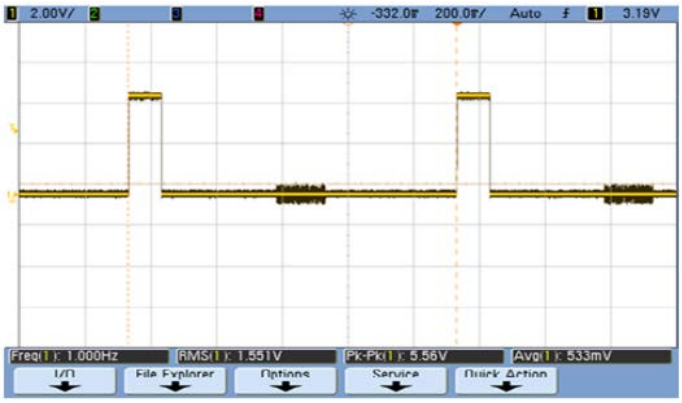

(a) Oscilloscope trace of the GPS timing signal; two one-second pulse cycles are shown. The leading edge of each pulse marks the "top of the second" with accuracy exceeding 1 μs.

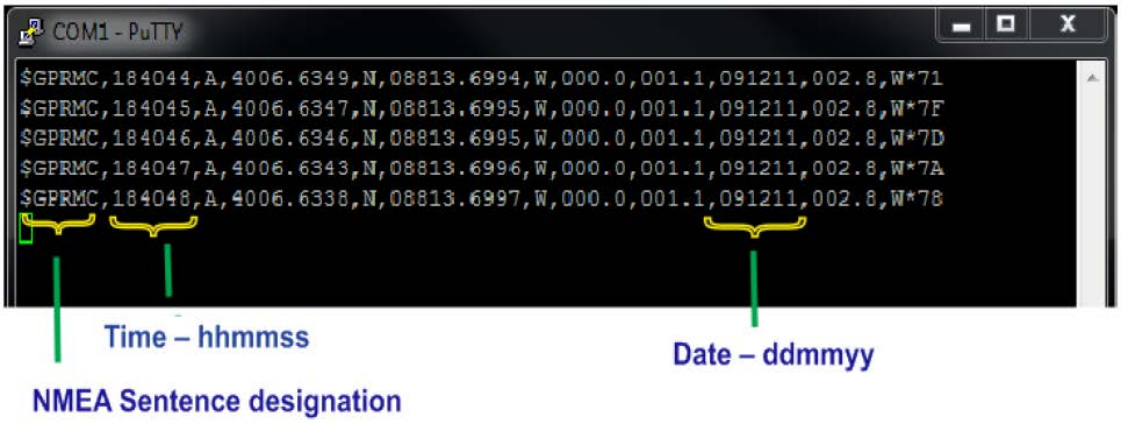

(b) Sample GPS textual data embedded in each pulse in National Maritime Electronics Association (NMEA) sentence format. This data uniquely identifies the pulse and is incorporated into each synchrophasor data measurement frame. The PMU tracks time between pulses and adds sub-second time information to each data frame.

Figure 1.7: Screen-captured images of the Global Positioning System (GPS) timing signal.

is accurate to better than 1 μs. The leading edge of each signal pulse marks the top of each second (see Fig. 1.7a). The GPS signal includes an embedded text string that labels the date and time of each timing pulse (see Fig. 1.7b). From this information, the PMU generates sub-second time stamps for each synchrophasor computed between the tops of sequential seconds. These very precise time stamps enable aggregated data from PMUs separated by thousands of miles to be assembled into snapshots having microsecond level precision. By definition, the phasor is referenced to the nominal system frequency and is a measure of the

power system's steady-state; synchrophasor measurements are produced at standard, user selectable rates tied to the nominal system frequency – e.g. 10, 30, or 60 synchrophasor measurements per second. Each measurement is reported as a "data frame" that includes synchrophasor, frequency, and rate of change of frequency measurements corresponding to a single time-stamp.[5]

The process that produces a synchrophasor measurement focuses narrowly upon producing a very precise steady-state measure compressing several thousand sample measurements into the handful of magnitude, phase and frequency values contained in a synchrophasor measurement. The data winnowing process starts with an analog low-pass filter before sampling that removes frequency components that are more than half the sampling rate to preclude data aliasing. After sampling, the data is further filtered by digital filters to facilitate synchrophasor accuracy. These filtering stages, by their very nature, discard information relevant to transient phenomena in the power system.

The PMU streams synchrophasor measurements to phasor data concentrators (PDCs) which receive, process, and forward information from multiple PMUs to control centers, which may occur via multiple hierarchical PDCs (see Fig. 1.8). The precise time-stamps are essential to synchronizing data from widely dispersed locations to enable the rapid and accurate calculation of the system-wide state with microsecond timing precision [13]. This collection of sensors, data concentration, and information transmission networks is often referred to as a wide area measurement system (WAMS). Widespread PMU deployment enables monitoring:

- Phase and power angle.
- System oscillations that develop and potentially threaten system stability.
- Voltage stability.
- Line thermal conditions.

[5] "Data frame" is a specialized term defined in section 3.2, IEEE Standard C37.118.1-2011[12]

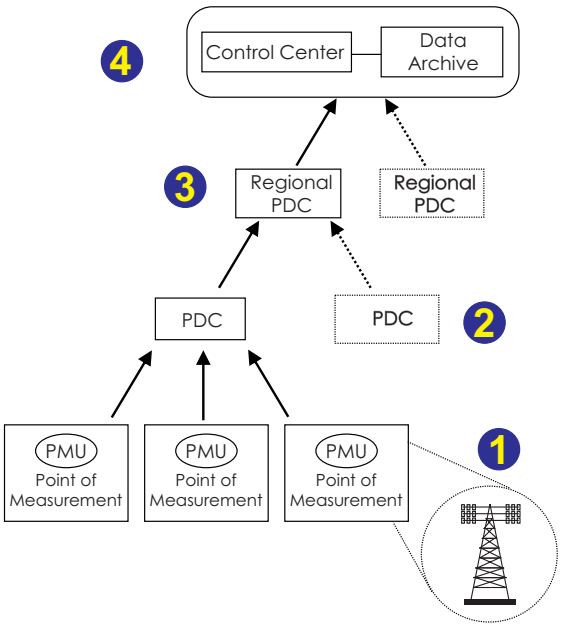

Figure 1.8: Synchrophasor data network from point of measurement to the control room. Conceptually, level 1 is the point of measurement. Levels 2 and 3 are phasor data concentrators (PDCs) that aggregate data from multiple PMUs. Level 4 is the control center that uses and archives aggregated synchrophasor data.

These capabilities improve the fidelity and reliability of the control center's awareness of the system's actual operating state, especially under stressed conditions [3]. Real (or near-real-time) time power system state estimates enable timely operational adjustments and system reconfigurations.

1.4 Synchrophasor Data Applications to Modeling

First, this investigation examines using synchrophasor data directly to assess system-wide power system stability from local measurements and computations. Conceptually, this assessment would use local synchrophasor data and computations at key points in the system to generate warnings to system operators of conditions threatening stable system operation. This is a departure from the traditional system-wide power flow analysis dependent on fused synchrophasor data from across the system – a computationally intense undertaking involving all system buses and transmission lines. Very fast local computations flagging sta-

bility threatening conditions would alert operators sooner, giving them more time to adjust operating conditions to avert power interruptions.

Second, this work investigates the utility of using synchrophasor data to capture transient system behavior between significantly different equilibrium states. In both system dynamic behavior analysis and real-time control, there are a number of issues to be investigated regarding the utility of synchrophasor data produced by PMUs. By design, the PMU produces phasor values (magnitude and phase) at the system's nominal frequency (50 or 60 Hz). The synchrophasor computation process by its very nature "discards" information available from the sampled data. First, the data produced by the PMU when the system is not operating at or near the fundamental frequency is not a "phasor"; rather, it is a number generated by an algorithm set to process measurements at the system's operating frequency. That being said, the data produced under dynamic conditions may still be useful if interpreted properly. Second, the sampled voltage and current values are altered from the point of measurement by bandwidth-limited step-down transformers (i.e. current and potential transformers) and the digital filters that condition data prior to phasor computation. These "filters" eliminate useful information occurring at frequencies other than the fundamental. This is particularly important under dynamic conditions which may have high frequency content discarded during filtering processes.

1.5 Literature Review

1.5.1 Distribution Factors

In the early 1960s, the five member companies of the Pennsylvania - New Jersey - Maryland Interconnect (currently known as PJM) chartered a task force to develop a computationally fast method for efficiently estimating power flow changes due to (1) changes in generation and (2) out-of-service transmission lines. The "distribution factors" technique required a full power load flow "base case" solution. The linear distribution factors derived from the non-

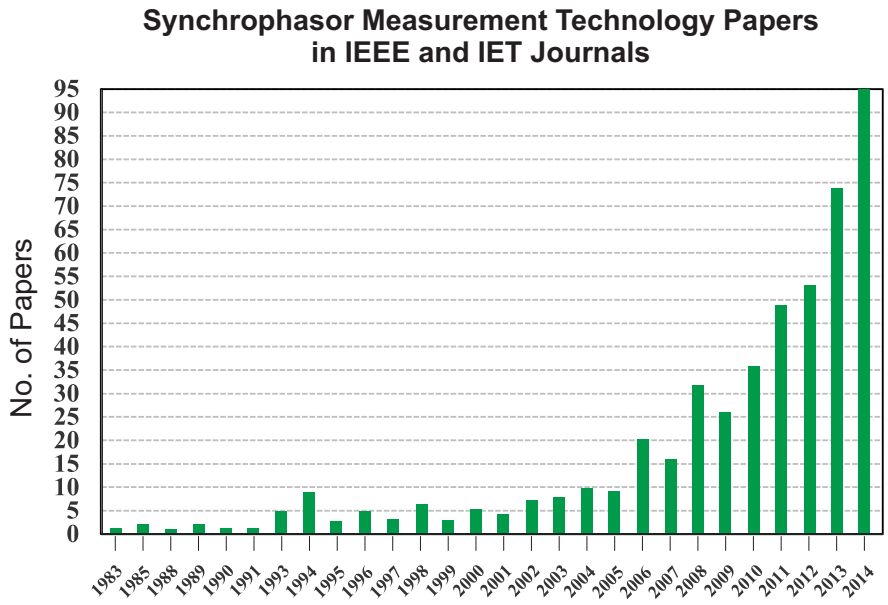

Figure 1.9: Distribution synchrophasor data and network technical papers in Institute of Electrical and Electronics Engineers (IEEE) and Institution of Engineering and Technology (IET) journals 1983-2014 [19].

linear model were then used to estimate power flow changes from the "base case" solution in much the same way that current dividers are used. This fast contingency screening method showed excellent agreement with full load flow studies [14]. As reported by Sauer, the distribution factor method was both applied extensively and extended to other power system quantities over the following 20 years; his paper extended the mathematical foundation by referencing the distribution factors to the swing bus and arbitrary ground tie modifications [15]. Wood and Wollenberg provide a comprehensive development of distribution factors using progressive modeling simplifications from the full (and non-linear) load flow model to the linear DC power flow model [16]. The recent widespread installation of PMUs has prompted efforts to compute distribution factors from synchrophasor data; this opens the door to computing distribution factors from real-time field data independent of a power flow model solution [17, 18].

1.5.2 Synchrophasor Measurements

The synchrophasor data "system" (nominally including phasor measurement units, phasor data concentrators, network communications, and control center applications) has amassed a sizable body of technical literature since concept proposal and initial development in the early 1980s. Arun Phadke and James Thorp shepherded early PMU development at Virginia Polytechnic Institute merging computer relay and GPS technologies [20]. The comprehensive starting point for understanding synchronized phasor measurements is their 2008 book that assembles more than 20 years of research in a coherent and comprehensive presentation [11]. In 2015, Farrokh Aminfar et al. [19] published a comprehensive literature review that cataloged over 470 synchrophasor measurement technology (SMT) related articles published in 32 Institute of Electrical and Electronics Engineers (IEEE) and Institution of Engineering and Technology (IET) journals between 1983 and 2014. As with many emerging technologies, the distribution of synchrophasor papers over this period resembles exponential growth as evident in Fig. 1.9. The review organized the articles into nine categories with the number of articles in parenthesis.

1. SMT algorithms, PMU design, and WAMS structure (135)
2. General SMT, PMU, and WAMS technology overviews (43)
3. PMU placement (55)
4. State estimation using synchrophasor data (45)
5. Model validation, calibration, and extraction (22)
6. Fault/event detection and location (39)
7. WAMS-based dynamic/stability monitoring and prediction (77)
8. WAMS-based control strategies (45)

9. WAMS-based protection schemes (29)

Categories one and five are most relevant to the research lines reported herein. The number of papers published since 2014 continues at the same pace or better.

Thevenin Equivalent Representations

A power system Thevenin equivalent using synchrophasor terminal measurements at one or both ends of a connecting transmission line was reported in [21] for characterizing transmission line loadability limits using numerical techniques, which inspired this work investigating a Thevenin equivalent based upon synchrophasor data. The proposal's novelty prompted a search for Thevenin equivalent theoretical underpinnings and assumptions [22, 23, 24, 25]. Several papers providing perspective on potentially useful mathematical tools including system identification [26], least squares estimation techniques [27, 28], and singular value decomposition [29].

As previously referenced, synchrophasor data is proposed as a means to locally compute distribution factors [17, 18]. The other papers with an intersection of synchrophasor data and Thevenin models addressed either voltage stability or the related challenge of maximum power transfer. The papers addressing voltage stability subdivided into two groups. The first group proposed Thevenin equivalents to model a local bus or device for voltage control or load shedding [30, 31, 32]. The second group proposed Thevenin equivalents to represent the power grid for evaluating local bus performance including generators; these used different mathematical approaches including algebraic [33], recursive least squares [34], and Kalman filters [35, 36].

Considerable research is being conducted to identify conditions producing erroneous synchrophasor measurements and propose mitigation measures. The papers fell into two categories: errors due to either noisy data or transient conditions. Three papers addressed algorithms intended to reduce noise effects [37, 38] or to improve data conditioning [39]. As synchrophasors are computed at nominal system frequency, the usefulness of synchropha-

sors computed from a sample data set that includes transient values (i.e. non-periodic values that significantly deviate from expected steady-state values) is uncertain. Phadke [40] explores the concepts of synchrophasor data computed under transient conditions and proposes standardization for computations under transient conditions. Two additional papers propose algorithms for detecting faulty synchrophasor data produced during a system transient [41, 42].

Synchronous Machine Transient Response and Synchrophasor Measurements

Synchronous machine dynamic modeling is mature and detailed in several well regarded textbooks [43, 44, 45]. The IEEE has been proactive developing and updating PMU and synchrophasor data standards for more than a decade [12]. The three damper winding model is nominally characterized by 14 dynamic states with dynamic response times including stator transients, shaft speed transients, and governor control spanning many orders of magnitude (10^{-5} to 10^{3} s). For many problems, the very fast transients are not of interest and are eliminated through model reduction. The integral manifold model order reduction techniques described in [46, 47] are widely accepted for power system modeling. Related work includes dynamic model evaluation from disturbance data in general [48] and efforts to validate machine models using synchrophasor data [49].

Chapter 2

Background

2.1 Power Load Flow Modeling

By its nature, controlling the inherently non-linear electric power system is non-trivial. The explanation that follows highlights relevant concepts, but is not a full explanation of solving the power flow problem. Insights into the challenges can be gained by way of a simple example with the widely used Western System Coordinating Council (WSCC) 3-Machine, 9-Bus System (Fig. 2.1). Each voltage-controlled bus is connected to a generator producing real power and reactive power. Power flows to local distribution systems through the remaining six buses. Power transmission lines are identified by bus number pairs, ij. At the i_{th} node, a pair of real and reactive power equations are written

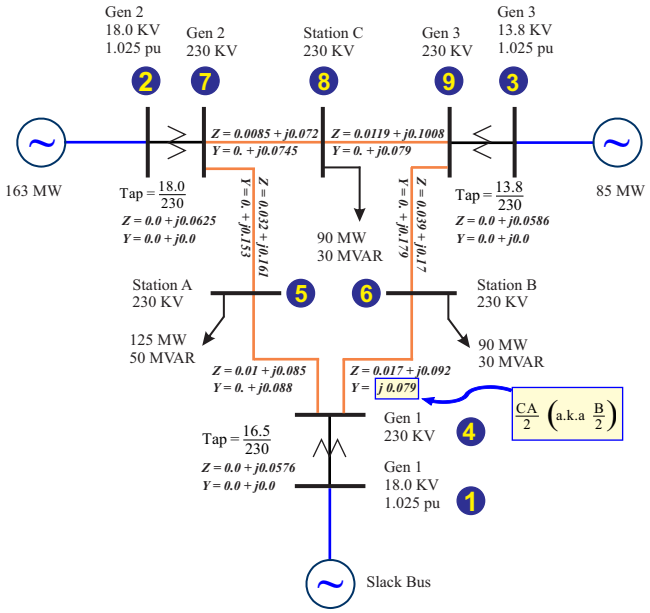

Figure 2.1: Western System Coordinating Council (WSCC) 3-Machine, 9-Bus System.

$$
\begin{aligned}
P_i &= \sum_{j=1}^{N} |Y_{ij}|\,|V_i|\,|V_j|\,\cos\left(\delta_i - \delta_j - \gamma_{ij}\right) \\
Q_i &= \sum_{j=1}^{N} |Y_{ij}|\,|V_i|\,|V_j|\,\sin\left(\delta_i - \delta_j - \gamma_{ij}\right)
\end{aligned}
\tag{2.1}
$$

where

P_i = net power entering the network at bus i from a source external to $\mathbf{Y}$

Q_i = net reactive power entering the network at bus i from a source external to $\mathbf{Y}$

$V_i,\ V_j$ = voltages at buses i and j respectively

Y_{ij} = entry $i\,j$ of $\mathbf{Y}$

γ_{ij} = angle $i\,j$ of $\mathbf{Y}$

$\delta_i\,,\ \delta_j$ = bus voltage angles at buses i and j

The net power and net reactive power at each node are the difference between generated and demanded power

$$
\begin{aligned}
P_i &= P_{gi} - P_{di} \\
Q_i &= Q_{gi} - Q_{di}
\end{aligned}
\tag{2.2}
$$

where

P_{gi} = power generated at bus i

P_{di} = power demanded by customers at bus i

Q_{gi} = reactive power generated at bus i

Q_{di} = reactive power demanded at bus i

Solving the $2N$ equations defining the system is referred to as solving the power flow problem, and is done using matrix solution techniques. For example, the 9-bus power flow test system is characterized by 18 equations. To provide an appreciation of the challenges, a simplified explanation of the system and its solution follows. Note that the equations' cosine, sine, and product terms make the system of equations non-linear; consequently, the system cannot be solved analytically. At each bus, i, four potentially unknown variables exist: real power, P_i; reactive power, Q_i; bus voltage angle, δ_i; and bus voltage magnitude,

$|V_i|$ [50]. At each bus, the number of unknowns is reduced to two by specifying two values, which mathematically allows a solution to be determined. At the load buses, the real and reactive power demands are projected from appropriately adjusted historical experience; hence, the unknown quantities are δ_i and $|V_i|$. At voltage controlled buses (i.e. those with generators), $|V_i|$ and P_i are specified, the load flow solution determines δ_i, and Q_i is computed algebraically from the load flow solution values. Neglecting transmission line resistance, a very useful estimate of real power flow magnitude and direction on transmission line ij is

$$P_{ij} \;=\; \frac{|V_i|\,|V_j|}{X_{ij}} \cdot \sin(\delta_i \,-\, \delta_j\,) \tag{2.3}$$

The power flow problem solution provides an operating point for the system under a specific set of conditions. However, the demand for power is constantly changing across the 24-hour day, during the course of a week, and with changing seasons. At any given instant, the power delivered to customers must precisely match the power generated less losses in the system. Power system operators adjust the system's operating point throughout the day to follow demand. The system's operating point can change dramatically from hour to hour, each new operating point having a different load flow solution. Sudden disturbances or equipment failures can have unforeseen consequences that ripple through the system with unpredictable consequences, including unstable operating states that lead to power outages [51].

Due to its complexity and size, power systems operators have, at present, very limited ability to measure the system's steady state in real time. The system's non-linear nature precludes forecasting the system's dynamic behavior with precision. As a consequence, utility companies operate the power system with a robust safety margin between the operating point and the estimated point at which small disturbances could cause the system to become unstable and collapse, providing the reliable power customers expect. However, as energy and power generation facilities have become more expensive and environmental concerns

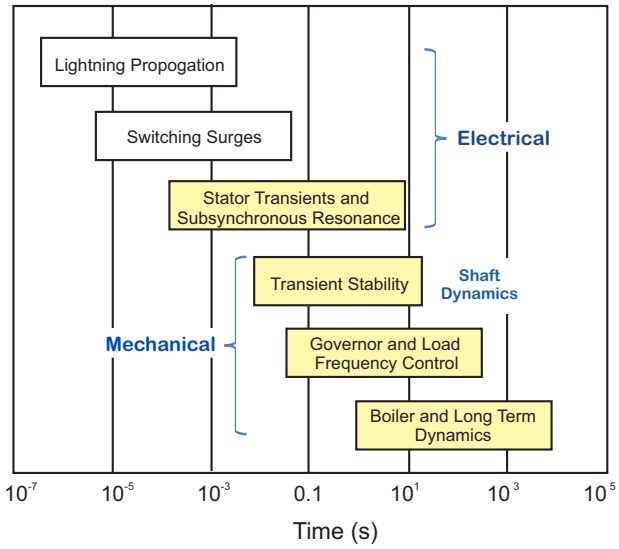

Figure 2.2: Synchronous machine dynamic phenomena time-scales. Adapted from Fig. 1.2 in [43].

have come to the forefront, the public and government are pressing the utilities to cut costs, while maintaining reliability. The smart grid is envisioned as a means to these ends.

2.2 Synchronous Machine Dynamic Modeling

The electric power system is subject to a broad spectrum of disturbance events. As depicted in Fig. 2.2, the transient response periods range from microseconds to hours, spanning 10 orders of magnitude. At one extreme, lightning strikes cause transient phenomena that are measured in microseconds. At the other extreme, mechanical response times are measured in hours. This broad duration range presents demanding modeling and simulation challenges. Comprehensive system models are capable of capturing the full transient phenomena range, but doing so requires very complex models and concomitant computational burden. In many instances, the full range of dynamic response transients is not important to the question at hand; thus, reduced models are chosen to focus on a specific phenomenon or to reduce the computational burden to produce an appropriate "good enough" answer.

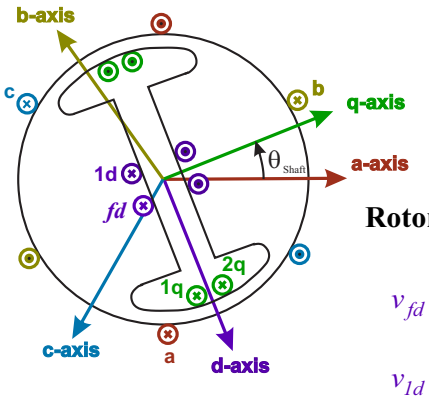

Stator Voltage Eqns

$$v_a = r_s i_a + \frac{d\lambda_a}{dt}$$

$$v_b = r_s i_b + \frac{d\lambda_b}{dt}$$

$$v_c = r_s i_c + \frac{d\lambda_c}{dt}$$

Rotor Voltage Eqns

$$v_{fd} = r_{fd}\, i_{fd} + \frac{d\lambda_{fd}}{dt}$$

$$v_{1d} = r_{1d}\, i_{1d} + \frac{d\lambda_{1d}}{dt}$$

$$v_{1q} = r_{1q}\, i_{1q} + \frac{d\lambda_{1q}}{dt}$$

$$v_{2q} = r_{2q}\, i_{2q} + \frac{d\lambda_{2q}}{dt}$$

Variable	Description
$\lambda_a, \lambda_b, \lambda_c$	Stator winding flux linkage in *abc*
i_a, i_b, i_c	Stator winding currents in *abc*
v_a, v_b, v_c	Stator winding voltages in *abc*
r_s	Stator winding resistance; identical in each phase
$i_{fd}, i_{1d}, i_{1q}, i_{2q}$	Field and *1d, 1q, 2q* damper winding currents
$v_{fd}, v_{1d}, v_{1q}, v_{2q}$	Field and *1d, 1q, 2q* damper winding voltages
$r_{fd}, r_{1d}, r_{1q}, r_{2q}$	Field and *1d, 1q, 2q* damper winding resistances

Figure 2.3: Synchronous generator: 3-damper winding schematic with *abc* frame voltage equations. The equations are colored to correspond with the synchronous machine structures shown in the synchronous machine diagram. Lower case variables signify unscaled values. Adapted from Chapter 3 of [43].

2.2.1 Multi-Time-Scale Model (14th Order)

The three-damper-winding synchronous generator model shown in Fig. 2.3 includes the full range of dynamic time-scales associated with the machine itself. Notice that the stator equations are written in the stationary (*abc*) reference frame, whereas the rotor equations are written in the rotating (*dqo*) reference frame. This and subsequent figures include equations color coded to match the machine feature being modeled. As a matter of computational convenience and with conceptual benefits, common practice is to use the Park transformation to refer the stator equations into the rotating (*dqo*) reference frame. The Park transformation,

denoted $\boldsymbol{T}_{dqo}$, defines the relationship between voltage ($\mathbf{V}$), current ($\boldsymbol{I}$), and flux linkage ($\boldsymbol{\lambda}$) vectors in the *abc* and *dqo* reference frames:[1]

$$\begin{aligned} \mathbf{V}_{dqo} &= \mathbf{T}_{dqo}\,\mathbf{V}_{abc} \\ \mathbf{I}_{dqo} &= \mathbf{T}_{dqo}\,\mathbf{I}_{abc} \\ \boldsymbol{\lambda}_{dqo} &= \mathbf{T}_{dqo}\,\boldsymbol{\lambda}_{abc} \end{aligned} \tag{2.4}$$

where

$$\mathbf{T}_{dqo} = \tfrac{2}{3} \begin{bmatrix} \sin\frac{P}{2}\theta_{shaft} & \sin\left(\frac{P}{2}\theta_{shaft} - \frac{2\pi}{3}\right) & \sin\left(\frac{P}{2}\theta_{shaft} + \frac{2\pi}{3}\right) \\ \cos\frac{P}{2}\theta_{shaft} & \cos\left(\frac{P}{2}\theta_{shaft} - \frac{2\pi}{3}\right) & \cos\left(\frac{P}{2}\theta_{shaft} + \frac{2\pi}{3}\right) \\ \frac{1}{2} & \frac{1}{2} & \frac{1}{2} \end{bmatrix} \tag{2.5}$$

The inverse transform is defined as

$$\begin{aligned} \mathbf{V}_{abc} &= \mathbf{T}_{dqo}^{-1}\,\mathbf{V}_{dqo} \\ \mathbf{I}_{abc} &= \mathbf{T}_{dqo}^{-1}\,\mathbf{I}_{dqo} \\ \boldsymbol{\lambda}_{abc} &= \mathbf{T}_{dqo}^{-1}\,\boldsymbol{\lambda}_{dqo} \end{aligned} \tag{2.6}$$

where

$$\mathbf{T}_{dqo}^{-1} = \begin{bmatrix} \sin\frac{P}{2}\theta_{shaft} & \cos\frac{P}{2}\theta_{shaft} & 1 \\ \sin\left(\frac{P}{2}\theta_{shaft} - \frac{2\pi}{3}\right) & \cos\left(\frac{P}{2}\theta_{shaft} - \frac{2\pi}{3}\right) & 1 \\ \sin\left(\frac{P}{2}\theta_{shaft} + \frac{2\pi}{3}\right) & \cos\left(\frac{P}{2}\theta_{shaft} + \frac{2\pi}{3}\right) & 1 \end{bmatrix} \tag{2.7}$$

and is applied to constitutive parameter matrices such that

$$\begin{aligned} \mathbf{R}_{dqo} &= \mathbf{T}_{dqo}\,\mathbf{R}_{abc}\,\mathbf{T}_{dqo}^{-1} \\ \mathbf{L}_{dqo} &= \mathbf{T}_{dqo}\,\mathbf{L}_{abc}\mathbf{T}_{dqo}^{-1} \end{aligned} \tag{2.8}$$

[1] This is the power-variant formulation, which is the historic industry standard. In the power-invariant formulation, the $\frac{2}{3}$ factor included in T_{dqo} is replaced by the factor $\sqrt{\frac{2}{3}}$ included in both the T_{dqo} and T_{dqo}^{-1} terms; Sect 3.4.8., Alternative Per Unit Systems and Transformations, of [52] provides insights into the trade-offs between the two formulations. Care must also be taken to distinguish the alternate formulation T_{qdo}, which juxtaposes matrix rows 1 and 2.

The constitutive relationship between voltage and resistance in the *dqo* frame is straightforward

$$\mathbf{V}_{dqo} \;= \boldsymbol{R}_{dqo}\, \mathbf{I}_{dqo}$$

The transformation of the constitutive relationship between voltage and flux linkage in the *dqo* frame is more involved due to the derivative operator

$$\begin{aligned} \mathbf{V}_{dqo} &= p\,[\,\boldsymbol{\lambda}_{dqo}] \\ &= \mathbf{T}_{dqo}\; p\left[\mathbf{T}_{dqo}^{-1}\;\boldsymbol{\lambda}_{dqo}\right] \end{aligned} \tag{2.9}$$

where

$$p \;=\; \tfrac{d}{dt}$$

Applying the differentiation product rule yields

$$\mathbf{V}_{dqo} \;=\; \mathbf{T}_{dqo}\;\left[\,p\,\mathbf{T}_{dqo}^{-1}\,\right]\;\boldsymbol{\lambda}_{dqo} \;+\; \mathbf{T}_{dqo}\;\left[\mathbf{T}_{dqo}^{-1}\,\right]\;\; p\,\boldsymbol{\lambda}_{dqo}$$

$$= \quad \omega \begin{bmatrix} 0 & -1 & 0 \\ 1 & 0 & 0 \\ 0 & 0 & 0 \end{bmatrix} \begin{bmatrix} \lambda_d \\ \lambda_q \\ \lambda_o \end{bmatrix} \;+\; p \begin{bmatrix} \lambda_d \\ \lambda_q \\ \lambda_o \end{bmatrix} \tag{2.10}$$

where ω is the rotational speed in radians per second. The term including ω contains "speed" voltage information in the *dqo* reference frame; the time derivative of the flux linkage contains "transformer" voltage information. A convenient property of the normally balanced $\mathbf{R}_{abc}$ and $\mathbf{L}_{abc}$ matrices is that, when referred to the *dqo* reference frame, the $\mathbf{R}_{dqo}$ and $\mathbf{L}_{dqo}$matrices are diagonal. However if either the $\mathbf{R}_{abc}$ or $\mathbf{L}_{abc}$ matrix is unbalanced, the respective $\mathbf{R}_{dqo}$ or $\mathbf{L}_{dqo}$ matrix are not diagonal and the matrix entries are functions of θ_{shaft}.[2] The transformed model with stator variables and equations "referred" to the rotating reference frame is shown in Fig. 2.4.

[2]Chapter 3 of [45] thoroughly develops reference frame theory pertinent to rotating machines.

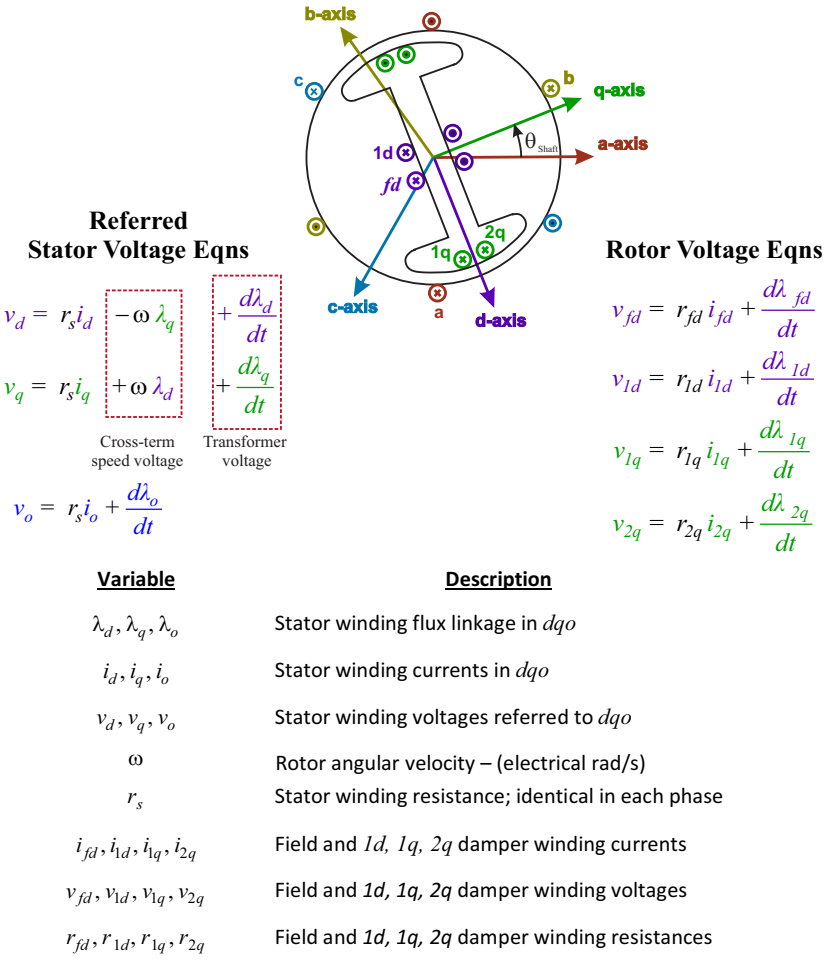

Figure 2.4: Synchronous generator: 3-damper winding schematic with *dqo* frame voltage equations. The stator equations have been referred from the *abc* to the *dqo* reference frame using the Park transformation, and the stator equation color coding changed accordingly. Adapted from Chapter 3 of [43].

A benefit of the *dqo* reference frame dynamic solution is that the system state variables are constant while the system is in steady state, and conversely, the state variables change with time when the system is transitioning between equilibrium states. This point is illustrated in Fig. 2.5 by way of comparing transmission line one 3-phase current flows in the *abc* and *dqo* reference frames, shown in Figs 2.5b and 2.5c respectively. The comparison clearly illustrates the advantage of using the *dqo* reference frame for visualizing transient behavior as transient periods stand out from otherwise constant state variables.

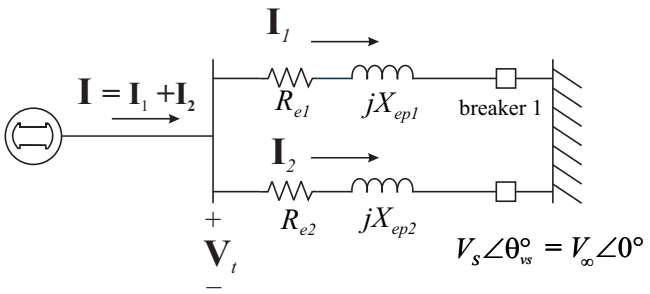

(a) After a trigger signal, breaker 1 opens when phase a crosses through zero the 2d time.

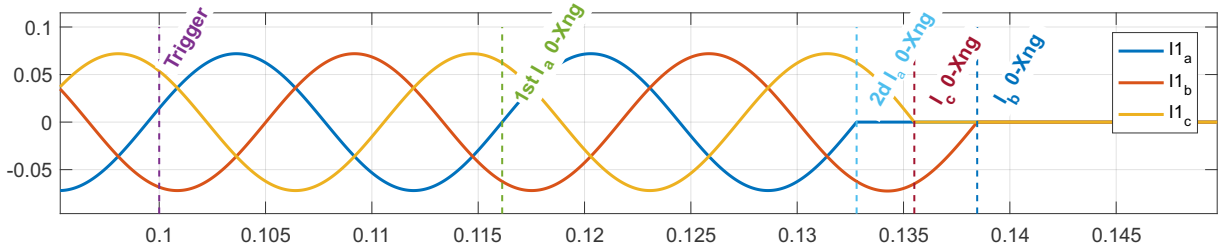

(b) $\boldsymbol{I}_{1abc}$ current solutions before, during, and after breaker 1 opening.

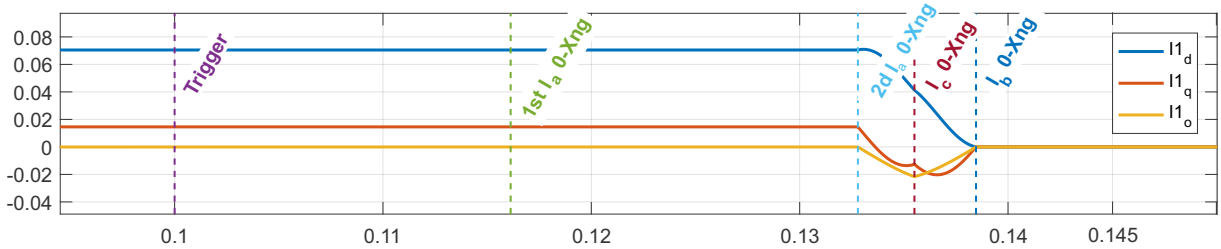

(c) $\boldsymbol{I}_{1dqo}$ current solutions before, during, and after breaker 1 opening.

Figure 2.5: Comparison of *abc* and *dqo* reference frame current solutions when a 3-phase breaker is opened. The significant point is that the steady-state sinusoidal currents in the *abc* reference frame are represented as constant values in the *dqo* reference frame.

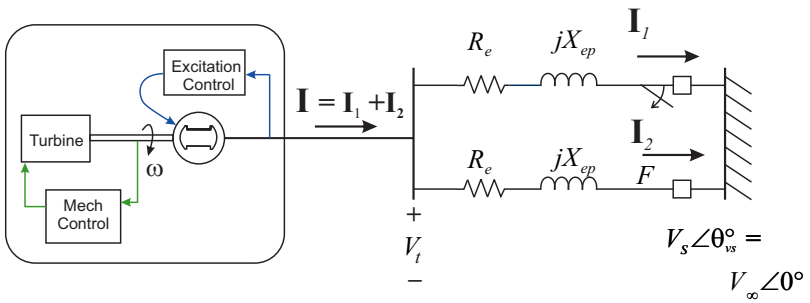

Figure 2.6: Synchronous machine connected to an infinite bus by identical parallel transmission lines.

The research presented in Chapter 5 will consider a power system composed of a synchronous generator connected via parallel transmission lines to an infinite bus; see the system one-line diagram in Fig. 2.6. This system's full-spectrum dynamic response can be fully characterized using the Multi-Time-Scale model (MTSM-14), which is comprised of 14 dynamic and 12 algebraic equations modeling the complete system. The three-damper-winding model (7 flux linkage state variables), already presented, accounts for the generator's electrical behavior.

3 Fast Dynamic States ψ_d, ψ_q, ψ_o

Stator Windings

(5.42.2) $$\varepsilon \frac{d\psi_d}{dt} = R_s\left(I_{d1} + I_{d2}\right) + \left(1 + \frac{\varepsilon}{T_s}\omega_t\right)\psi_q + V_d$$

(5.43.2) $$\varepsilon \frac{d\psi_q}{dt} = R_s\left(I_{q1} + I_{q2}\right) - \left(1 + \frac{\varepsilon}{T_s}\omega_t\right)\psi_d + V_q$$

(5.44.2) $$\varepsilon \frac{d\psi_o}{dt} = R_s\left(I_{o1} + I_{o2}\right) + V_o$$

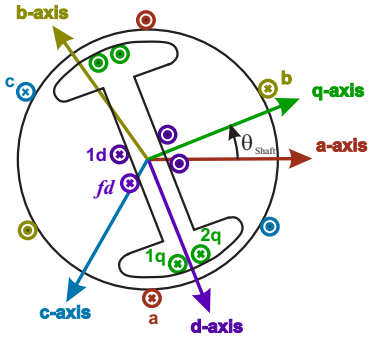

Scaled Variable	Description
θ	q-axis angular displacement from the a-axis– (rad)
θ_s	Rotating magnetic field axis angular displacement from a-axis (electrical rad/s)
δ	Rotor angle – ($\delta = \theta - \theta_s$) (electrical rad)
ω	Rotor angular velocity – (electrical rad/s)
ω_t	Transient speed – T_s ($\omega - \omega_s$) (electrical rad/s)
ψ_d, ψ_q, ψ_o	Stator winding flux linkage referred to *dqo*
V_d, V_q, V_o	Stator phase voltages referred to *dqo*
I_d, I_q, I_o	Stator winding currents referred to *dqo*

Parameter		Per unit value
R_s	Stator winding resistance; identical in each phase	0.003
ε	1 / ω_s appears as a scaling factor during the transformation and scaling of the system equations	$\frac{1}{377\ (\text{rad/s})}$

Figure 2.7: Synchronous machine – 3 fast dynamic equations – stator windings. These equations are scaled and transformed from the equations in Fig. 2.4. The equations are modified from the similarly numbered equations in Chapter 5 of [43].

Rounding out the MTSM-14 are the rotor shaft (2 state variables), excitation system (3 state variables), mechanical control system (2 state variables), and 12 algebraic equations modeling terminal conditions. The algebraic equations are determined by the transmission lines, infinite bus, and mathematical requirement to fully determine the system by matching the number of unknown variables and constraining equations.

The MTSM-14[3] is defined in Figs. 2.7 – 2.13 and reflects new variables arising from scaling and transformation modifications to the three-damper-winding model per Chapter 3, Synchronous Machine Modeling of [43]. For instance ψ_d, ψ_q, ψ_o, E'_d, E'_q, E_{fd}, and ω_t are the scaled and/or transformed variables originally denoted λ_d, λ_q, λ_o, ψ_{1q}, ψ_{fd}, and ω respectively. Note that resistances in the original equations do not explicitly appear in the transformed and scaled equations; rather, resistances are included in the dynamic equation time constant definitions. Variable fonts are colored consistent with axis color coding in corresponding diagrams to aid associating variables with d, q, and o axes; variables colored black are not associated with an axis; and ϵ and closely associated parameters are presented in yellow text, as they are key to distinguishing the MTSM-14 model and the reduced order (11 dynamic states) model to be presented.

The variables and equations that model the system behavior due to the stator windings are defined in Fig. 2.7. The stator winding flux linkages ψ_d, ψ_q, and ψ_o are the system's three fast dynamic states. Note ϵ, that entered the MTSM-14 as a frequency scaling factor.[4]

The remaining 11 not-so-fast state variables capture dynamic behaviors occurring in the rotor windings, rotor shaft, exciter sub-system, and mechanical power control sub-system. The four equations and constituent variables characterizing the rotor's field and three damper winding flux linkages are shown in Fig. 2.8.

[3]The machine models and equations are drawn from [43]; for ease of reference, equation numbers in these figures are traceable to corresponding equation numbers. The first two equation number positions here correspond directly to chapter and equation numbers; third equation number positions indicate modifications tailoring the equation to this application; and fourth equation number positions indicate its application to either TL-1, which opens during simulation, or TL-2, which remains closed throughout the simulation.

[4]i.e. $\epsilon = \omega_s^{-1} = \frac{1}{377}$

11 Not-So Fast Dynamic States $E'_q,\ \psi_{1d},\ E'_d,\ \psi_{2q},\ \delta,\ \omega_t,\ E_{fd},\ R_f,\ V_R,\ T_m,\ P_{SV}$

Part 1 of 4

Rotor Windings

(5.45.1) $$T'_{do}\frac{dE'_q}{dt} = -E'_q - (X_d - X'_d)\cdot\left[(I_{d1}+I_{d2}) - \frac{X'_d - X''_d}{(X'_d - X_{\ell s})^2}\left(\psi_{1d} + (X'_d - X_{\ell s})(I_{d1}+I_{d2}) - E'_q\right)\right] + E_{fd},$$

where $E'_q \triangleq \frac{X_{md}}{X_{fd}}\psi_{fd}$

(5.46.1) $$T''_{do}\frac{d\psi_{1d}}{dt} = -\psi_{1d} + E'_q - (X'_d - X_{\ell s})(I_{d1}+I_{d2})$$

(5.47.1) $$T'_{qo}\frac{dE'_d}{dt} = -E'_d + (X_q - X'_q)\cdot\left[(I_{q1}+I_{q2}) - \frac{X'_q - X''_q}{(X'_q - X_{\ell s})^2}\left(\psi_{2q} + (X'_q - X_{\ell s})(I_{q1}+I_{q2}) + E'_d\right)\right],$$

where $E'_d \triangleq -\frac{X_{mq}}{X_{1q}}\psi_{1q}$

(5.48.1) $$T''_{qo}\frac{d\psi_{2q}}{dt} = -\psi_{2q} - E'_d - (X'_q - X_{\ell s})(I_{q1}+I_{q2})$$

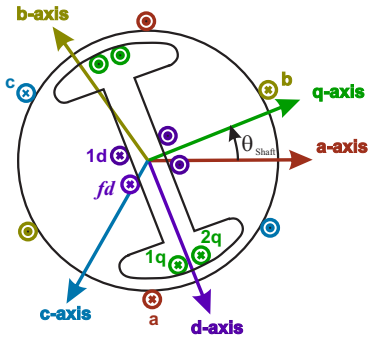

Scaled Variable	Description
ψ_{1d}, ψ_{2q}	d-axis and q-axis damper winding flux linkages
E_{fd}	Field voltage (scaled from V_{fd})
E'_d	q-axis transient voltage (scaled ψ_{1q})
E'_q	d-axis transient voltage (scaled ψ_{fd}); "Voltage behind the Transient Reactance"
I_d, I_q, I_o	Stator winding currents referred to dqo

Parameter		Per unit value
X_{ls}	Stator winding leakage reactance	0.15
X_{md}, X_{mq}	Stator winding magnetizing reactance, d- and q-axis	1.66, 1.61
X'_d, X'_q	Transient reactance d- and q-axis	0.3000, 0.5875
X''_d, X''_q	Sub-transient reactance d- and q-axis	0.2292, 0.2488
T'_{do}, T'_{qo}	Transient time constant d- and q-axis	8.171, 1.1943
T''_{do}, T''_{qo}	Sub-transient time constant d- and q-axis	0.0294, 0.0586

Figure 2.8: 11 not-so-fast dynamic equations (part 1 of 4) – rotor winding dynamics. The equations are modified from the similarly numbered equations in Chapter 5 of [43].

The current vector $\mathbf{I}_{dqo}$ is the sum of the current vectors $\mathbf{I}_{1dqo}$ and $\mathbf{I}_{2dqo}$ in branch transmission lines one (TL-1) and two (TL-2) respectively; branch TL-1 is opened during the simulation, causing the dynamic phenomenon of interest. With model reduction eliminating stator winding dynamics, these 11 dynamic variables will constitute the reduced order model to be considered in this investigation.

11 Not-So Fast Dynamic States $E'_q,\ \psi_{1d},\ E'_d,\ \psi_{2q},\ \boxed{\delta,\ \omega_t,}\ E_{fd},\ R_f,\ V_R,\ T_m,\ P_{SV}$

Part 2 of 4

Rotor Shaft Dynamics

(5.49) $$T_s \frac{d\delta}{dt} = \omega_t \text{ , where } \qquad \omega_t = T_s(\omega - \omega_s) \quad \text{and} \quad T_s = \sqrt{\frac{2H}{\omega_s}}$$

(5.50.1) $$T_s \frac{d\omega_t}{dt} = T_M - \left(\psi_d\left(I_{q1} + I_{q2}\right) - \psi_q\left(I_{d1} + I_{d2}\right)\right) - T_{FW}$$

$$\frac{d\theta_{shaft}}{dt} = \frac{\omega_t}{T_s} + \omega_s$$

Scaled Variable	Description	
θ	q-axis angular displacement from the a-axis– (rad)	
θ_s	Rotating magnetic field axis angular displacement from a-axis (electrical rad/s)	
θ_{vs}	Infinite bus reference angle, phase a	0.0°
δ	Rotor angle – ($\delta = \theta - \theta_s$) (rad)	
ω	Rotor angular velocity – (electrical rad/s)	
ω_s	Rated synchronous speed – $2\pi f$ – electrical angular velocity of the air-gap rotating magnetic field established by the stator current's fundamental frequency	377 (rad/s)
ω_t	Transient speed – $T_s(\omega - \omega_s)$ (electrical rad/s)	
ψ_d, ψ_q, ψ_o	Scaled stator winding flux linkages referred to *dqo*	
I_d, I_q, I_o	Stator winding currents referred to *dqo*	
T_M	Torque—prime mover	

Parameter		Per unit value
T_s	Shaft mechanical time constant	0.1362 s
H	Shaft inertia constant	3.5 s
T_{FW}	Torque—friction and windage opposing prime mover	0.0

Figure 2.9: 11 not-so-fast dynamic equations (part 2 of 4) – rotor shaft dynamics. The equations are modified from the similarly numbered equations in Chapter 5 of [43].

The pair of equations describing rotor shaft dynamics are shown in Fig. 2.9. Note that angular velocity state variable ω initially introduced has been transformed to ω_t, which is the scaled difference between the magnetic field axis and rotor angular velocities.

An equation casting θ_{shaft} as an integrable state variable in the transformed and scaled model has been added; during simulation, it proved useful for referring resistance and reactance matrices between the *abc* and *dqo* reference frames under unbalanced line conditions.

11 Not-So Fast Dynamic States $E'_q,\ \psi_{1d},\ E'_d,\ \psi_{2q},\ \delta,\ \omega_t,\ E_{fd},\ R_f,\ V_R,\ T_m,\ P_{SV}$

Excitation System **Part 3 of 4**

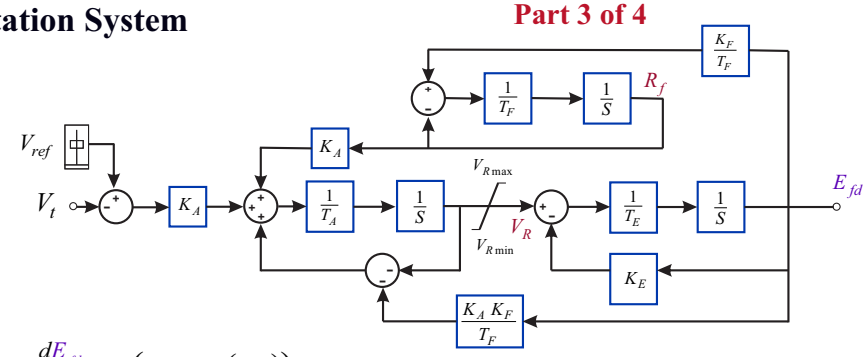

(5.54) $$T_E \frac{dE_{fd}}{dt} = -\left(K_E + S_E\left(E_{fd}\right)\right)E_{fd} + V_R$$ **Main Exciter**

(5.55) $$T_F \frac{dR_f}{dt} = -R_f + \frac{K_F}{T_F} E_{fd}$$ **Stabilizing Transformer**

(5.56) $$T_A \frac{dV_R}{dt} = -V_R + K_A R_f - \frac{K_A K_F}{T_F} E_{fd} + K_A\left(V_{ref} - V_t\right)$$ **Pilot Exciter**

(5.57) $$V_R^{\min} \le V_R \le V_R^{\max}$$ $-5.0 \le V_R \le 5.0$

Scaled Variable	Description
R_f	Rate feedback
V_R	Exciter input voltage
E_{fd}	Field voltage (scaled from V_{fd})

Parameter		Per unit value
K_A	Pilot exciter gain	200
K_E	Main exciter gain	1.00
K_F	Rate feedback amplifier gain	0.03
T_A	Pilot exciter time constant	0.04
T_E	Main exciter time constant	0.70
T_F	Rate feedback amplifier time constant	1.00
V_{ref}	Pilot exciter reference voltage	1.012

Figure 2.10: 11 not-so-fast dynamic equations (part 3 of 4) – excitation system. The equations are modified from the similarly numbered equations in Chapter 5 of [43].

11 Not-So Fast Dynamic States E'_q, ψ_{1d}, E'_d, ψ_{2q}, δ, ω_t, E_{fd}, R_f, V_R, T_m, P_{SV}

Mechanical Power Control System

Part 4 of 4

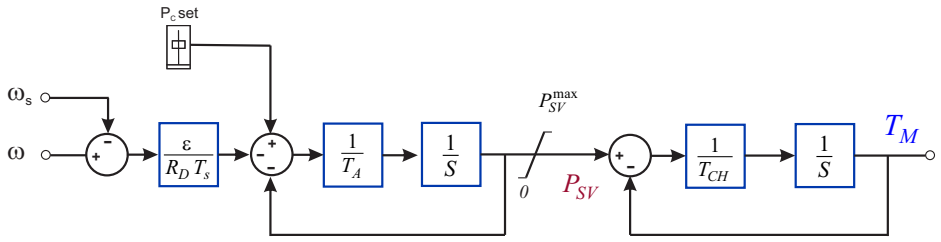

(5.63) $$T_{CH}\frac{dT_M}{dt} = -T_M + P_{SV}$$ **Single Stage Turbine Model**

(5.64) $$T_{SV}\frac{dP_{SV}}{dt} = -P_{SV} + P_C - \frac{\varepsilon}{R_D T_s}\omega_t$$ **Governor Model**

(5.65) $$0 \le P_{SV} \le P_{SV}^{max}$$

Scaled Variable	Description
P_{SV}	Steam valve position – proportional to steam pressure
T_M	Torque—prime mover
ω_t	Transient speed – T_s (ω - ω_s) – electrical rad/s

Parameter		Per unit value
T_{CH}	Steam chest time constant	0.05
T_s	Shaft mechanical time constant	0.1363
T_{FW}	Torque—friction and windage opposing prime mover; neglected in this formulation	0.0
T_{SV}	Steam valve time constant	0.10
R_D	Speed regulation quantity – also known as “droop” factor	0.05
P_C	Power change setting	0.255
ε	1 / ω_s appears as a scaling factor during the transformation and scaling of the system equations	$\frac{1}{377\ (\text{rad/s})}$

Figure 2.11: 11 not-so-fast dynamic equations (part 4 of 4) – mechanical power control. The equations are modified from the similarly numbered equations in Chapter 5 of [43].

The three state variable equations defining the excitation sub-system are shown in Fig. 2.10; the exciter’s feedback control scheme is also shown. The two state variable equations modeling turbine and shaft speed governor dynamic behavior in the mechanical power control sub-system are shown in Fig. 2.11. The sub-system’s feedback control scheme depicting the turbine and governor interaction is also shown.

15 Algebraic Equations $I_{d1}, I_{q1}, I_{o1}, I_{d2}, I_{q2}, I_{o2},$ $V_d, V_q, V_o, \frac{dI_{d1}}{dt}, \frac{dI_{q1}}{dt}, \frac{dI_{o1}}{dt},$ $\frac{dI_{d2}}{dt}, \frac{dI_{q2}}{dt}, \frac{dI_{o2}}{dt}$

Part 1 of 2

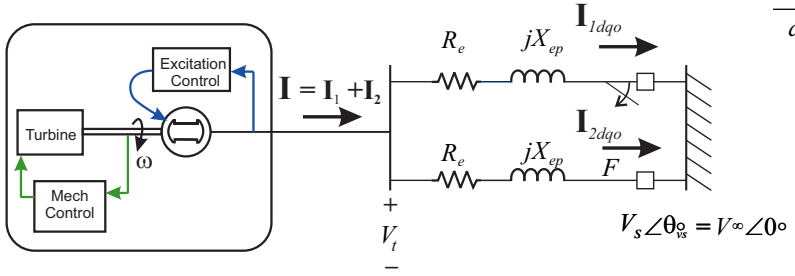

(5.51.5.1) $$I_{d1} = \frac{1}{\left(X''_d + X_{11,1}\right)}\left[-\psi_d + \frac{\left(X''_d - X_{\ell s}\right)}{\left(X'_d - X_{\ell s}\right)}E'_q + \frac{\left(X'_d - X''_d\right)}{\left(X'_d - X_{\ell s}\right)}\psi_{1d} - \left[X_{12,1}I_{q1} + X_{13,1}I_{o1}\right]\right]$$

(5.52.5.1) $$I_{q1} = \frac{1}{\left(X''_q + X_{22,1}\right)}\left[-\psi_q - \frac{\left(X''_q - X_{\ell s}\right)}{\left(X'_q - X_{\ell s}\right)}E'_d + \frac{\left(X'_q - X''_q\right)}{\left(X'_q - X_{\ell s}\right)}\psi_{2q} - \left[X_{21,1}I_{d1} + X_{23,1}I_{o1}\right]\right]$$

(5.53.5.1) $$I_{o1} = \frac{1}{\left(X_o + X_{33,1}\right)}\left[-\psi_o - \left[X_{31,1}I_{d1} + X_{32,1}I_{q1}\right]\right]$$

(5.51.5.2) $$I_{d2} = \frac{1}{\left(X''_d + X_{11,2}\right)}\left[-\psi_d + \frac{\left(X''_d - X_{\ell s}\right)}{\left(X'_d - X_{\ell s}\right)}E'_q + \frac{\left(X'_d - X''_d\right)}{\left(X'_d - X_{\ell s}\right)}\psi_{1d} - \left[X_{12,2}I_{q2} + X_{13,2}I_{o2}\right]\right]$$

(5.52.5.2) $$I_{q2} = \frac{1}{\left(X''_q + X_{22,2}\right)}\left[-\psi_q - \frac{\left(X''_q - X_{\ell s}\right)}{\left(X'_q - X_{\ell s}\right)}E'_d + \frac{\left(X'_q - X''_q\right)}{\left(X'_q - X_{\ell s}\right)}\psi_{2q} - \left[X_{21,2}I_{d2} + X_{23,2}I_{o2}\right]\right]$$

(5.53.5.2) $$I_{o2} = \frac{1}{\left(X_o + X_{33,2}\right)}\left[-\psi_o - \left[X_{31,2}I_{d2} + X_{32,2}I_{q2}\right]\right]$$

Figure 2.12: Infinite bus system – algebraic equations (part 1 of 2). These equations describe the TL-1 and TL-2 currents ($\mathbf{I}_{1dqo}$ and $\mathbf{I}_{2dqo}$ respectively). and are modified from the similarly numbered equations in Chapter 5 of [43] to reflect modified terminal conditions. In the initial equilibrium, the TL-1 and TL-2 current equations are identical, including reactance matrices $\mathbf{X}_{[\mathbf{3x3}],\mathbf{1}}$ and $\mathbf{X}_{[\mathbf{3x3}],\mathbf{2}}$ which reflect transmission line reactances referred to the *dqo* reference frame. During the TL-1 breaker opening sequence, the TL-1 reactance matrix is both a function of rotor position and an unbalanced matrix. Once TL-1 is open, $\mathbf{X}_{[\mathbf{3x3}],\mathbf{1}}$ models an open circuit. The reactance matrix row entries are color coded to enhance clarity.

Figures 2.12 and 2.13 detail the system's algebraic equations. While the state variable equations are determined by the synchronous machine, exciter, and mechanical control subsystem models, the algebraic equations are determined by the terminal conditions – i.e. all other system components. Figure 2.12 details three current equations: the terminal current $\mathbf{I}_{dqo}$ and transmission line currents $\mathbf{I}_{1dqo}$ and $\mathbf{I}_{2dqo}$. Transmission lines TL-1 and TL-2 and

their respective reactance matrices, $\mathbf{X}_{[3x3],1}$ and $\mathbf{X}_{[3x3],2}$, are initially identical, but $\mathbf{X}_{[3x3],1}$ changes as breaker 1 opens. During the breaker opening sequence, the a, b, and c phase

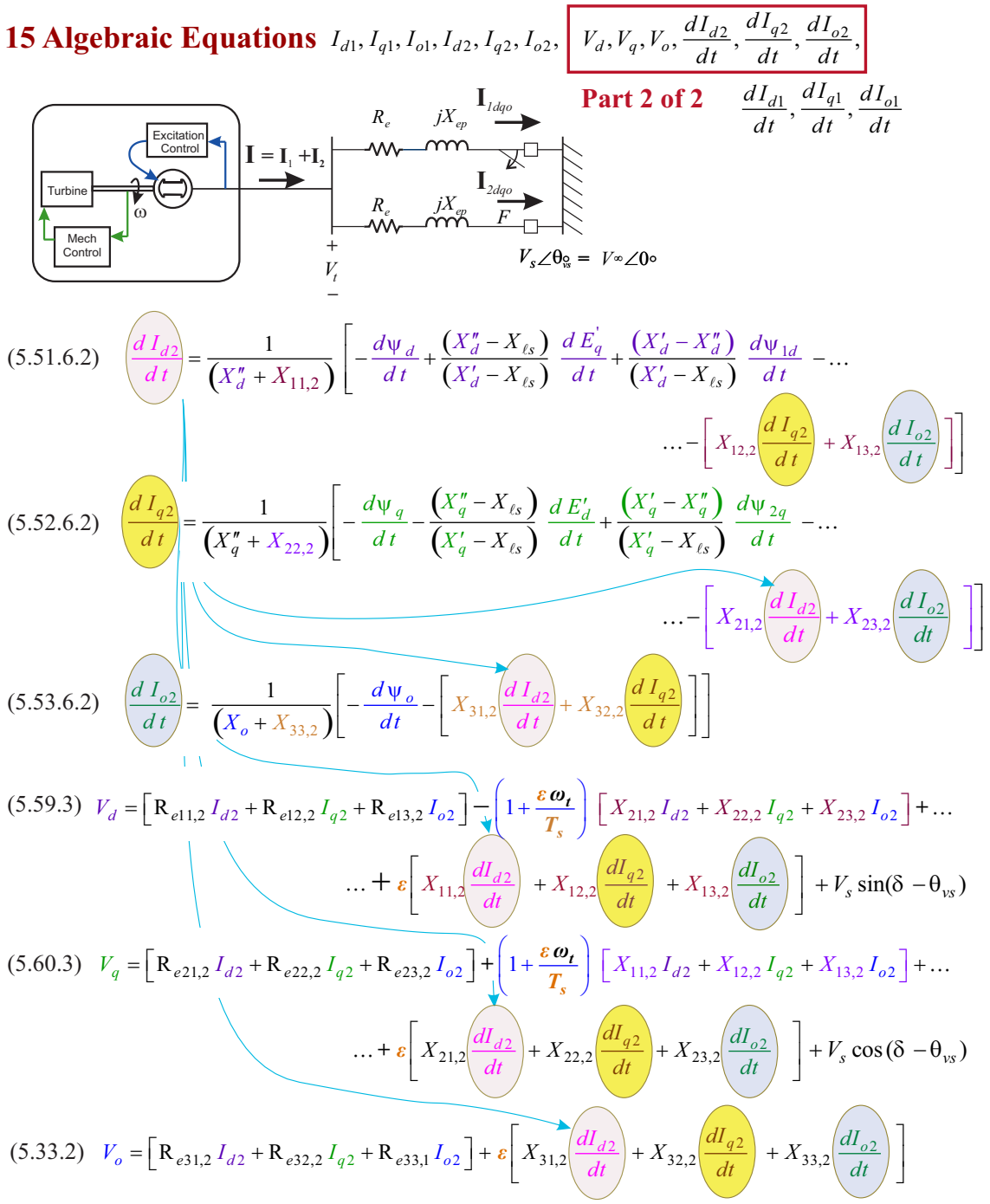

Figure 2.13: Infinite bus system – algebraic equations (part 2 of 2). The equations are modified from the similarly numbered equations in Chapter 5 of [43]. Note that the voltage equations each include ϵ, which is important in the reduced order model development.

lines open as the respective currents pass through 0. As breaker 1 opens, the TL-1 reactance matrix is both a function of rotor position and is an unbalanced matrix. Once the TL-1 breaker is open, $\mathbf{X}_{[\mathbf{3x3}],\mathbf{1}}$ models an open circuit. This terminal condition formulation makes clear the distinction between the synchronous machine (internal) and transmission line (external) reactance effect upon $\mathbf{I}_{dqo}$ currents. Note that X_d'', X_d'', and X_o appear $\mathbf{X}_{[\mathbf{3x3}],\mathbf{1}}$ and $\mathbf{X}_{[\mathbf{3x3}],\mathbf{2}}$, so these matrices are not strictly functions of external transmission line parameters.

Figure 2.13 details the algebraic equations that determine generator terminal voltage, $\mathbf{V}_{dqo}$, which is computed as a function of the $\mathbf{I}_{2dqo}$ time rate of change – chosen because TL-2 remains in the circuit throughout the simulation. While depicted as time derivatives in equations (5.51.6.2), (5.52.6.2), (5.53.6.2), these equations are not new state equations; rather, $\frac{d\,I_{d2}}{dt}$, $\frac{d\,I_{q2}}{dt}$, and $\frac{d\,I_{o2}}{dt}$ are computed algebraically from the system's state variables and solving the $[3\,x\,3]$ sub-matrix formed by these equations. The algebraic solutions for $\frac{d\,I_{d2}}{dt}$, $\frac{d\,I_{q2}}{dt}$, and $\frac{d\,I_{o2}}{dt}$ are, in turn, used to compute $\mathbf{V}_{dqo}$. The figure uses color coding to aid in visualizing the inter-relationships between the variables in the six equations. Note that a similar set of equations can also be written to compute solutions for $\frac{d\,I_{d1}}{dt}$, $\frac{d\,I_{q1}}{dt}$, and $\frac{d\,I_{o1}}{dt}$, though these values are not needed.

2.2.2 Reduced Order Model (11th Order)

When modeling power systems, common industry practice is to use synchronous machine models that neglect stator winding flux linkage transients, and consequently, stator winding voltage transients. This enables balancing the computational burden and the solution information needed for the application, which more often than not does not include the comparatively fast stator transients. A widely applied theoretical basis for this model reduction is derived by applying the integral manifold approach, which includes changing flux linkage effects without including their differential equations.

A manifold is a functional relationship between variables. The fundamental concept

is captured in the following example that outlines the mathematical steps of expressing a two-time-scale dynamic system as a one-time-scale system.[5] The key is finding a functional relationship between the fast dynamics in z and the comparatively slower dynamics in x, which are characterized by the equations and initial conditions:

$$\begin{aligned} \frac{dx}{dt} &= f(x,\ z) \qquad x(0) = x^o \\ \varepsilon\frac{dz}{dt} &= g(x,\ z) \qquad z(0) = z^o \end{aligned} \tag{2.11}$$

The manifold (functional relationship) is expressed as

$$z = h\,(\mathrm{x},\, \epsilon) \tag{2.12}$$

in which ϵ is sufficiently small so that the manifold expressed as a Taylor series is:

$$h\,(x,\ \varepsilon) = h_o\,(x) + \varepsilon h_1\,(x) + \epsilon^2 h_2\,(x) + \ldots \tag{2.13}$$

Substituting Eq. (2.13) into Eq. (2.12) and the result into Eq. (2.11) yields

$$\varepsilon\left(\frac{\partial\, h_o}{\partial x} + \varepsilon\frac{\partial\, h_o}{\partial x} + \ \ldots\right)\ f\,(x,\ h) = g\ \ (x,\ h)$$

Using the Taylor series to expand f and g about $\epsilon = 0$

$$\begin{aligned} f\,(x,\ h) &= \quad f\ (x,\ h_o) + \varepsilon\frac{\partial\, f}{\partial\, z}|_{z=h_o}\, h_1 + \ldots \\ g\,(x,\ h) &= \quad g\ (x,\ h_o) + \varepsilon\frac{\partial g}{\partial z}|_{z=h_o}\, h_1 + \ldots \end{aligned}$$

[5]Drawn from multiple sources. In [53], the example is stand-alone. In Appendix A of [43], the example is presented as part of a comprehensive development of integral manifolds for application to synchronous machine model reduction.

yields the partial differential equation

$$\varepsilon\left(\frac{\partial\, h_o}{\partial\, x}\ +\ \varepsilon\frac{\partial\, h_1}{\partial\, x}+\ldots\right)\ \left(f\ (x,\ h_o)\ +\ \varepsilon\frac{\partial\, f}{\partial\, z}\,|_{z=h_o}h_1\ +\ldots\right)$$
$$=\ g\,(x,\ h_o)\ +\ \varepsilon\frac{\partial g}{\partial z}\,|_{z=h_o}\,h_1+\ldots$$

which after collecting terms and equating "power of ϵ" coefficients yields a system of algebraic equations that can be solved for h_o, h_1, h_2, etc., to obtain the desired accuracy (i.e. by choosing the appropriate power of ϵ):

$$\begin{aligned}\epsilon^o:&\qquad 0\ =\ g\,(x,\ h_o)\\ \epsilon^1:&\qquad \frac{\partial\, h_o}{\partial\, x}\ f\,(x,\ h_o)\ =\ \varepsilon\frac{\partial g}{\partial z}|_{z=h_o}\,h_1\end{aligned}$$

The concept lends itself nicely to visualization in a three-variable system modeled by two slow dynamic variables x_1 and x_2 and the fast dynamic variable z. The surface in Fig. 2.14 represents the chosen manifold relating the fast and slow dynamic variables. Ideally, the initial condition lies on the integral manifold and exactly satisfies the manifold function

$$z\ =\ h\,(x^o,\ \epsilon)$$

In this case, the solution follows a trajectory on the manifold from the initial to the final equilibrium condition. A second case occurs when the initial conditions yield an off-manifold starting solution; the solution evolves along a trajectory from that solution to an on-manifold equilibrium solution. A third possibility, not depicted, is that off-manifold initial conditions produce a starting solution "too distant" from the manifold to converge an equilibrium solution on the manifold surface, which is, needless to say, not useful as a reduced-order system representation.

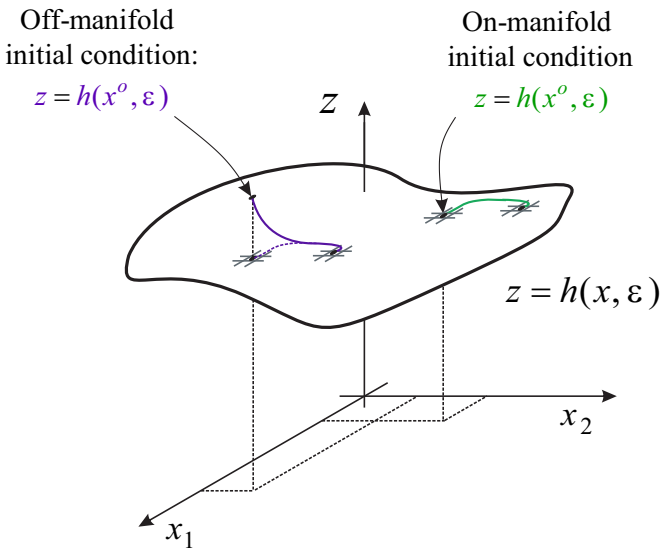

Figure 2.14: Visualizing the integral manifold as a function of two slow dynamic variables x_1 and x_2 and one fast dynamic variable z; adapted from Fig A.3, Appendix A of [43]. The surface represents the integral manifold as the exact functional relationship between z and x. Ideally, the initial conditions are on the manifold and the solution trajectory follows the manifold to the steady state solution. When the initial conditions are off-manifold and "close-enough," the solution trajectory will move to the manifold and to a steady state condition. When not "close-enough," the reduced order equations will not yield a meaningful solution.

The detailed development of the 11th-order reduced system model (RedSysMdl-11) is involved and beyond the scope of this presentation. Sauer details the integral manifold approach to the RedSysMdl-11 in [43]. Full mathematical development of the integral manifold approach to synchronous machine model order reduction is presented in the original papers [46, 47].

In essence, the RedSysMdl-11 can be obtained from the MTSM-14 by arguing that since $\epsilon \approx 0$, setting $\epsilon = 0$ is equivalent to the reduced order model produced using the integral manifold approach. Again, ϵ and associated terms are presented in yellow text. Setting $\epsilon = 0$ in Eqs (5.42), (5.43), and (5.44) in Fig 2.7 reduces the stator flux linkage state equations to algebraic equations. The terms ϵ and ϵ/T_s appear in the stator voltage equations (Fig. 2.13) and are set to zero. This yields simplified terminal voltage algebraic equations.

The necessary and notable exception to setting $\epsilon = 0$ and eliminating the term is in the $\epsilon/R_D T_s$ term appearing in governor model equation (Fig. 2.11); otherwise, the feedback

loop linking rotor speed and mechanical power control is lost. The droop regulation factor, R_D (.05 in this application), is sufficiently small so that, while $\epsilon \approx 0$, the term $\epsilon/R_D T_s$ does not approach zero and is therefore justifiably retained.

2.2.3 Synchronous Machine System Simulation

A MATLAB simulation was written for the synchronous machine-infinite bus system simulating solutions to compare the MTSM-14 and RedSysMdl-11 models. In the simulation, TL-1 is opened, changing the impedance between the generator and infinite bus and causing a transient response as the system moves to a new equilibrium point. Transmission line TL-2 remains closed through the simulation. The simulation system parameters are listed in Figs 2.7 through 2.13.

Transmission line parameters were determined as follows to facilitate normalized transmission line characteristics between the simulations, driven principally by the RTDS transmission line modules constraints. Transmission lines TL-1 and TL-2 are identical. The starting point was a 10 km "typical" 230KV overhead transmission line as listed Table 6.1 of [52] operating at surge impedance load (140 MW) and 60 Hz. The RTDS Overhead Line Constants Program[6] data input screens and computed transmission line impedance matrices are shown in Fig. 2.15.

Note that the RTDS Overhead Line Constants Program impedance matrices include off-diagonal resistance values, indicating resistive cross-coupling between transmission line phases. The theoretical basis for these cross-coupling terms is not included in the program documentation, which highlights the "black box" module nature in some RTDS implementation details. This highlights the challenges of normalizing RTDS and our MATLAB simulation without full knowledge of RTDS module inner workings. The MATLAB simulation includes the RTDS computed on-diagonal resistance matrix entries, but neglects the off-diagonal entries.

[6]RTDS Technologies Inc. transmission line module is also referred to as TLine Version 2.0 (2014) 4.006.2.

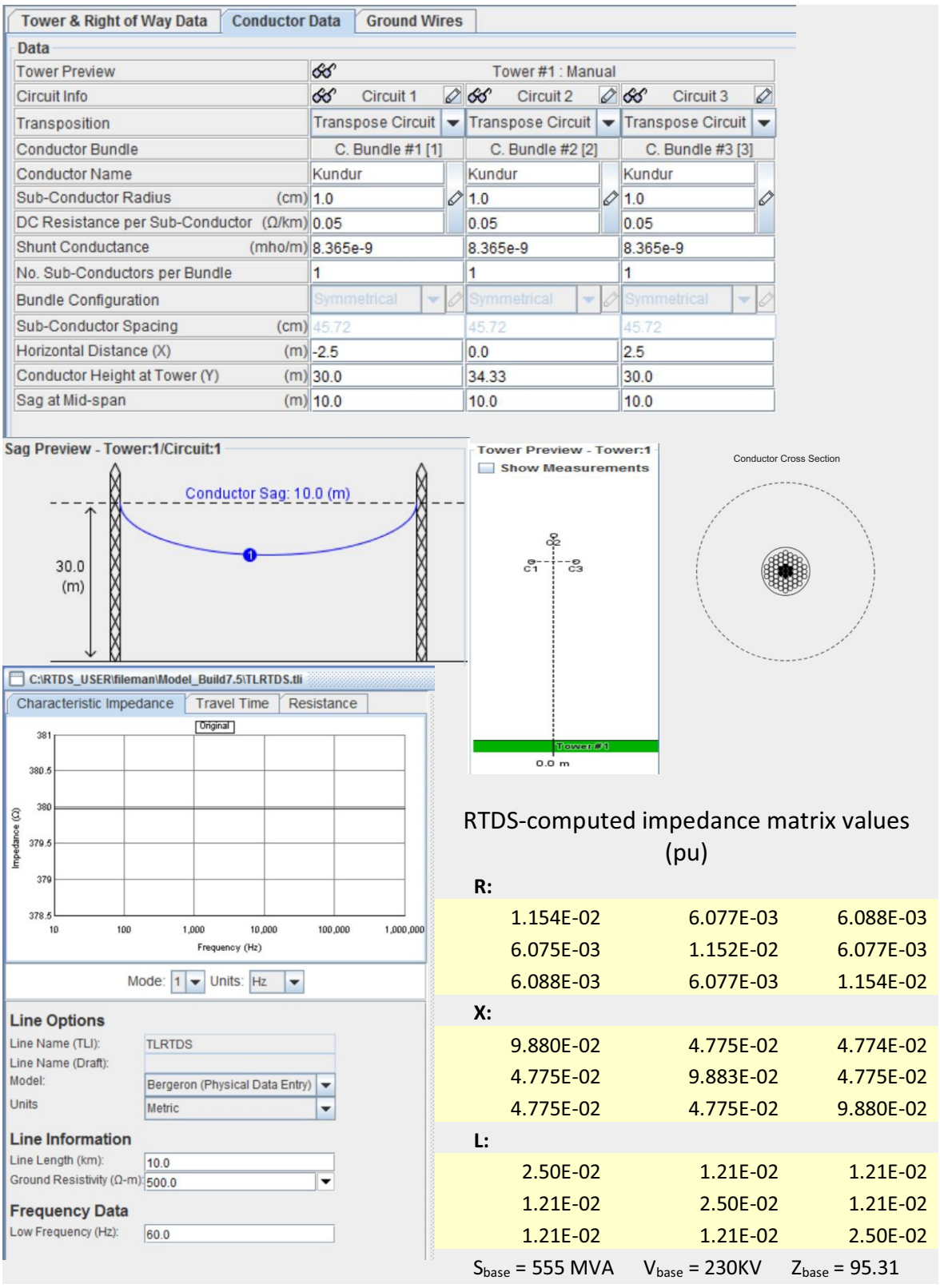

RTDS-computed impedance matrix values (pu)

R:			
	1.154E-02	6.077E-03	6.088E-03
	6.075E-03	1.152E-02	6.077E-03
	6.088E-03	6.077E-03	1.154E-02
X:			
	9.880E-02	4.775E-02	4.774E-02
	4.775E-02	9.883E-02	4.775E-02
	4.775E-02	4.775E-02	9.880E-02
L:			
	2.50E-02	1.21E-02	1.21E-02
	1.21E-02	2.50E-02	1.21E-02
	1.21E-02	1.21E-02	2.50E-02

S_{base} = 555 MVA V_{base} = 230KV Z_{base} = 95.31

Figure 2.15: RTDS Overhead Line Constants Program data input screens – computed impedance matrix entries are highlighted in yellow.

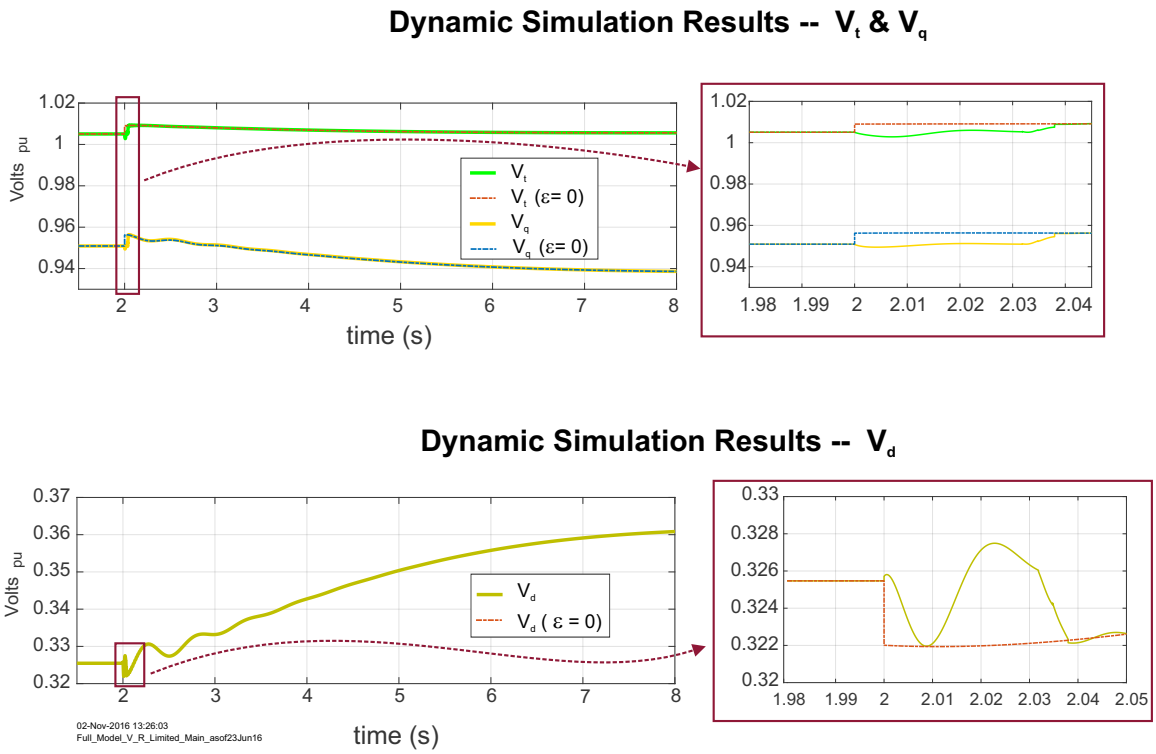

Figure 2.16: Terminal voltage (*dqo* reference frame) dynamic response when 1 of 2 lines is opened at $t = 2$ s.

The generator's terminal voltage and current dynamic responses are shown in Figs. 2.16 and 2.17 respectively. Each figure shows superimposed simulation results for the MTSM-14 and RedSysMdl-11 models for comparison. The generator terminal dynamic model response characteristics (voltages and currents with $\epsilon \neq 0$) include the fast transient stator flux linkages modeled in Eqs. (5.42), (5.43), and (5.44) in Fig. 2.7. For comparison, the RedSysMdl-11 generator terminal model response characteristics (voltages and currents with $\epsilon = 0$) are superimposed. The full and reduced model simulations show very similar results, but are nonetheless distinguishable – particularly in the transient response period. This is shown very clearly in the I_{dq} transient response curves (Fig 2.17); the RedSysMdl-11 I_{dq} curves follow a path through the center of mass of the envelop bounding the MTSM-14 I_{dq} curves. Of note is that MTSM-14 I_{dq} curve envelopes are defined by a nominally 60 Hz oscillation. This observation tracks nicely with the expected integral manifold approach variable reduc-

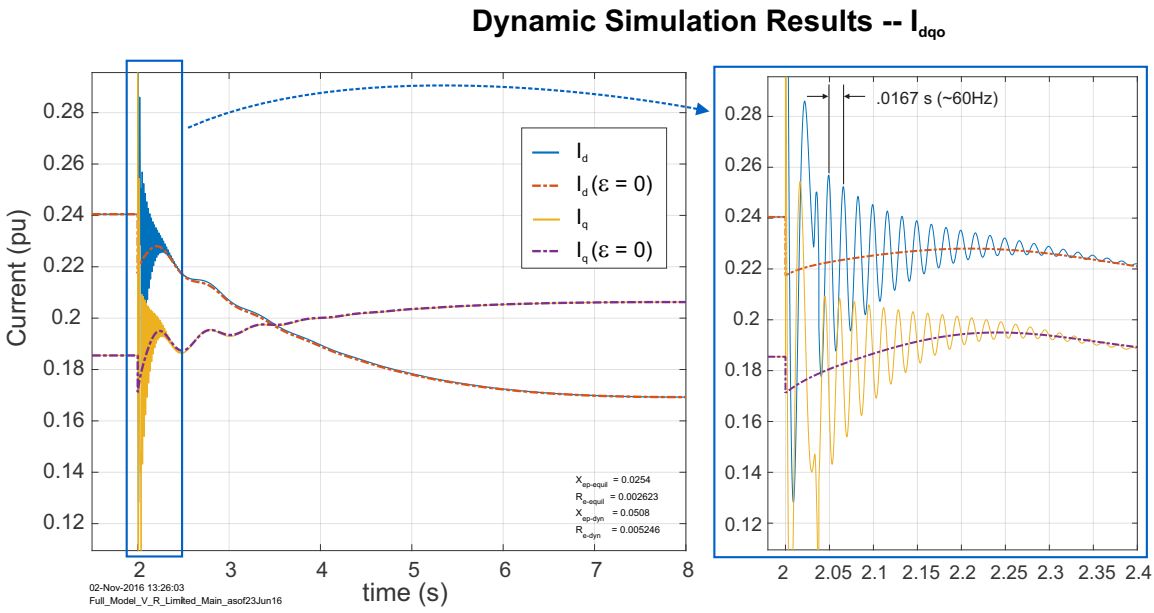

Figure 2.17: Terminal current (*dqo* reference frame) dynamic response when 1 of 2 lines is opened at $t = 2$ s.

tion outcome eliminating the stator flux linkage state variables, which would have a 60 Hz component. Recalling Fig. 2.5, care must be taken not misinterpret (or confuse) the seeming 60 Hz oscillation in the *dqo* frame with the *abc* frame's nominal 60 Hz system frequency. The oscillation observed in the *dqo* frame exists as a short-lived transient. Recall that any waveform moving synchronously with the rotor has a constant value in the *dqo* reference frame, and as expected I_{dq} settles to constant values several seconds after TL-1 opens.

In Chapter 5, the simulation's voltage and current response will be "sampled" in simulation to mimic phasor measurement unit processing to investigate dynamic system response information that can be gleaned from synchrophasor data. In parallel and for comparison, the system was also simulated on the Real-Time Digital Simulator (RTDS) operated by the Information Trust Institute, University of Illinois at Urbana-Champaign. The RTDS digitally simulates the dynamic system response and in real time produces analog voltage and current signals that can be sampled by a commercial PMU.

Chapter 3

Distribution Factors for Linear Contingency Analysis

As introduced in Chapter 2, the power system is very complex. The system's operating state is periodically estimated (several times per hour) from system-wide measurements. However, not easily known are changes to the system's operating state should an unexpected system event occur – say, the loss of a transmission line. In a very large power system, there are thousands of possible contingency cases arising from unforeseen system changes. The system operator needs to quickly assess contingency impacts: Is the effect minor requiring no action? Or is there a major impact that dictates emergency action? Solving the full power flow problem for each contingency (possibly numbering in the thousands) is impractical, if not impossible. Distribution factors provide fast, "computationally light" methods for estimating contingency case impacts, enabling rapid screening for the dangerous contingencies. This chapter extends distribution factor-based contingency analysis to several key applications.

The distribution factors developed here estimate changes due to a sudden line opening (or re-closure); the distribution factors are easily extended to estimating generator internal current surges when a line opens (or closes).[1] When a line under load is opened, currents throughout the network change much faster than any generator of load dynamics to satisfy energy conservation laws manifested in Kirchhoff's current and voltage laws. Excessive current changes, consequent to sudden and extreme power mismatches, produce extreme torques that can severely damage generator shafts. If the system is stable, the dynamics should settle to new conditions that are only slightly different from the pre-outage case. Power-flow methods (linear or nonlinear) compute the final system state based upon power

[1]This line of investigation was first reported by Sauer, Reinhard, and Overbye in [54].

system topology. Estimates of instantaneous internal generator redistribution currents can be determined by modifying the simulated circuit topology to include synchronous machine transient reactances, enabling rapid screening operating states in which line opening (or reclosure) risks damaging equipment.

3.1 Transfer Distribution Factors

The basis for this analysis begins by considering linear circuits with voltage and current sources interconnected by impedances. Consider an n-bus plus ground network modeled with the admittance matrix referenced to ground. For an operating condition called case A, Kirchhoff's current law at each bus is:

$$\begin{bmatrix} I_1^A \\ \vdots \\ I_n^A \end{bmatrix} = \begin{bmatrix} Y_{11} & \dots & Y_{1n} \\ \vdots & \dots & \vdots \\ Y_{n1} & \dots & Y_{nn} \end{bmatrix} \begin{bmatrix} V_1^A \\ \vdots \\ V_n^A \end{bmatrix} \tag{3.1}$$

with each bus injection current I_1^A coming from the ground through a path not included in Y. The Y matrix may include any line, transformer, or load admittance connected between any two buses or between a bus and ground. For a generator, this injection current is the generator current. For a load (not included in Y), this injection current is the negative of the load current. All quantities are in per unit. For this analysis, let bus 1 be the system's swing bus such that $V_1 = V_1^0$, i.e. an ideal fixed-voltage source (fixed magnitude and 0^o reference angle). Eliminating the bus 1 current from the network model gives

$$\begin{bmatrix} I_2^A \\ \vdots \\ I_n^A \end{bmatrix} = \begin{bmatrix} Y_{22} & \dots & Y_{2n} \\ \vdots & \dots & \vdots \\ Y_{n2} & \dots & Y_{nn} \end{bmatrix} \begin{bmatrix} V_2^A \\ \vdots \\ V_n^A \end{bmatrix} + \begin{bmatrix} Y_{21} \\ \vdots \\ Y_{n1} \end{bmatrix} \begin{bmatrix} V_1^0 \end{bmatrix} \tag{3.2}$$

Solving for the case A voltages gives

$$\begin{bmatrix} V_2{}^A \\ \vdots \\ V_n{}^A \end{bmatrix} = \begin{bmatrix} Z_{22} & \dots & Z_{2n} \\ \vdots & \dots & \vdots \\ Z_{n2} & \dots & Z_{nn} \end{bmatrix} \begin{bmatrix} I_2^A - Y_{21}V_1^0 \\ \vdots \\ I_n^A - Y_{n1}V_1^0 \end{bmatrix} \tag{3.3}$$

The line currents for case A are:

$$I_{ij}^{\ A} = \frac{V_i{}^A - V_j{}^A}{\bar{z}_{ij}} \tag{3.4}$$

where $\bar{z}_{ij}$ is the primitive line ij impedance. Now consider injection current changes from case A to case B. The case B network equations (for unchanged impedances) are:

$$\begin{bmatrix} V_2{}^B \\ \vdots \\ V_n{}^B \end{bmatrix} = \begin{bmatrix} Z_{22} & \dots & Z_{2n} \\ \vdots & \dots & \vdots \\ Z_{n2} & \dots & Z_{nn} \end{bmatrix} \begin{bmatrix} I_2^B - Y_{21}V_1^0 \\ \vdots \\ I_n^B - Y_{n1}V_1^0 \end{bmatrix} \tag{3.5}$$

The line currents for case B are:

$$I_{ij}^{\ B} = \frac{V_i{}^B - V_j{}^B}{\bar{z}_{ij}} \tag{3.6}$$

From Eqs. (3.3) thru (3.6), the changes in node voltages and line currents ij between cases A and B are:

$$\begin{bmatrix} \Delta V_2 \\ \vdots \\ \Delta V_n \end{bmatrix} = \begin{bmatrix} Z_{22} & \dots & Z_{2n} \\ \vdots & \dots & \vdots \\ Z_{n2} & \dots & Z_{nn} \end{bmatrix} \begin{bmatrix} \Delta I_2 \\ \vdots \\ \Delta I_n \end{bmatrix} \tag{3.7}$$

with

$$\Delta I_{ij} = I_{ij}^B - I_{ij}^{\ A} = \sum_{k=2}^{n} \left[\frac{Z_{ik} - Z_{jk}}{\bar{z}_{ij}} \right] \Delta I_k \tag{3.8}$$

and

$$\Delta I_k = I_k^B - I_k^A \tag{3.9}$$

When bus i or j is 1, the Z entries are defined to be zero. The line current change on line ij can also be written as

$$\Delta I_{ij} = \sum_{k=2}^{n} T_{ij,k} \Delta I_k \tag{3.10}$$

where

$$T_{ij,\,k} = \left[\frac{Z_{ik} - Z_{jk}}{\bar{z}_{ij}} \right] \tag{3.11}$$

is a "current" transfer distribution factor (CTDF). In power flow studies, it is commonly accepted practice to use Stott's "fast decoupled load flow" technique to reduce computational burden by trading off a measure of solution accuracy; the technique's underlying assumptions include neglecting resistance ($R_{ij} \approx 0$), neglecting shunt reactances (i.e. charging admittances) to ground, and assuming bus voltages to be near unity ($V_i \approx 1$ pu) [55]. The fast decoupled load flow bus voltage assumption provides a sound rationale for extending the CTDF to "power" transfer distribution factors (PTDFs) by multiplying both sides of Eq. (3.10) by the assumed 1 pu bus voltage. Note that under these assumptions, the PTDFs are defined solely in terms of transmission line reactances. Further, real power line flows change in response to real power system injections (positive injections represent power generation; negative injections represent loads). Thus, transmission line power flows can be approximated:

$$\Delta P_{ij} \approx \sum_{k=2}^{n} PTDF_{ij,\,k}\, \Delta P_k \tag{3.12}$$

For the derivations presented in the following sections, the change from case A to case B will always be done with constant impedances and constant topology. Thus, the change due to a line outage (topology change) is not the change from case A to case B. Fictitious changes in injections (i.e. from case A to case B) will be used to compute the impact of a line outage on flows and voltages. These injection changes are applied to networks either

with the line "IN" or the line "OUT". As such, the factors will be labeled to reflect this change.

3.2 Line Outage Distribution Factor (LODF)

The current transfer distribution factors above can be used to approximate the effects of a line outage as follows. Consider a change in the injection current at bus i equal to:

$$\Delta I_i = -\frac{I_{ij}^{IN}}{T_{ij,\,k}^{IN}} \tag{3.13}$$

where I_{ij}^{IN} is the flow in line ij before the line outage, and $T_{ij,\,i}^{IN}$ is the current transfer distribution factor before the line outage. This injection will zero the flow in line ij and cause the following change in all other lines:

$$\Delta I_{ab} \;=\; -T_{ab,\,i}^{IN}\left(\frac{I_{ij}^{IN}}{T_{ij,\,i}^{IN}}\right) \tag{3.14}$$

With the line flow zeroed, the line ij may be opened without any resulting change in flows. The new network equations with line ij removed have new current transfer distribution factors denoted as $T_{ab,\,i}^{OUT}$. When the injection of Eq. (3.13) is removed (with the line open due to outage) to restore all injections to their original values, the total change in line flow is:

$$\Delta I_{ab} = -T_{ab,\,i}^{IN}\left(\frac{I_{ij}^{IN}}{T_{ij,\,i}^{IN}}\right) + T_{ab,\,i}^{OUT}\left(\frac{I_{ij}^{IN}}{T_{ij,\,i}^{IN}}\right) \tag{3.15}$$

which can be rewritten

$$\Delta I_{ab} \;=\; -T_{ab,\,i}^{IN}\left(\frac{T_{ab,\,i}^{OUT} - T_{ab,\,i}^{IN}}{T_{ij,\,i}^{IN}}\right) I_{ij}^{IN} \tag{3.16}$$

Neglecting resistance again and assuming voltages to be near unity, the LODF is defined as:

$$LODF_{ab,\,ij} = \left(\frac{PTDF_{ab,\,i}^{OUT} - PTDF_{ab,\,i}^{IN}}{PTDF_{ij,\,i}^{IN}} \right) \tag{3.17}$$

with the change in line real power flow in response to a line outage approximated as:

$$\Delta P_{ab} = LODF_{ab,\,ij}\, P_{ij}^{IN} \tag{3.18}$$

An equivalent derivation based upon "DC" load flow assumptions is presented in [16].

3.3 Line Outage Angle Factor (LOAF)

Looking at the bus voltage angle changes due to a line outage, we recall that the voltage changes at buses i and j in response to the injection current change of Eq. (3.13) are

$$\Delta V_i = -Z_{ii} \frac{I_{ij}^{IN}}{T_{ij,\,i}^{IN}} \tag{3.19}$$

$$\Delta V_j = -Z_{ji} \frac{I_{ij}^{IN}}{T_{ij,\,i}^{IN}} \tag{3.20}$$

When the injection change is removed in the outaged system, the bus voltage changes are

$$\Delta V_i = -Z_{ii}^{IN} \frac{I_{ij}^{IN}}{T_{ij,\,i}^{IN}} + Z_{ii}^{OUT} \frac{I_{ij}^{IN}}{T_{ij,\,i}^{IN}} \tag{3.21}$$

$$\Delta V_j = -Z_{ji}^{IN} \frac{I_{ij}^{IN}}{T_{ij,\,i}^{IN}} + Z_{ji}^{OUT} \frac{I_{ij}^{IN}}{T_{ij,\,i}^{IN}} \tag{3.22}$$

The change in voltage between buses i and j due to the outage of line ij is

$$\Delta V_i - \Delta V_j = \left(\frac{Z_{ii}^{OUT} - Z_{ji}^{OUT}}{T_{ij,i}^{IN}} \right) I_{ij}^{IN} - \left(\frac{Z_{ii}^{IN} - Z_{ji}^{IN}}{T_{ij,i}^{IN}} \right) I_{ij}^{IN} \tag{3.23}$$

$$= \left(\frac{Z_{ii}^{OUT} - Z_{ji}^{OUT}}{Z_{ii}^{IN} - Z_{ji}^{IN}} \, \bar{z}_{ij} - \bar{z}_{ij} \right) I_{ij}^{IN} \tag{3.24}$$

Since the original network (with line ij in service) had

$$V_i^{IN} - V_j^{IN} = \bar{z}_{ij} \, I_{ij}^{IN} \tag{3.25}$$

the difference between voltages at buses i and j after line ij is removed is:

$$V_i^{OUT} - V_j^{IN} = \Delta V_i - \Delta V_j + V_i^{IN} - V_j^{IN} \tag{3.26}$$

$$= \left(\frac{Z_{ii}^{OUT} - Z_{ji}^{OUT}}{Z_{ii}^{IN} - Z_{ji}^{IN}} \, \bar{z}_{ij} \right) \bar{z}_{ij} \, I_{ij}^{IN} \tag{3.27}$$

Using the approximations

$$\begin{array}{lllll} cos\,\theta_i & \approx & 1 \qquad I_{ij}^{IN} \approx P_{ij}^{IN} & sin\,\theta_i & \approx \quad \theta_i \\ cos\,\theta_i & \approx & 1 & sin\,\theta_j & \approx \quad \theta_j \end{array} \tag{3.28}$$

and, again neglecting resistance, the angle difference across opened line ij is approximately

$$\theta_i - \theta_j \approx LOAF_{ij} \, P_{ij}^{IN} \tag{3.29}$$

where the Line Outage Angle Factor (LOAF) is defined as

$$LOAF_{ij} = \left(\frac{X_{ii}^{OUT} - X_{ji}^{OUT}}{X_{ii}^{IN} - X_{ji}^{IN}} \right) \bar{x}_{ij} \tag{3.30}$$

$$= \left(\frac{PTDF_{ij,i}^{OUT}}{PTDF_{ij,i}^{IN}} \right) \bar{x}_{ij} \tag{3.31}$$

3.4 Line Outage Generation Factor (LOGF)

Assume for convenience that buses numbered $1, \ldots, m$ are generator terminal buses and $m+1, \ldots, n$ are load buses. In the LODF derivation, the assumption of constant current (power) at each generator reflects the new steady-state condition of constant scheduled output. This will normally not be the case for the small time between when the line is opened and when the controls react to preserve initial set points. During this time, dangerous currents can exist in some of the system generators, causing undesirable shaft torques. To compute these temporary but possibly damaging currents, the generators are appropriately modeled as constant voltages behind their respective transient reactances – an application of the classical dynamic machine model.[2] When a line is opened, the currents immediately change to match the constraint of constant internal generator voltage (both magnitude and angle). The LODF derivation can be directly applied to predict "worst case" internal generator currents. Including each generator's transient reactance into the system admittance matrix enables estimating generator branch current flows at the instant a transmission line is opened. To reflect the constant internal voltage constraint, the analysis proceeds as before with the exception that the CTDFs and changes in generator currents are computed as follows:

1. Add $1/jX'_d$ (generator transient reactance) to the diagonal of the $n\,x\,n$ YBUS (including bus 1 – the swing bus, which by definition includes a generator).

2. Compute the CTDFs per Eq. (3.10) using the full $n\,x\,n$ Z_{BUS} in Eq. (3.11).

[2]The classical model is developed in Section 5.6 of [43].

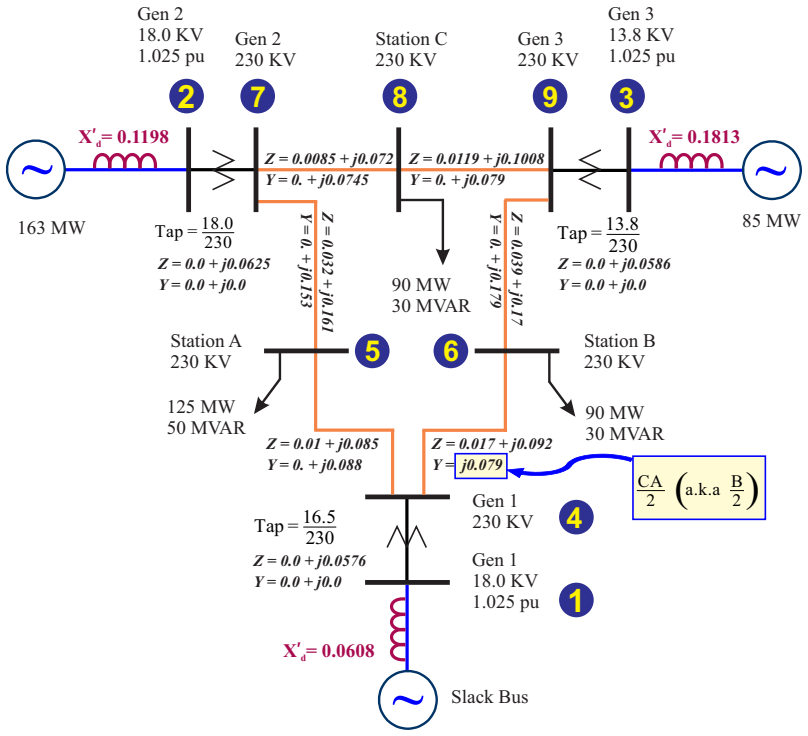

Figure 3.1: Western System Coordinating Council (WSCC) 3-Machine, 9-Bus System modified to show the generator transient reactances.

3. The generator current changes are estimated using Eq. (3.16) with $Z_{ij} = 0$ for subscripts $i, j = n+1, \ldots, n+m$.

The subscripts numbered $n+1, \ldots, n+m$ denote the internal, constant voltage sources behind reactances of the m generators. Since these buses are constant voltage, they are not included in the YBUS (consistent with the reasoning for not including bus 1 in Eq. 3.3).

3.5 Numerical Results

The distribution factors developed were applied to the Western System Coordinating Council (WSCC) 3-Machine, 9-Bus System shown in Fig. 3.1 with generator and exciter parameter data from [43] shown in Table 3.1. The test system uses the π transmission line model (see Fig. 3.2). The validity of simplifying assumptions for the 9-bus test system with all possible transmission line loss cases was tested; the results are shown in Fig. 3.3. In Fig. 3.3a,

Table 3.1: Generator and exciter parameter data, WSCC 3-Machine, 9-Bus System

Generator Data				
	Generator 1	Generator 2	Generator 3	
$H\ (s)$	23.64	6.4	3.01	scaled shaft inertia
$X_d\ (pu)$	0.146	0.8958	1.3125	d-axis reactance
$X_d^{'}\ (pu)$	0.0608	0.1198	0.1813	d-axis transient reactance
$X_q\ (pu)$	0.0969	0.8645	1.2578	q-axis reactance
$X_q^{'}\ (pu)$	0.0969	0.1969	0.2500	q-axis transient reactance
$T_{do}^{'}\ (s)$	8.96	6.0	5.89	d-axis transient time constant
$T_{qo}^{'}\ (s)$	0.31	0.535	0.6	q-axis transient time constant

Exciter Data				
	Exciter 1	Exciter 2	Exciter 3	
K_A	20	20	20	pilot exciter amplifier gain
$T_A\ (s)$	0.2	0.2	0.2	pilot exciter amplifier time constant
K_E	1.0	1.0	1.0	main exciter gain
$T_E\ (s)$	0.314	0.314	0.314	main exciter time constant
K_F	0.063	0.063	0.063	stabilizing transformer gain
$T_F\ (s)$	0.35	0.35	0.35	stabilizing transformer time constant

the pre-outage bus voltages computed using the "π" and "reactance only" transmission line models are compared; the simpler "reactance only" solution tracks the "π" solution closely with the difference being typically less than five percent. As shown in Fig. 3.3b, the bus voltages were approximately 1 pu in all outage cases; the greatest bus voltage difference was approximately 15 percent.

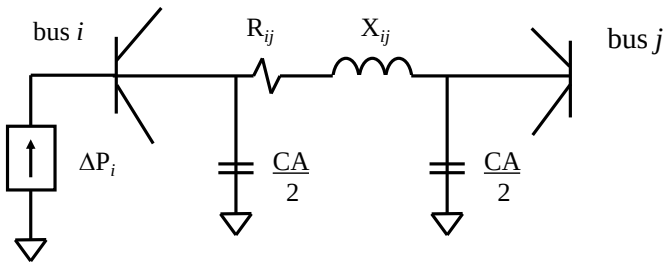

Figure 3.2: "Pi" (π) transmission line model. In the LODF development, resistance, R_{ij}, and charging admittance, $\frac{1}{2}\ CA_{ij}$, are assumed to be negligible, leaving a much simplified series–reactance–only (X_{ij}) transmission line model.

Line power flow results using non-linear power flow solution (both π and reactance-only transmission lines) and the Line Outage Distribution Factor (LODF) contingency estimate

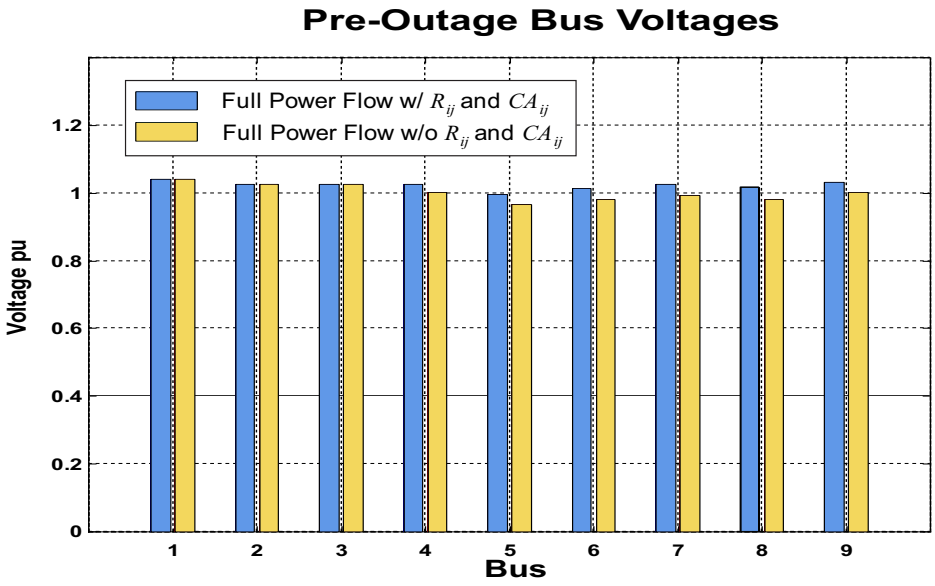

(a) Validating the "fast decoupled power flow" technique assumption that transmission line resistance, R_{ij}, and charging admittances, $\frac{1}{2}CA_{ij}$ can be neglected. Visual inspection shows that full power flow solutions for "π" and "reactance only" transmission line models track closely.

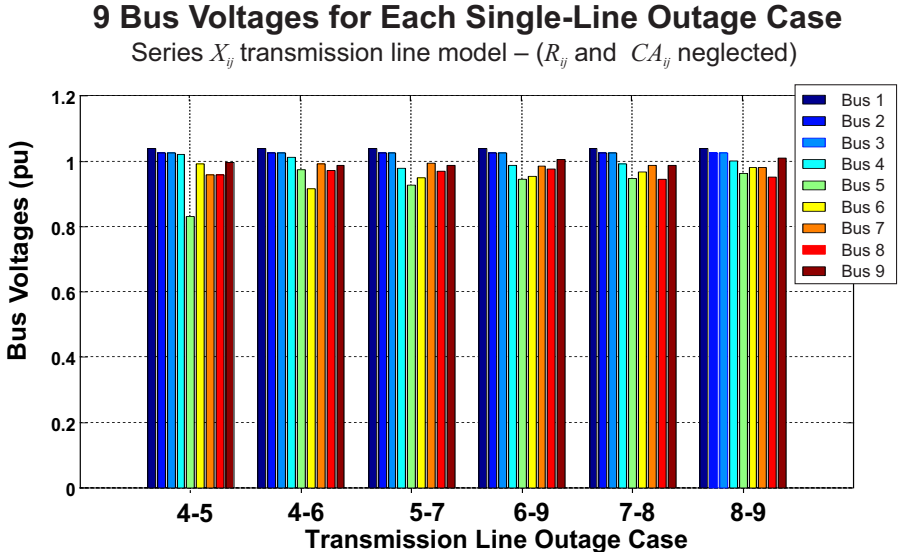

(b) Validating the "fast decoupled power flow" technique assumption that node voltage solutions are approximately 1 pu for transmission line outage cases when transmission lines are modeled as series reactances; R_{ij} and $\frac{1}{2}CA_{ij}$ are neglected. Visual inspection shows the assumption is valid; the greatest bus voltage deviation from 1pu was less than 15 percent.

Figure 3.3: "Fast decoupled power flow" technique assumptions validation for transmission line outage cases of the WSCC 3-Machine, 9-Bus System.

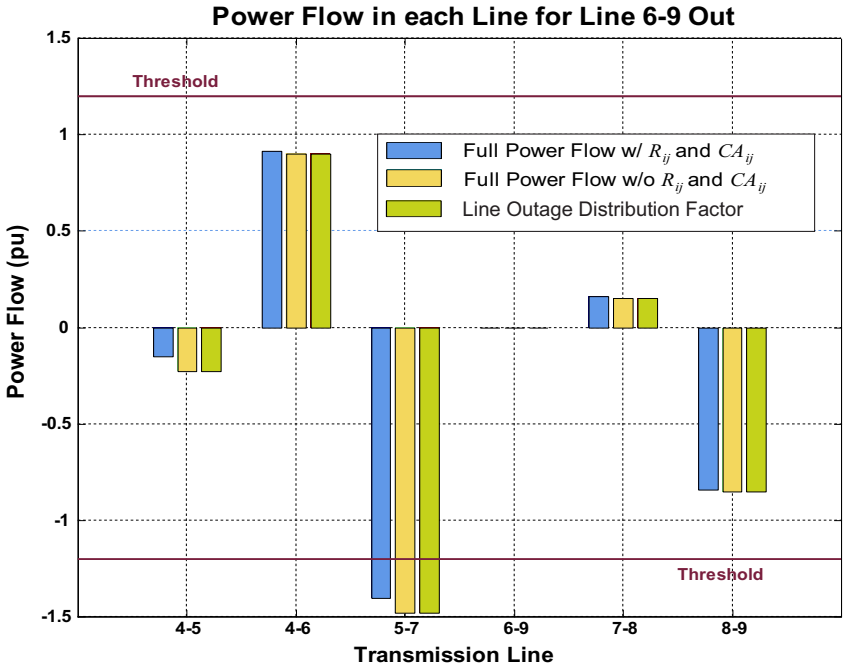

Figure 3.4: Line power flow comparison of power flow solutions and Line Outage Distribution Factor (LODF) contingency estimate for line 6–9 open. The negative power flow indicates the direction of power flow changed when line 6–9 was removed from service.

are shown in Fig. 3.4. The transmission line 6–9 out contingency case produced the most dramatic changes from the base case, but this result is, nonetheless, similar to the other transmission line outage case results. The power flow on line 5–7 exceeds a line power flow threshold policy, which has been arbitrarily set for illustrative purposes. Note the LODF contingency estimates closely follow the full power flow solutions for both the π and reactance-only transmission line models, demonstrating the LODF technique's efficacy for computing a solution estimate.

Computing the LODF contingency case estimate requires significantly fewer floating-point operations than computing a full power flow solution. MATLAB counted 45,000 floating point operations (flops) for the full power flow solution program custom written to test the transfer distribution factors developed herein. Each line outage contingency case solved using the full power flow solution required a similar number of floating point operations. In contrast, the distribution factor contingency solver required approximately

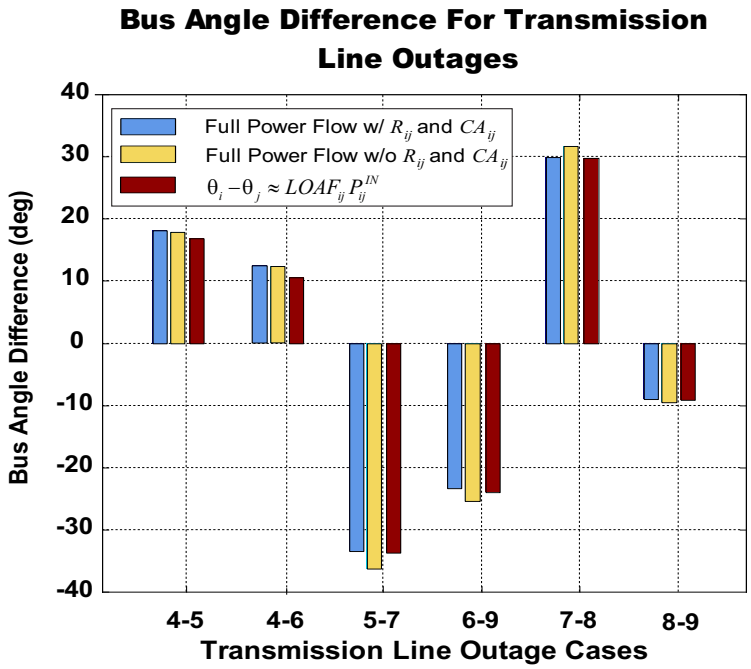

Figure 3.5: Comparison of four bus angle solution methods for each transmission line outage case: (1) π transmission line full power flow solution, (2) series reactance transmission line full power flow solution, (3) angle differences computed using Eq. (3.29). The contingency estimate tracks the full power flow solutions closely, demonstrating the efficacy of the LOAF distribution factor.

1500 flops to estimate the power flows for each transmission line outage. To perform a full power flow analysis for every line outage would require 6 x 45k flops (270k flops), whereas the contingency solver uses 45k flops (solving for the base case) plus six contingencies x 1,500 flops (54k flops). So in this comparison, the transfer distribution factor contingency solver required 20 percent of the flops required to compute the six contingencies using the full power flow solution program.

Results for angle difference across open transmission lines using non-linear power flow solution (both π and reactance-only transmission lines) and Line Outage Angle Factor (LOAF) are shown in Fig. 3.5. The LOAF contingency estimates closely follow the power flow solutions. In each case, the difference between the linear angle factors estimate and the full power flow solution was less than 15 percent. Thus, the LOAF contingency factor provides a low-computational-burden alternative for screening angle differences that exceed the line

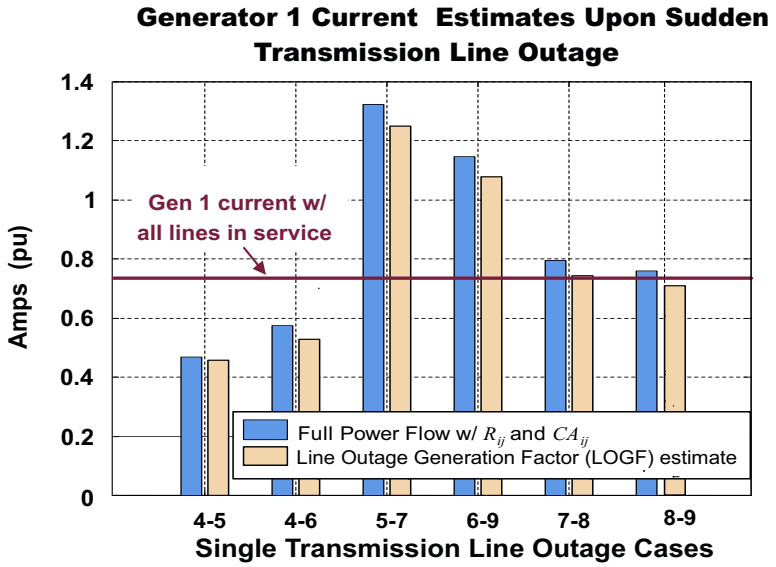

Figure 3.6: Generator 1 post-opening current estimates for each transmission line outage case compared to the pre-opening generator current. Note the Line Outage Generator Factor (LOGF) estimates closely track full power flow solution results, offering a "computationally light" alternative to a full power flow solution.

closing angle difference policy.

The internal generator current results using non-linear power flow solution (both and reactance only transmission lines) and LOGF contingency estimate are shown in Fig. 3.6. Again, the LOGF contingency estimates closely follow the full solution validating the method. The LOGF contingency factor provides a computationally practical method for screening line closures that may give rise to damaging internal generator current surges.

Chapter 4

Thevenin Equivalents to Estimate Steady-State Stability

Electric power systems have well-documented transmission line power transfer capacity limits. A continuing challenge is real-time operator awareness of the power system's state versus known operating limits. Today, the power system's state is estimated several times per hour, which guides power system operators to continually balance power and generation to maintain very reliable, stable system operation. Meeting these high expectations requires conservative power system operation to protect against uncertainties and unexpected system conditions, which might lead to power system loadability violations. The Smart Grid initiative is bringing a synchrophasor data network on-line that will provide near-real-time, precisely synchronized bus voltage, current, and power measurements that open the door to advance from estimate-based to measurement-based power system energy management.[1]

This chapter investigates using synchrophasor measurements from two buses to compute model parameters for a pair of Thevenin sources, which with the connecting transmission line parameters enable a two-bus equivalent power system representation. The difference between the resulting Thevenin equivalent source angles is proposed as an indicator of the system's proximity to its stability limits. The largest Thevenin equivalent source angle difference among the connected bus pairs in the system becomes an indicator of the risk of losing system stability. This approach offers the possibility of a simple, near-real-time system stability assessment without requiring system-wide state measurements, complex system models, and powerful computer systems.

[1]This line of investigation was first reported by Reinhard, Sauer, and Dominguez-Garcia in [56].

4.1 Preliminaries

Many factors restrict power system operations. Among them are the thermal, voltage, and stability transmission line limitations. Short lines are thermally limited; medium length lines are voltage drop limited; and long lines are stability limited. Harry P. St. Clair provided empirical line loadability limits in what have become known in the power industry as the St. Clair Curves [57]. These loadability limit notions are rooted in well understood phenomena. Thermal and voltage constraints are set by line currents and bus voltages respectively – both easily measured. The stability constraint related to phase angle differences is more difficult to measure; the constraint is simply illustrated in the relationship between bus 1 and bus 2 real power flows on a lossless line with voltage support on both ends, which is given by

$$P_{12} = \frac{V_1 V_2}{X_{12}} \sin(\theta_1 - \theta_2) \tag{4.1}$$

where X_{12} is the line series reactance and $V_1 \angle \theta_1$ and $V_2 \angle \theta_2$ are the respective bus voltage magnitudes and phase angles. Maximum power flow is reached when the voltage phase angle difference, $\theta_1 - \theta_2$, between the buses reaches 90 degrees; beyond this angle difference, it is well known that the system is no longer steady-state stable. The authors in [21] validated and extended St Clair line loadability limits to extra-high voltage lines using numerical techniques – providing the St. Clair curves shown in Fig. 4.1.[2] This chapter uses a π equivalent transmission line with Thevenin equivalent models on the sending and receiving ends; it also uses 45 degrees as the stability margin limit. A similar approach for detecting loadability constraints is proposed in [58]. The authors in [32] and [35] propose using local current and voltage measurements to compute Thevenin equivalent circuits.

The St. Clair curves and the application of Thevenin equivalent models form the basis for the ideas advanced in this chapter. Consequently, we envision that our Thevenin equivalent application will retain the notions of thermal, voltage-drop, and stability constraints.

[2] Adapted from the Fig. 1 in [21]

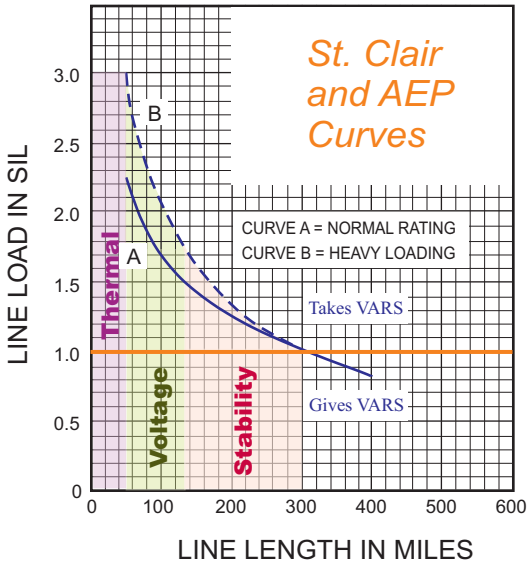

Figure 4.1: St. Clair and American Electric Power (AEP) curves. [57, 21]

Whereas Thevenin equivalents have previously been used to determine line loadability limits, this paper proposes using equivalents to gauge proximity to loadability limits. Our goal is to compute a real-time "angle across the system" (AnglxSys) for each line using Thevenin equivalents. These equivalents are obtained from synchrophasor measurements. Our conjecture is that when the power system is nearing its loadability limit, the AnglxSys for at least one line will be approaching 90 degrees. In this paper, the analysis and results focus on the methods and feasibility of computing the AnglxSys for a given line using actual synchrophasor data.

4.2 Thevenin Equivalents from Synchrophasors

4.2.1 Two-Bus Thevenin Equivalent I

Per conjecture, the AnglxSys as seen from two buses connected to opposing ends of a transmission line is a preeminent indicator of the system's proximity to its steady-state stability limit – the most difficult to determine of the three stability indicators listed above. The objective is to develop a Thevenin equivalent circuit representation composed of an equivalent

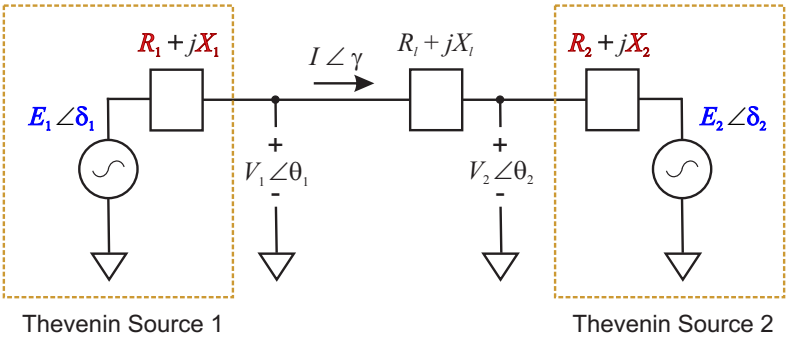

Figure 4.2: Thevenin equivalent circuit model.

voltage source (voltage magnitude and angle) and impedance, which characterizes the power system's behavior as seen from the end of a particular transmission line. The boxed portion of the circuit in Fig. 4.2 represents such a Thevenin equivalent of the power system looking into bus 1. The transmission line connecting buses 1 and 2 is modeled by the known line impedance, $R_l + jX_l$. A second Thevenin equivalent representing the power system behind the terminals at bus 2 completes the proposed circuit. In this model, we have neglected the shunt elements.

The challenge is to develop a reliable, accurate method for determining Thevenin equivalent circuit parameters from field measurements. In particular, we propose using synchrophasor data measured by phasor measurement units (PMUs) at two connected bus terminals of interest to compute two Thevenin equivalent circuits. The proposed Thevenin equivalent stability indicator (the difference between the Thevenin source angles) could be easily computed from PMU measurements. This would allow power system operators to continuously monitor the AnglxSys and use it to gauge proximity to unstable conditions.

The common method for finding a Thevenin equivalent circuit is to measure the open circuit voltage, V_{oc}, and the short circuit current, I_{sc}, across the terminal pair. These voltage and current values determine the axis crossings; the slope of the line connecting the two axis crossings is the Thevenin equivalent impedance. Figure 4.3a shows a Thevenin equivalent circuit characteristic for a purely resistive circuit. Unfortunately, in practice it is impossible to measure V_{oc} and I_{sc} while the line is in operation. Assuming the power system

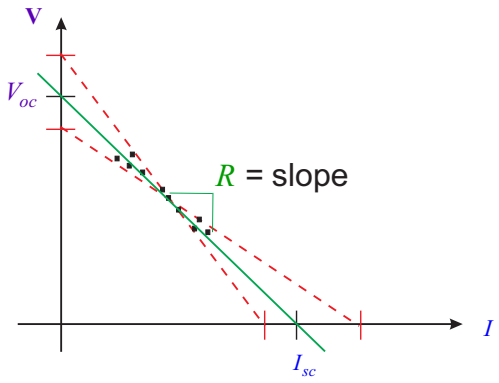

(a) Real power Thevenin equivalent – resistance only.

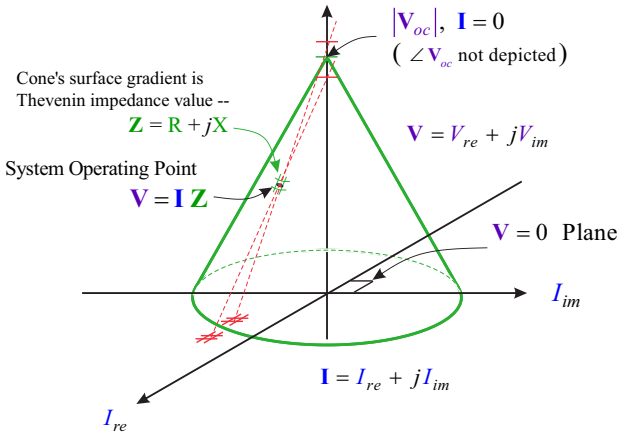

(b) Complex power Thevenin equivalent – resistance and reactance.

Figure 4.3: Thevenin equivalent I-V characteristics.

$I - V$ relationship is nearly linear in the anticipated operating range, a Thevenin equivalent (green line) could be determined by measurements. Determining the equivalent circuit is complicated by noise in PMU voltage and current measurements, which conceptually will result in a range of Thevenin equivalent parameter extremes as indicated by the dashed orange lines crossing the respective axes. This prompts the caveat that poorly conditioned data may result in large equivalent parameter value swings between data sets collected under nearly identical operating conditions. A Thevenin equivalent circuit with energy storage elements (inductive and capacitive) needed to model an AC electric power system would add two more dimensions to span the solution space. This extended Thevenin equivalent can be visualized, in part, in three dimensions – see Fig. 4.3b. The usefulness of the Thevenin equivalent depends upon the how well the physical system behavior can be represented by a linear model.

Consider the Thevenin source 1 circuit in Fig. 4.2; in order to simplify the notation in subsequent developments, the sub-index 1 is dropped from all the variables. The relation

between the variables is described by the complex equation

$$E\angle\delta = I\angle\gamma \cdot (R + jX) + V\angle\theta \tag{4.2}$$

By writing the complex variables in Cartesian form, i.e.

$$\begin{aligned} E\angle\delta &= E_r + jE_i \\ I\angle\gamma &= I_r + jI_i \\ V\angle\theta &= V_r + jV_i \end{aligned} \tag{4.3}$$

we obtain an equivalent pair of equations:

$$E_r = R\,I_r - X\,I_i + V_r \tag{4.4}$$

$$E_i = X\,I_r - R\,I_i + V_i \tag{4.5}$$

Note that in Eq. (4.2) and its equivalent pair in Eqs. (4.4) and (4.5), there are four unknown variables: real and imaginary Thevenin source terms, E_r and E_i, and unknown constitutive impedance, consisting of resistance R and reactance X. There are multiple approaches to solving the Thevenin equivalent problem: (i) use a set of two sequential PMU measurements to enable an exact solution, (ii) use three or more sequential measurements to find a least squares estimate (LSE), and (iii) reduce the number of unknowns by fixing one or more of the four unknown values.

The exact solution requires 2 consecutive measurement sets, which results in 4 equations and 4 unknowns. This equation set can be in $Ax =$ b matrix form as

$$\begin{bmatrix} 1 & 0 & -I_{r_{(1)}} & I_{i_{(1)}} \\ 0 & 1 & -I_{i_{(1)}} & -I_{r_{(1)}} \\ 1 & 0 & -I_{r_{(2)}} & I_{i_{(2)}} \\ 0 & 1 & -I_{i_{(2)}} & -I_{r_{(2)}} \end{bmatrix} \begin{bmatrix} E_r \\ E_i \\ R \\ X \end{bmatrix} = \begin{bmatrix} V_{r_{(1)}} \\ V_{i_{(1)}} \\ V_{r_{(2)}} \\ V_{i_{(2)}} \end{bmatrix} \tag{4.6}$$

Table 4.1: Sample Synchrophasor Data.

Time (s)	V_1 (KV)	θ_1 °	$P_{1->2}$ MW at Bus 2	$Q_{1->2}$ MVAR at Bus 2	V_2 (KV)	θ_2°
0.00	759.26	62.286	2409.4	-542.98	762.76	60.724
0.10	759.27	62.405	2409.4	-542.98	762.77	60.841
0.20	759.27	62.524	2409.4	-542.98	762.76	60.963
0.30	759.33	62.642	2409.4	-542.98	762.77	61.079
0.40	759.31	62.758	2409.4	-542.98	762.76	61.193
0.50	759.26	62.876	2409.4	-542.98	762.73	61.312
0.60	759.23	62.989	2409.4	-542.98	762.68	61.427
0.70	759.18	63.107	2409.4	-542.98	762.64	61.543
0.80	759.18	63.223	2409.4	-542.98	762.66	61.66
0.90	759.21	63.343	2409.4	-542.98	762.65	61.779
1.00	759.19	63.456	2409.4	-542.98	762.65	61.892
1.10	759.2	63.572	2409.4	-542.98	762.65	62.011
1.20	759.19	63.685	2409.4	-542.98	762.63	62.121
1.30	759.16	63.803	2409.4	-542.98	762.63	62.24
1.40	759.15	63.916	2409.4	-542.98	762.61	62.356
1.50	759.13	64.035	2409.4	-542.98	762.63	62.47
1.60	759.16	64.151	2409.4	-542.98	762.61	62.585
1.70	759.16	64.264	2409.4	-542.98	762.64	62.699
1.80	759.19	64.38	2409.4	-542.98	762.63	62.814
1.90	759.18	64.498	2409.4	-542.98	762.62	62.93
2.00	759.16	64.726	2409.4	-542.98	762.65	63.159

with the first and second data measurement sets indicated in parentheses. From a purely mathematical standpoint, this would appear to solve the problem provided that the left-hand matrix is invertible, which depends upon measured data characteristics.

Numerical Results

Table 4.1 shows a typical synchrophasor data set for a 765 kV transmission line that includes line-to-line voltage magnitude and phase angle. Power is flowing from bus 1 to bus 2. As is typical of a power system, the measured frequency varies just under 0.02 Hz from the nominal 60 Hz system frequency, which accounts for the voltage angles' slow rotation. The real and reactive power flows allow calculation of current magnitude and angle. For calculations, the sample data was normalized and converted to per phase, per unit data for calculations. Typically, the data values over short time periods showed only small changes. For example, the per unit voltage measurement mean over 2400 measurements (10 measurements per second) was 1.0003 with variance $7.062 \cdot 10^{-8}$ pu. The per unit current measurement calculated from the data showed similar stability with mean .9587 and variance $1.251 \cdot 10^{-5}$ pu.

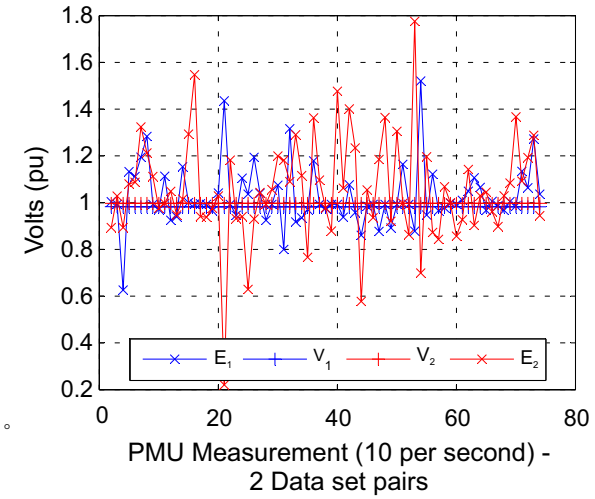

(a) Numerical Thevenin source magnitudes.

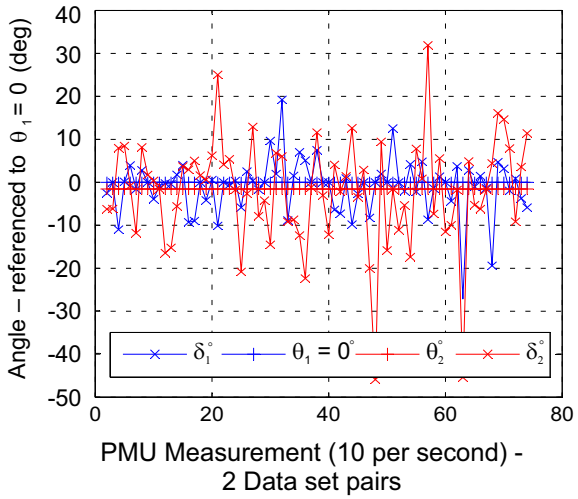

(b) Numerical Thevenin source phase angles.

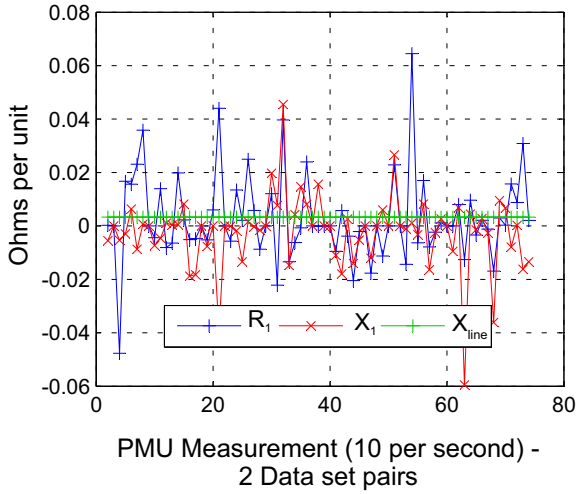

(c) Numerical Thevenin resistance and reactance.

Figure 4.4: Exact Thevenin source solutions.

We applied the exact solution approach to the data outlined above. The calculated Thevenin source magnitudes, phase angles, and impedances are shown respectively in Figs. 4.4a, 4.4b, and 4.4c. The computed Thevenin source parameter values were striking in their wildly erratic swings, which run counter to intuition and cast doubt on the value of computations for modeling system behavior. For instance, the Thevenin source magnitudes are expected to be close to 1.0 per unit and certainly to not swing across a range exceeding 1.0 pu. Similarly, the phase angle relationships are not consistent with power flow from source

1 to source 2, i.e. that the voltage phase angles be characterized by $\delta_1 > \theta_1 > \theta_2 > \delta_2$. Finally, the impedance values not only rapidly swing, but also improbably take on negative values, which is difficult to accept or justify. As outlined in the next section, we found that the erratic Thevenin parameter behavior was attributable to sample synchrophasor data characteristics.

Matrix Condition Numbers

2 measurement pairs

Consider the matrix on the left-hand side of Eq. (4.6):

$$A = \begin{bmatrix} 1 & 0 & -I_{r_{(1)}} & I_{i_{(1)}} \\ 0 & 1 & -I_{i_{(1)}} & -I_{r_{(1)}} \\ 1 & 0 & -I_{r_{(2)}} & I_{i_{(2)}} \\ 0 & 1 & -I_{i_{(2)}} & -I_{r_{(2)}} \end{bmatrix} \tag{4.7}$$

The condition number of A is an important measure of the sensitivity of the solution

$$x = [\, E_r \;\; E_i \;\; R \;\; X \,]^T \tag{4.8}$$

to small perturbations in the measurement vector

$$b = \begin{bmatrix} V_{r_{(1)}} & V_{r_{(1)}} & V_{r_{(2)}} & V_{i_{(2)}} \end{bmatrix}^T \tag{4.9}$$

To simplify the representation of A^{-1}, represent the terms $I_{r_{(1)}},\ I_{i_{(1)}},\ I_{r_{(2)}},\ I_{r_{(2)}}$ respectively by $a,\ b,\ c,\ d$ so that

$$A = \begin{bmatrix} 1 & 0 & -a & b \\ 0 & 1 & -b & -a \\ 1 & 0 & -c & d \\ 0 & 1 & -d & -d \end{bmatrix}$$

The inverse of A is given by the comparatively complex expression

$$A^{-1} = \begin{bmatrix} 1 + \frac{-b\,(a-c)+a[(b-d)-(a-c)\,f]}{(a-c)^2} & \frac{b}{(b-d)\,f} - \frac{a}{(a-c)\,f} & \frac{b\,(a-c)+a[(d-b)+(a-c)\,f]}{(a-c)^2 f} & -\frac{b}{(b-d)\,f} + \frac{a}{(a-c)\,f} \\ \frac{a\,(a-c)+b[(b-d)-(a-c)\,f]}{(a-c)^2 f} & 1 - \frac{a}{(b-d)\,f} - \frac{b}{(a-c)\,f} & \frac{-a\,(a-c)+b[(a-c)\,f-(b-d)]}{(a-c)^2 f} & \frac{a}{(b-d)\,f} + \frac{b}{(a-c)\,f} \\ \frac{(b-d)-(a-c)\,f}{(a-c)^2 f} & \frac{-1}{(a-c)\,f} & \frac{(a-c)\,f-(b-d)}{(a-c)^2 f} & \frac{1}{(a-c)\,f} \\ \frac{1}{(a-c)\,f} & \frac{-1}{(b-d)\,f} & \frac{-1}{(a-c)\,f} & \frac{1}{(b-d)\,f} \end{bmatrix} \tag{4.10}$$

where

$$f = \frac{(a-c)^2+(b-d)^2}{(a-c)(b-d)}$$

The condition number is defined for the norm p as

$$K(A) = \|A\|_p \left\|A^{-1}\right\|_p \tag{4.11}$$

The L_1 ($p = 1$, maximum absolute column sum) and L_∞ ($p = \infty$, maximum absolute row sum) norms are easily computed to provide accurate condition number order of magnitude estimates. A desirable matrix condition number is close to one, in which case small measurement errors have negligible impact upon the solution. In contrast, a very large matrix condition number amplifies small measurement errors to substantially affect the computed solution. Using the synchrophasor data in Table 4.1, the L_1 and L_∞ norms of A^{-1} are easily estimated. The differences between sequential real and imaginary current measurements are

both very small, such that

$$\left(I_{i_{(1)}} - I_{i_{(2)}}\right) = (b - d) \sim 10^{-3} \tag{4.12}$$

$$\left(I_{i_{(1)}} - I_{i_{(2)}}\right) = (b - d) \sim 10^{-3} \tag{4.13}$$

$$f = \frac{(a-c)^2 + (b-d)^2}{(a-c)(b-d)} \sim \frac{(10^{-3})^2 + (10^{-3})^2}{(10^{-3})(10^{-3})} \sim 1 \tag{4.14}$$

which results in $\|A\|_1 \sim \|A\|_\infty \sim 1$ and $\|A^{-1}\|_1 \sim \|A^{-1}\|_\infty \sim 10^3$. The resulting condition numbers are much greater than the ideal condition number that is close to 1, in particular:

$$K(A) = \|A\|_p \left\|A^{-1}\right\|_p \sim 10^3 \tag{4.15}$$

The consequence of the condition number being on the order of 10^3 is that small perturbations in b may disproportionately change the calculated solution, casting doubt on the accuracy of computed results. We found that the sample data matrices had condition numbers on the order of 10^5, as shown in Fig. 4.5. The impact of these extremely large condition numbers is evident in the dramatic Thevenin parameter swings in Figs 4.4a, 4.4b, and 4.4c.

More than 2 measurement pairs

We also considered using an LSE solution to reduce the Thevenin parameter swings. The LSE solution incorporates additional data pairs, generating a rectangular $m \times n$ matrix with $m > n$. The condition number can be computed using the ratio of the largest to smallest of the ordered singular values, σ_i, obtained from the singular value decomposition of the matrix A. The condition number is

$$K(A) = \frac{\sigma_1}{\sigma_n}, \quad \sigma_1 > \ldots > \sigma_i > \ldots > \sigma_n \tag{4.16}$$

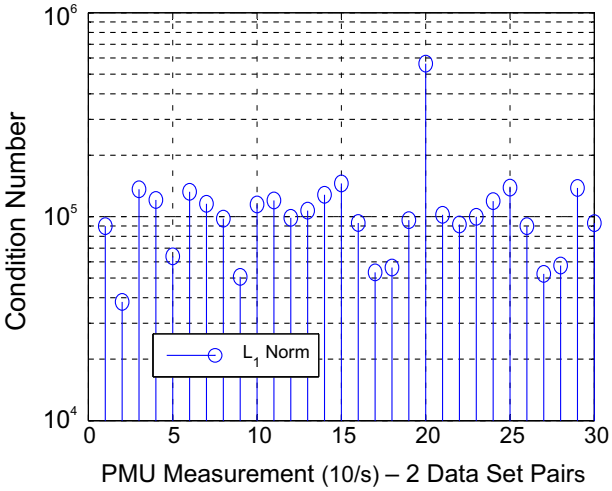

Figure 4.5: Sample condition numbers for 30 consecutive Thevenin parameter data set pairs.

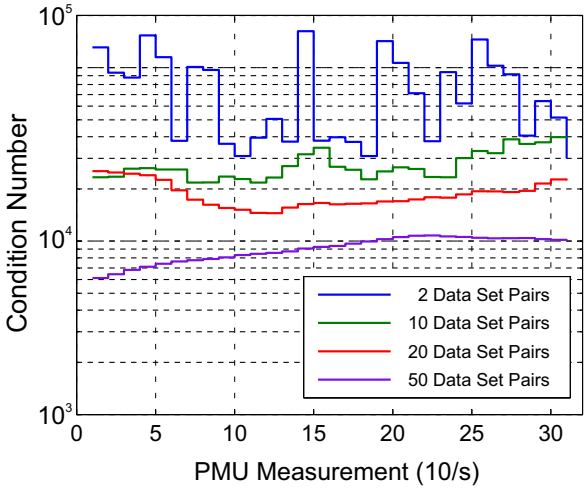

Figure 4.6: Least squares error estimate condition numbers computed using 2, 10, 20, and 50 sequential synchrophasor data frames to provide best estimates of two data points to compute solution vector x in Eq. (4.8) .

Unlike the fully determined system in Eq. (4.7), a straightforward estimate of the over-determined system's condition number is very difficult to derive. To determine whether the LSE solution improved the problem's conditioning, we used MATLAB to compute condition numbers for overdetermined matrices constructed from 10, 20, and 50 sample data set pairs. The results in Fig. 4.6 clearly show that the condition number does not appreciably improve even using 50 data set pairs, and that synchrophasor data does not lend itself well to this approach to computing a Thevenin equivalent. Further, Fig. 4.7 shows that while the Thevenin source phases do not swing erratically, they also do not satisfy the fundamental condition $\delta_1 > \theta_1 > \theta_2 > \delta_2$ that is characteristic of power flowing from source 1 to source 2.

4.2.2 Two-Bus Thevenin Equivalent II

Figure 4.8 shows an alternative Thevenin equivalent model. In this model, we fix the source magnitudes $|E_1| = |E_2|$ to 1 pu and specify that the Thevenin equivalent impedances be purely reactive, i.e. $R_1 = R_2 = 0$. Note that this circuit model carries forward the as-

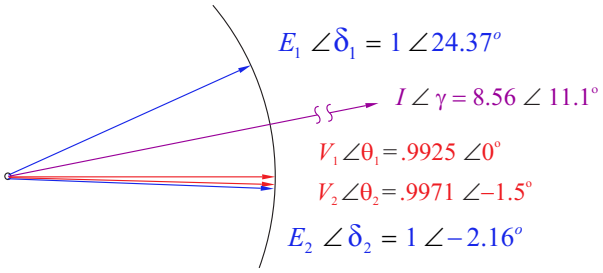

Figure 4.7: Overdetermined Thevenin source phase angles.

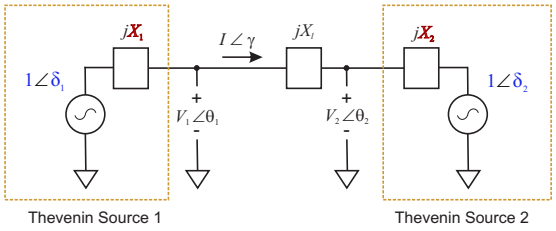

Figure 4.8: Simplified Thevenin equivalent model.

sumption that current flows through shunt capacitances are negligible; consequently, the two Thevenin source terminals share the same current. The Thevenin source 1 reactance, X_1, is determined by

$$1\angle\delta_1 = I\angle\gamma \cdot (jX_1) + V_1\angle\theta_1 \tag{4.17}$$

Decomposing Eq. 4.17 into its real and imaginary equations, the δ_1 term can be eliminated using the trigonometric identity

$$\sin\,\delta_1 = \sqrt{1 - \cos^2\delta_1} \tag{4.18}$$

which results in the quadratic equation

$$I^2X_1^2 - 2V_1I\,\sin(\gamma)\,X_1 - (V_1^2 - (1)^2) = 0 \tag{4.19}$$

with two possible solutions:

$$X_1 = \frac{1}{I}\left[V_1\sin(\gamma - \theta_1) \pm \sqrt{(1)^2 - V_1^2\cos^2(\gamma - \theta_1)}\right] \tag{4.20}$$

Similarly, we determine Thevenin source 2 reactance, X_2,

$$V_2\angle\theta_2 = I\angle\gamma \cdot (jX_2) + 1\angle\delta_2 \tag{4.21}$$

which yields two possible X_2 solutions of very similar form

$$X_2 = \frac{1}{I}\left[-V_2 \sin(\gamma - \theta_2) \pm \sqrt{(1)^2 - V_2^2 \cos^2(\gamma - \theta_2)}\right] \tag{4.22}$$

The Thevenin source angles are determined by writing the system power balance equation

$$1\angle\delta_1 \left(I\angle\gamma\right)^* = j(X_1 + X_l + X_2)\, I^2 + 1\angle\delta_2 \cdot \left(I\angle\gamma\right)^* \tag{4.23}$$

The real power equation reduces to $\cos(\delta_1 - \gamma) = \cos(\delta_2 - \gamma)$, which is satisfied if $\delta_1 = \delta_2$ (a trivial solution with no power flow); alternatively, since $\cos(\alpha) = \cos(-\alpha)$,

$$\delta_2 = 2\gamma - \delta_1 \;\equiv\; \gamma = \frac{\delta_1 + \delta_2}{2} \tag{4.24}$$

is also a solution. Using these relationships, we obtain

$$\delta_1 = \gamma + \sin^{-1}\left(\frac{(X_1 + X_l + X_2)\, I}{2}\right) \tag{4.25}$$

$$\delta_2 = \gamma - \sin^{-1}\left(\frac{(X_1 + X_l + X_2)\, I}{2}\right) \tag{4.26}$$

To compensate for the slow rotation of the phasor measurements due to the slight difference between the actual system frequency and the ideal 60 Hz frequency, the voltage angle at bus 1 is set to 0 (i.e. $\theta_1' = 0 = \theta_1 - \theta_1$) and all other angles are adjusted by subtracting θ_1.

The effectiveness of these relationships was tested using the data set from which Table 4.1 is extracted. The resulting Thevenin source angle values and computed reactances are shown in Table 4.2. Note that the X_1 and X_2 solutions are each composed of a pair of positive and negative reactance values; also, the four possible solutions show interesting symmetries. We confirmed that these solutions provided near-zero KVL residuals around each source loop and around the system loop; however, only the two positive reactance solutions resulted in

Table 4.2: Computed Thevenin Source Parameters*, $\gamma = 11.1^o$.

δ_1^o	X_1	X_l	X_2	X_{total}	δ_2^o
-2.179	-.0043	.0034	-.0546	-.0555	24.37
10.95	.0506	.0034	-.0546	-.0006	11.25
11.22	-.0043	.0034	.0016	.0007	10.96
24.35	.0506	.0034	.0016	.0556	-2.161

*Thevenin source values at $t = 1$ s averaging 10 PMU measurements. Angles and reactance are in degrees and ohms per unit respectively.

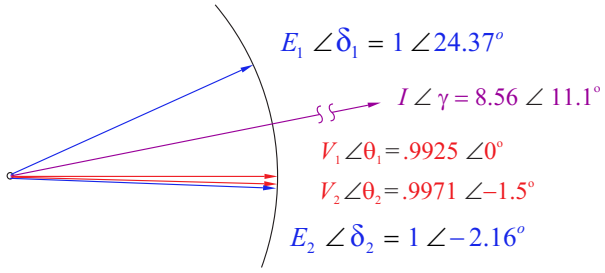

(a) Thevenin source values at $t = 1$ s averaging 10 synchrophasor measurements.

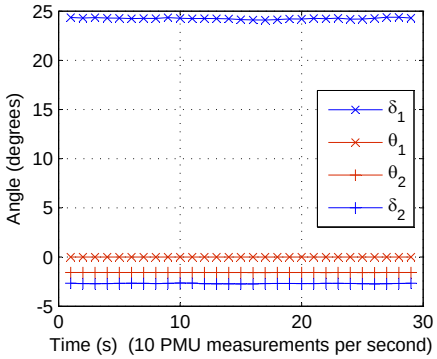

(b) Voltage phase angles using sets of 10 averaged synchrophasor measurements.

Figure 4.9: Thevenin source phase angle results using the positive X_1 and X_2 solutions, $\gamma = 11.1^o$.

the expected power flows based upon the relative phase angle relationships of the source and terminal voltages, i.e. $\delta_1 > \theta_1 > \theta_2 > \delta_2$. In the other three X_1 and X_2 solution combinations, the phase angle order is violated. The phase angle relations for the positive X_1 and X_2 solutions are shown in Fig. 4.9.

This model was consistent with expected system behavior in every respect. The solution satisfied three KVL loop equations with small residuals – one through each source and its corresponding terminals and a loop around the total system. Additionally, the real and reactive powers computed at each source and terminal were consistent with expected real and reactive power flows. Further, the Thevenin equivalent solution showed results that varied no more quickly than the phasor measurements. Consequently, this model and Thevenin

equivalent computational approach warrant further investigation for applications assessing power system stability.

4.3 Heuristic View – Exploitable Linear Behaviors

The challenges encountered developing a satisfactory Thevenin equivalent model from field measurements raise questions about whether the inherently non-linear power system has linear characteristics that can be exploited. This suggests studying series of non-linear power flow solutions of a power system under progressively increasing stress – to the point of system failure. The object is to seek linear or near-linear characteristics that might be exploited to produce Thevenin equivalent models from PMU field measurements to compute a real-time "angle across the system" (AnglxSys).

4.3.1 Proposed Power Flow Solution-based Thevenin Equivalent

Consider the Thevenin source model for bus injecting power into the line as shown in Fig. 4.10. The relationship between the complex variables is described by

$$E_{send}\angle\delta_{send} = I\angle\gamma \cdot (R_{send} + jX_{send}) + V_{send}\angle\theta_{send} \tag{4.27}$$

which can be rewritten as

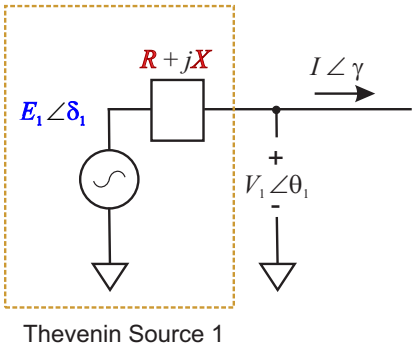

Figure 4.10: Thevenin source model for PowerWorld.

$$
\begin{aligned}
R_{send} + jX_{send} &= \frac{E_{send}\angle\delta_{send} - V_{send}\angle\theta_{send}}{I\angle\gamma} \\
&= \frac{E_{send}}{I}\angle\left(\delta_{send} - \gamma\right) - \frac{V_{send}}{I}\angle\left(\theta_{send} - \gamma\right) \\
&= \frac{E_{send}}{I}\left[\cos\left(\delta_{send} - \gamma\right) + j\sin\left(\delta_{send} - \gamma\right)\right] - \ldots \\
&\qquad \ldots - \frac{V_1}{I}\left[\cos\left(\theta_{send} - \gamma\right) + j\sin\left(\theta_{send} - \gamma\right)\right]
\end{aligned}
\tag{4.28}
$$

Separating the real and imaginary components:

$$
\begin{aligned}
R_{send} &= \frac{1}{I}\left[E_{send}\cos\left(\delta_{send} - \gamma\right) + V_{send}\cos\left(\theta_{send} - \gamma\right)\right] \\
X_{send} &= \frac{1}{I}\left[E_{send}\cos\left(\delta_{send} - \gamma\right) + V_{send}\sin\left(\theta_{send} - \gamma\right)\right]
\end{aligned}
\tag{4.29}
$$

Similar relationships are developed for the bus receiving power from the line such that

$$
\begin{aligned}
R_{receive} &= \frac{1}{I}\left[E_{receive}\cos\left(\delta_{receive} - \gamma\right) + V_{receive}\cos\left(\theta_{receive} - \gamma\right)\right] \\
X_{receive} &= \frac{1}{I}\left[E_{receive}\cos\left(\delta_{receive} - \gamma\right) + V_{receive}\sin\left(\theta_{receive} - \gamma\right)\right]
\end{aligned}
\tag{4.30}
$$

Note that the sign on γ is reversed to reflect that power is flowing into the bus. Determining Thevenin equivalent resistance and reactance values requires two operating points. We choose the first to be the I and γ values on each line from the power flow solution. We choose the second operating point to be the bus voltages and angles at either end of each transmission line when the line is open. When the line is out, the sending end bus voltage and angle are the open line's open circuit values E_{send} and δ_{send} respectively. This provides data from the two needed operating points to compute a Thevenin equivalent R_{send} and X_{send} at the source bus. Similarly, the Thevenin equivalent $R_{receive}$ and $X_{receive}$ are computed at the receiving bus. Computed bus Thevenin R and X values that remain constant (or nearly constant) as system stress increases would be a clear indication that a Thevenin equivalent implementation may be possible.

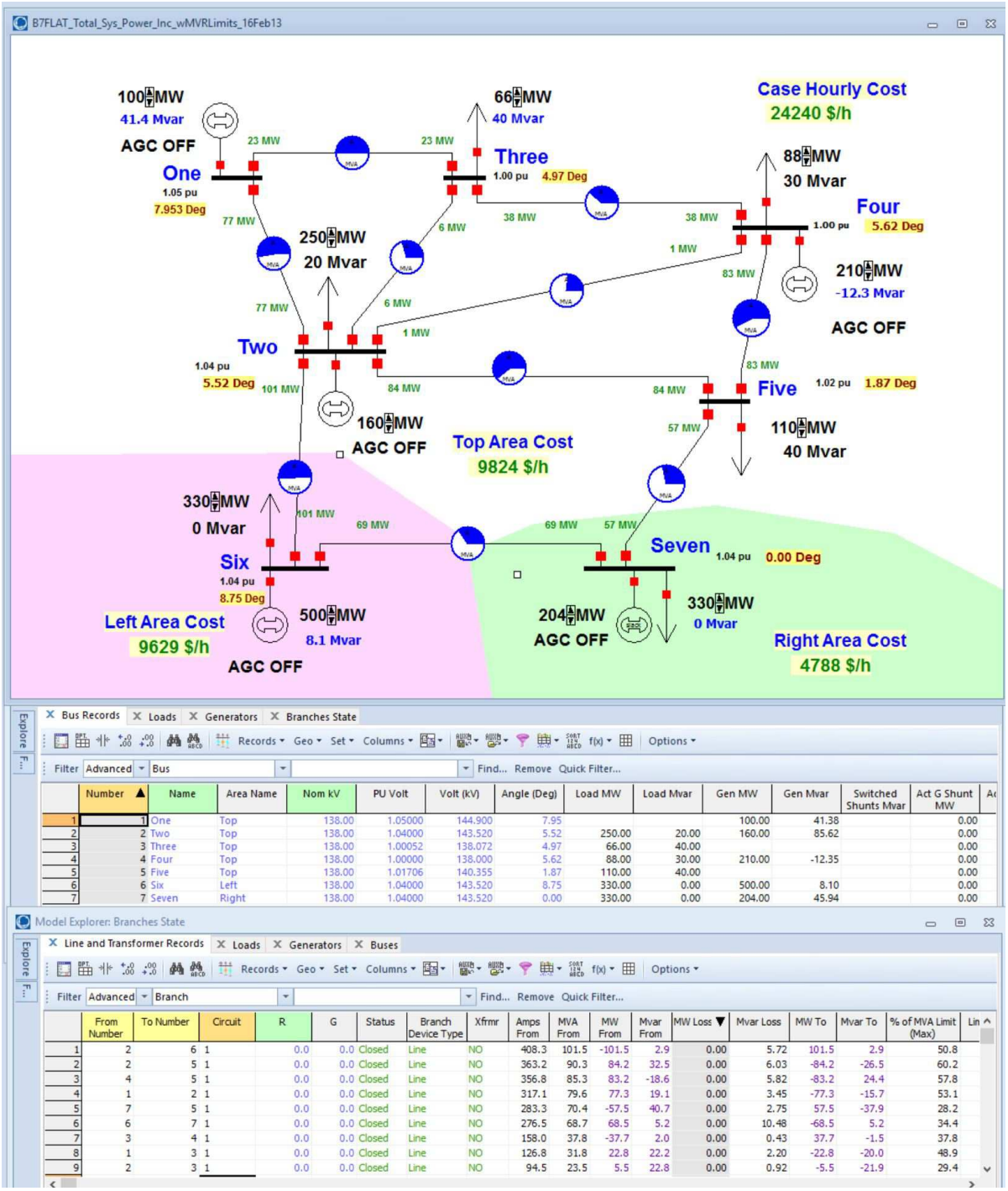

Number	Name	Area Name	Nom kV	PU Volt	Volt (kV)	Angle (Deg)	Load MW	Load Mvar	Gen MW	Gen Mvar	Switched Shunts Mvar	Act G Shunt MW
1	One	Top	138.00	1.05000	144.900	7.95			100.00	41.38		0.00
2	Two	Top	138.00	1.04000	143.520	5.52	250.00	20.00	160.00	85.62		0.00
3	Three	Top	138.00	1.00052	138.072	4.97	66.00	40.00				0.00
4	Four	Top	138.00	1.00000	138.000	5.62	88.00	30.00	210.00	-12.35		0.00
5	Five	Top	138.00	1.01706	140.355	1.87	110.00	40.00				0.00
6	Six	Left	138.00	1.04000	143.520	8.75	330.00	0.00	500.00	8.10		0.00
7	Seven	Right	138.00	1.04000	143.520	0.00	330.00	0.00	204.00	45.94		0.00

From Number	To Number	Circuit	R	G	Status	Branch Device Type	Xfrmr	Amps From	MVA From	MW From	Mvar From	MW Loss	Mvar Loss	MW To	Mvar To	% of MVA Limit (Max)
2	6	1	0.0	0.0	Closed	Line	NO	408.3	101.5	-101.5	2.9	0.00	5.72	101.5	2.9	50.8
2	5	1	0.0	0.0	Closed	Line	NO	363.2	90.3	84.2	32.5	0.00	6.03	-84.2	-26.5	60.2
4	5	1	0.0	0.0	Closed	Line	NO	356.8	85.3	83.2	-18.6	0.00	5.82	-83.2	24.4	57.8
1	2	1	0.0	0.0	Closed	Line	NO	317.1	79.6	77.3	19.1	0.00	3.45	-77.3	-15.7	53.1
7	5	1	0.0	0.0	Closed	Line	NO	283.3	70.4	-57.5	40.7	0.00	2.75	57.5	-37.9	28.2
6	7	1	0.0	0.0	Closed	Line	NO	276.5	68.7	68.5	5.2	0.00	10.48	-68.5	5.2	34.4
3	4	1	0.0	0.0	Closed	Line	NO	158.0	37.8	-37.7	2.0	0.00	0.43	37.7	-1.5	37.8
1	3	1	0.0	0.0	Closed	Line	NO	126.8	31.8	22.8	22.2	0.00	2.20	-22.8	-20.0	48.9
2	3	1	0.0	0.0	Closed	Line	NO	94.5	23.5	5.5	22.8	0.00	0.92	-5.5	-21.9	29.4

Figure 4.11: PowerWorld B7Flat test system diagram.

4.3.2 Power Flow Thevenin Equivalent Test Case

We have written a hybrid simulation using MATLAB in combination with PowerWorld via the Simulator Automation Server (SimAuto) component object module to generate a series of power flow solutions, and to record power flow solution data for subsequent analysis. The test system is PowerWorld Corporation's 7-bus system (B7Flat) depicted in Fig. 4.11; key simulation parameters are shown in PW model explorer screen shots. Sample simulation results are shown in Fig. 4.12. The simulation uses purely reactive transmission lines and does not include charging admittances. The lower figure portion shows the progressively increasing power generation and demand set points that increase until the power flow solution does not converge (i.e. a stability limit is violated). In this case, the power generated and used increases exponentially as the set point number increases; the increased power generated and demanded stresses the model power system in a way not unlike inflating a balloon until it ruptures.

At each power set point, the MATLAB program calls PowerWorld to produce a power flow solution. Each data point on the power set line represents power demand, power generation, or the difference between the bus angles in the set's power flow solution. Note that the number of successful power flow solutions for each line being removed from service varies. Transmission line 2–6 has the fewest of solutions and, as expected, also shows the greatest AnglxSys.

Thevenin equivalent resistances and reactances were computed per the process described above using Eqs. (4.29) and (4.30). The computed Thevenin equivalent values are shown in Fig. 4.13. The results show encouraging evidence of linear behavior. However, there is also non-linear behavior that may limit the method's efficacy.

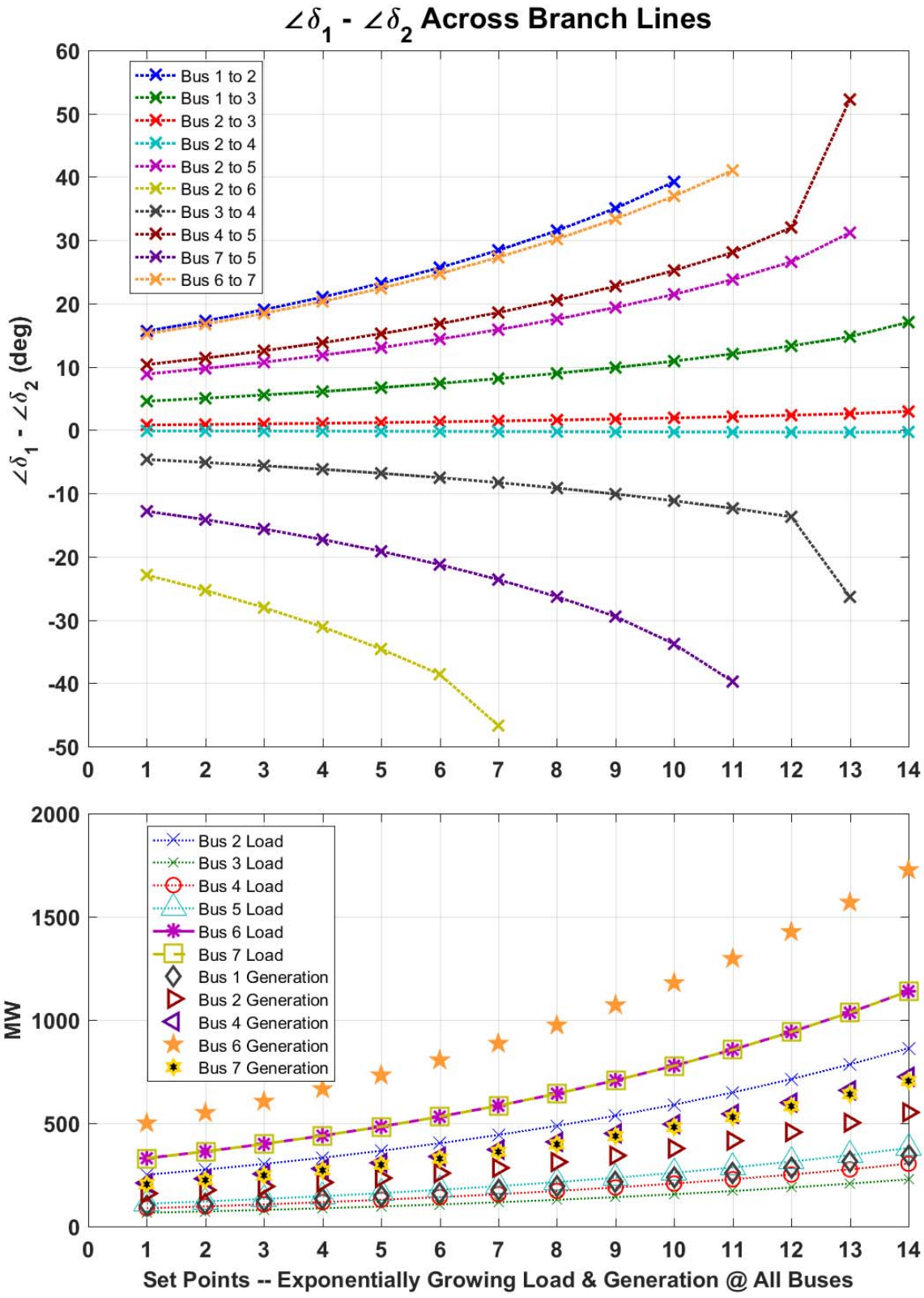

Figure 4.12: Simulated bus angle differences across open transmission lines.

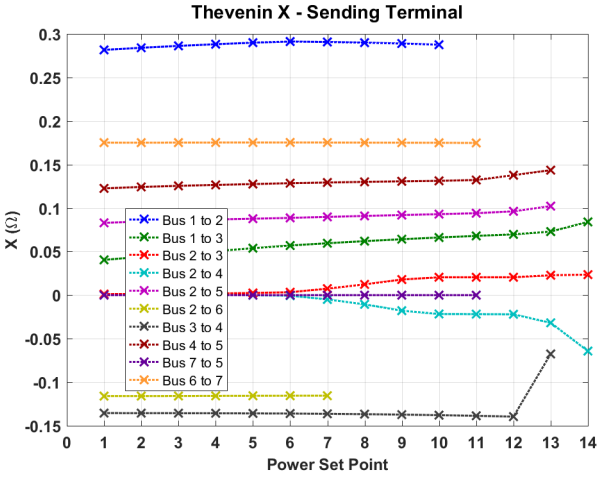

(a) Sending bus Thevenin reactance.

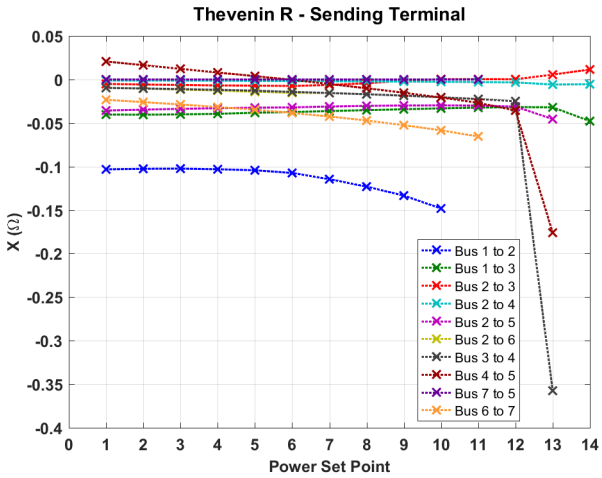

(b) Sending bus Thevenin resistance.

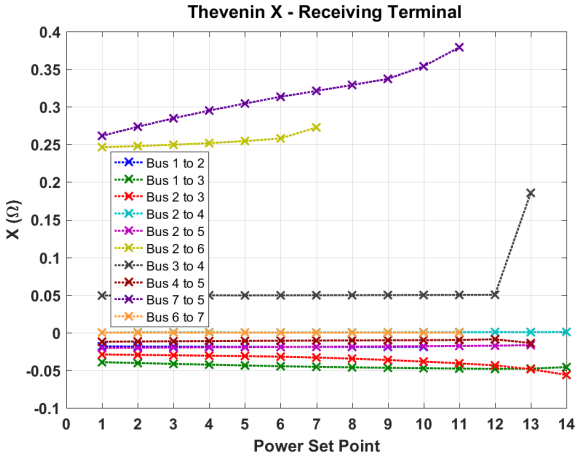

(c) Receiving bus Thevenin reactance.

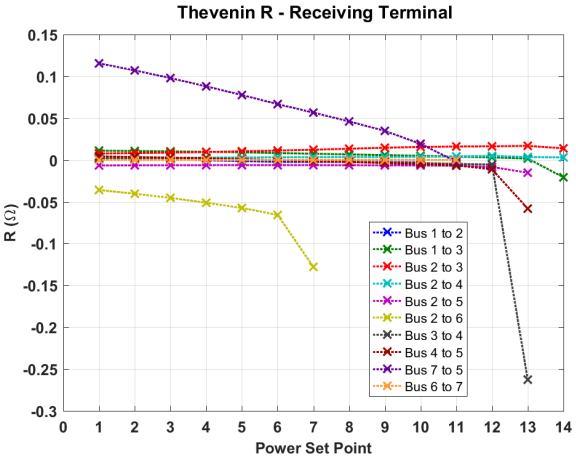

(d) Receiving bus Thevenin resistance.

Figure 4.13: Thevenin equivalent values for each transmission line computed at power set points.

4.3.3 Applying Monte Carlo Methods

The drawback to the Thevenin equivalent computed from power flow solutions is the impracticality of applying the technique in the field environment, i.e. opening a transmission line to obtain the "open circuit" measurement. An alternative is to use Monte Carlo techniques to determine Thevenin equivalent parameters from many measurements taken in the normal operating range of the two buses connected by the transmission line. Given the linear

behavior observed in the PF Thevenin equivalent, the approach is plausible. If acceptable Thevenin equivalent impedance can be computed, then the power system stability could be monitored by flagging variations from the established parameters.

We extended the PowerWorld simulation to create random variations in load and generation at the power set points. The objective is to gain insight into the impact of random, banded load and generation variations about the set points. The variations generated resemble the random values about the original set points as shown at bus 2 in Fig. 4.14a; in this example, four additional load and generation set points were randomly generated in a band ± 5 percent about the original set points. The Thevenin equivalent computation algorithm applied to these input data sets to compute Thevenin resistance and reactance at the power sending terminal produced the values shown in Fig. 4.14b.

At lower power set points, the effect upon the computed Thevenin equivalent reactance is both stable and linear as the power increases. Beyond set point 6, the computed reactance for the transmission lines connecting buses 2 and 4 and buses 2 and 3 exhibits non-linear sensitivity to ± 5 percent random variations. This indicates a bound on the amount that load and generation can be increased while retaining confidence that the computed values are useful for computing a Thevenin equivalent.

Significantly, the reactance values computed with the randomly generated load and generation variations for all lines below set point 7 clearly show linear and nearly constant behavior. This linear behavior is important – it points to the possibility that Thevenin equivalent component values could be generated using Monte Carlo-like techniques using synchrophasor data to establish a useful Thevenin equivalent circuit. The resulting Thevenin equivalent used with streaming synchrophasor data could then be a useful measure of phase angle differences across the transmission line – and importantly an indicator when the angle difference across the line is moving toward system security policy limits. Across the system the Thevenin equivalent models could also point to transmission lines that are more likely to threaten system stability.

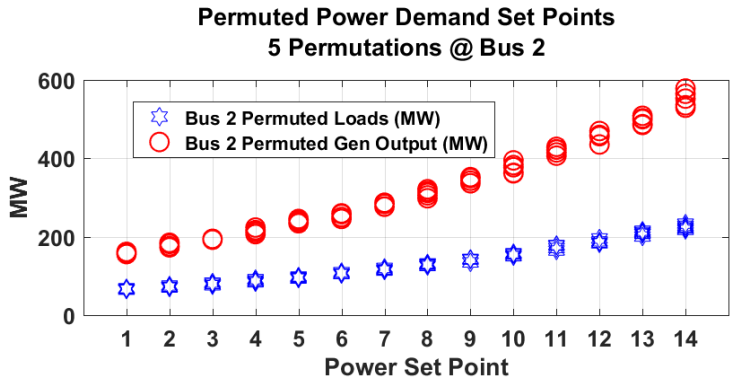

(a) Permuted power set points.

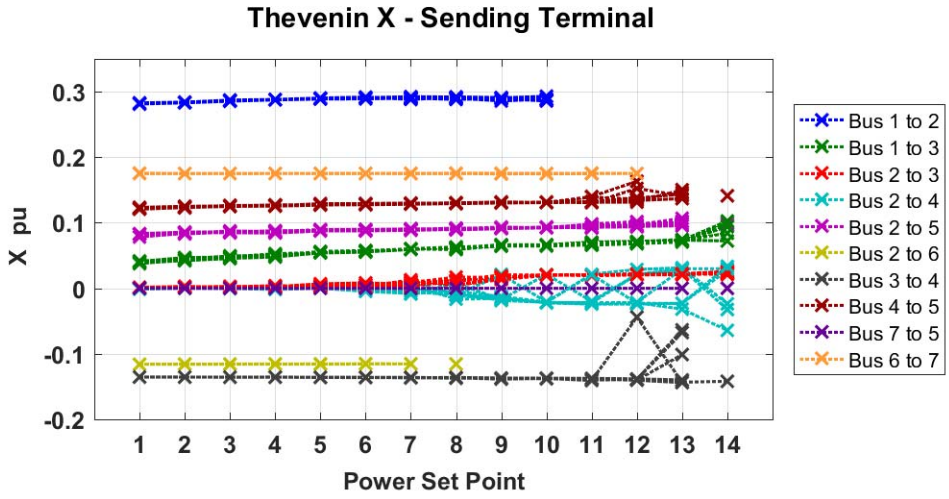

(b) Thevenin X computations from permuted power set values.

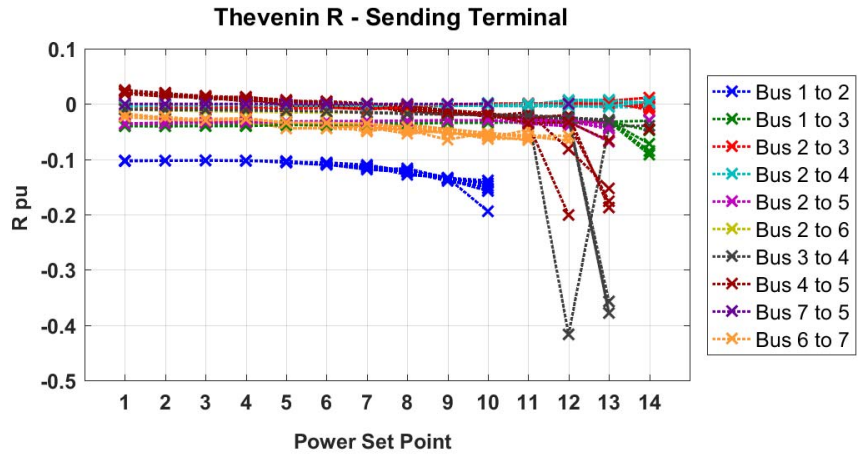

(c) Thevenin R computations for permuted power set values.

Figure 4.14: Monte Carlo approach to computing Thevenin equivalents to randomly generated load and generation set points in a band bounded by a $\pm.05$ factor about the original set points.

This line of investigation offers hope that Monte Carlo-like techniques may be useful for developing a Thevenin equivalent model for assessing the angle difference between buses connected by transmission lines. Such a Thevenin equivalent could be valuable because it would be computed in the field using synchrophasor data – independent of load-flow and other control room-based measures of system security. Thus, this line of investigation merits continued investigation.

Chapter 5

Synchrophasor Data from Machine Transient Response

In both real-time system control and after-the-fact dynamic behavior analysis, there are a number of issues to be investigated regarding the utility of synchrophasor data produced by PMUs. Inherent to its purpose and design, the PMU computes a phasor value (including both magnitude and phase) at the system's nominal frequency (60 Hz in the U.S. and Canada) over a sample data window that fully characterizes the sinusoidal steady-state waveform. However, a disturbance causing a dynamic response is likely to be poorly characterized by a phasor; in essence, the phasor represents filtered data. This line of investigation seeks to understand from a "field" perspective the information that can be extracted from synchrophasor data streams produced during a synchronous generator's transient response to a disturbance event. Of particular interest is whether useful synchronous generator transient behaviors can be extracted from synchrophasor data.

The approach was twofold. First, a purpose-written MATLAB simulation was used to generate a baseline dynamic response in the across the highlighted timescales illustrated in Fig. 5.1. The MATLAB simulation was entirely our own work leveraging existing MATLAB differential algebraic equation (DAE) solution tools; as such, we had complete control and knowledge of the code's inner workings. Second, we used a Real-Time Digital Simulator (RTDS) to produce real-time, analog generator terminal waveforms that were sampled by the PMU built into Schweitzer Engineering Laboratory's SEL-421 Protection, Automation, and Control System. This test design enabled "field" measurements to be collected in a controlled laboratory environment with full knowledge of test system behavior.

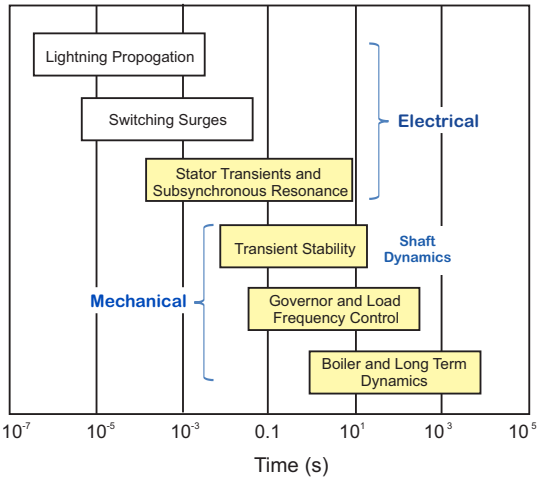

Figure 5.1: The synchronous machine dynamic phenomena modeled in this investigation are highlighted. Adapted from Fig. 1.2 in [43].

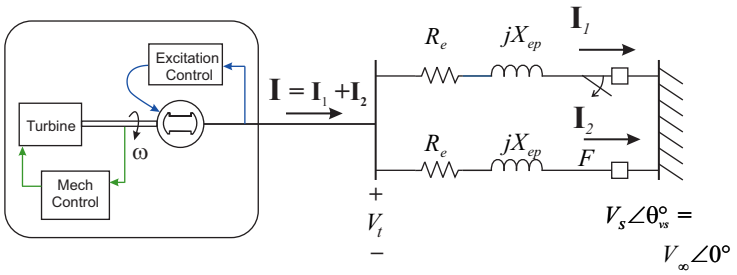

Figure 5.2: The test system is a synchronous generator connected to an infinite bus by identical parallel transmission lines. The disturbance event producing the simulated system dynamic response occurs when TL-1 is opened.

The test system was a synchronous generator connected by a pair of identical transmission lines to an infinite bus as shown in Fig. 5.2 and implementing the system model detailed in Chapter 2. The disturbance event occurs when transmission line one (TL-1) is opened.

The RTDS is a purpose-built computer designed very specifically to simulate electromagnetic transients in real-time. The RTDS equipment design provides the capability to make low-voltage ($\sim$ 5 V) analog output signals available for interfacing with external equipment. The RTDS receives and integrates a live GPS timing signal using the SEL-2407 Satellite Synchronized Clock into the simulation. Thus, the RTDS-based simulation is as close to taking "field measurements" as possible short of connecting the SEL hardware to a live power line.

Using the MATLAB and RTDS in parallel provided the ability to cross-check the MATLAB Multi-Time-Scale model (MTSM-14) and 11th-order reduced system model (RedSysMdl-11) simulation results with RTDS results. A down side to the RTDS simulator in this application is that its component modules are in many respects "black boxes", i.e. internal component processes are opaque to the user. Considerable effort was undertaken to harmonize simulation component models. RTDS component models were selected that implemented the test system model described in Chapter 2. To the fullest extent possible, the MATLAB simulation emulated the selected RTDS component models. The ultimate objective was for two simulations to produce convergent results, enabling an apples to apples comparison of the results.

5.1 Preliminaries

First, the data produced by the PMU when the system is not operating at or near the fundamental frequency is not a "phasor"; rather, it is a number generated by an algorithm set to process measurements at the system's operating frequency. That being said, the data produced under dynamic conditions may still be useful if properly interpreted. Second, the sampled voltage and current values are altered from the point of measurement by bandwidth limited CT/PT sensors, analog anti-aliasing low-pass filters, limited bandwidth sampling rates, and further digital signal processing that produces phasors. Undoubtedly, this signal processing chain "filters" useful information occurring at other than the fundamental frequency. This is particularly important during events having high frequency content. The practical question to be answered is what transient information can be discerned from synchrophasor data.

Continuous 3-phase current is represented:

$$\begin{aligned} I_a &= \sqrt{2}\sqrt{I_d^2 + I_q^2}\cos\left(\omega_s t + \delta + (\tan^{-1}\tfrac{I_q}{I_d}) - \tfrac{\pi}{2}\right) \\ I_b &= \sqrt{2}\sqrt{I_d^2 + I_q^2}\cos\left(\omega_s t + \delta + (\tan^{-1}\tfrac{I_q}{I_d}) - \tfrac{\pi}{2} - \tfrac{2\pi}{3}\right) \\ I_c &= \sqrt{2}\sqrt{I_d^2 + I_q^2}\cos\left(\omega_s t + \delta + (\tan^{-1}\tfrac{I_q}{I_d}) - \tfrac{\pi}{2} + \tfrac{2\pi}{3}\right) \end{aligned} \tag{5.1}$$

Three-phase voltage data is represented by similar expressions.

The PMU samples stepped-down current and voltage signals via instrument transformers. Following anti-aliasing filtering and digitization, digital signal processing produces voltage and current phasor data. Applying the discrete Fourier transformation to the sampled current data produces the discrete "a" phase and positive sequence current representations respectively:

$$\begin{aligned} \bar{I}_{\underset{DFT}{a}} &= \frac{\sqrt{2}}{N}\sum_{k=1}^{N} I_{ak} e^{-jk\frac{2\pi}{N}} \\ \bar{I}_{\underset{DFT}{POS}} &= \frac{1}{3}\left(\bar{I}_{\underset{DFT}{a}} + \bar{I}_{\underset{DFT}{b}} e^{j\frac{2\pi}{3}} + \bar{I}_{\underset{DFT}{c}} e^{-j\frac{2\pi}{3}}\right) \end{aligned} \tag{5.2}$$

The d-q reference frame current and voltage phasors are represented by:

$$\begin{aligned} \bar{I}_{DQ} = \ (I_D + jI_Q) \ &= \ (I_d + jI_q)\, e^{j(\delta - \pi/2)} \\ \bar{V}_{DQ} = (V_D + jV_Q) \ &= (V_d + jV_q)\, e^{j(\delta - \pi/2)} \end{aligned} \tag{5.3}$$

Conceptually understanding differences between simulation-based phasors and measurement-based phasors is fundamentally important to interpreting synchrophasor data produced during transitions between equilibrium states.

5.2 MATLAB Simulation and Results

The purpose-written MATLAB simulation program is built around the ode15s ordinary differential equation (ODE) solver, which is well-suited for systems of stiff differential algebraic equations (DAEs). The ode15s solver is a quasi-constant step, variable order differential

equation integrator. The essential structure of the ode15s solver function call is shown in Fig. 5.3.

Figure 5.3: MATLAB ode15s solver function call example.

The "options" odeset is used to set up the solver. Two important "options" are pictured: "Mass" which is the matrix defining the left-hand side of the DAE equation set, and "Events" which calls a conditional function that interrupts the solver if specific conditions are satisfied. The right-hand side of the DAE equation set is passed to the solver via function name in the first position (in this example "@Full_Model_v3").

The ode15s ODE solver's output is a structured array. An example is shown in Fig. 5.4. The simulation code is considerably more complex, including multiple calls to ode15s as the simulation moves from equilibrium, through each phase on TL-1 being opened at current zero crossing until a new equilibrium state is reached. The simulation code itself is complex and extensive, consisting of 2000+ lines of code contained in up to 30 function calls executing modular code.

The MATLAB DAE structural analysis (DAESA) tool also proved to be quite valuable. The DAESA function call includes data structure similar to the "@Full_Model_v3" function call in the ode15s solver input. The DAESA tool determines the structural index, degrees of freedom, constraints, and variables that must be initialized, and it suggests a solution scheme; an example is shown in Fig. 5.5.

The MATLAB simulation results follow. The terminal current and voltage responses are shown first because these are the waveforms that the PMU samples. The most dramatic simulation result is the I_{dqo} result (Fig. 5.6) previously presented in Chapter 2. Of note is that MTSM-14 I_{dq} curve envelopes are defined by a nominally 60 Hz oscillation. This observation tracks nicely with the expected integral manifold approach variable reduction outcome eliminating the stator flux linkage state variables, which would have a 60 Hz component. Recalling Fig. 2.5, care must be taken not to misinterpret (or confuse) the seeming 60 Hz oscillation in the *dqo* frame with the *abc* frame's nominal 60 Hz system frequency. The oscillation observed in the *dqo* frame exists as a short-lived transient. Recall that any waveform moving synchronously with the rotor has a constant value in the *dqo* reference frame, and as expected I_{dq} settles to constant values several seconds after TL-1 opens.

```
[Full_Mdl_Soln] = ode15s(@Full_Model_v3, options, time_span, Init_Cond )
```

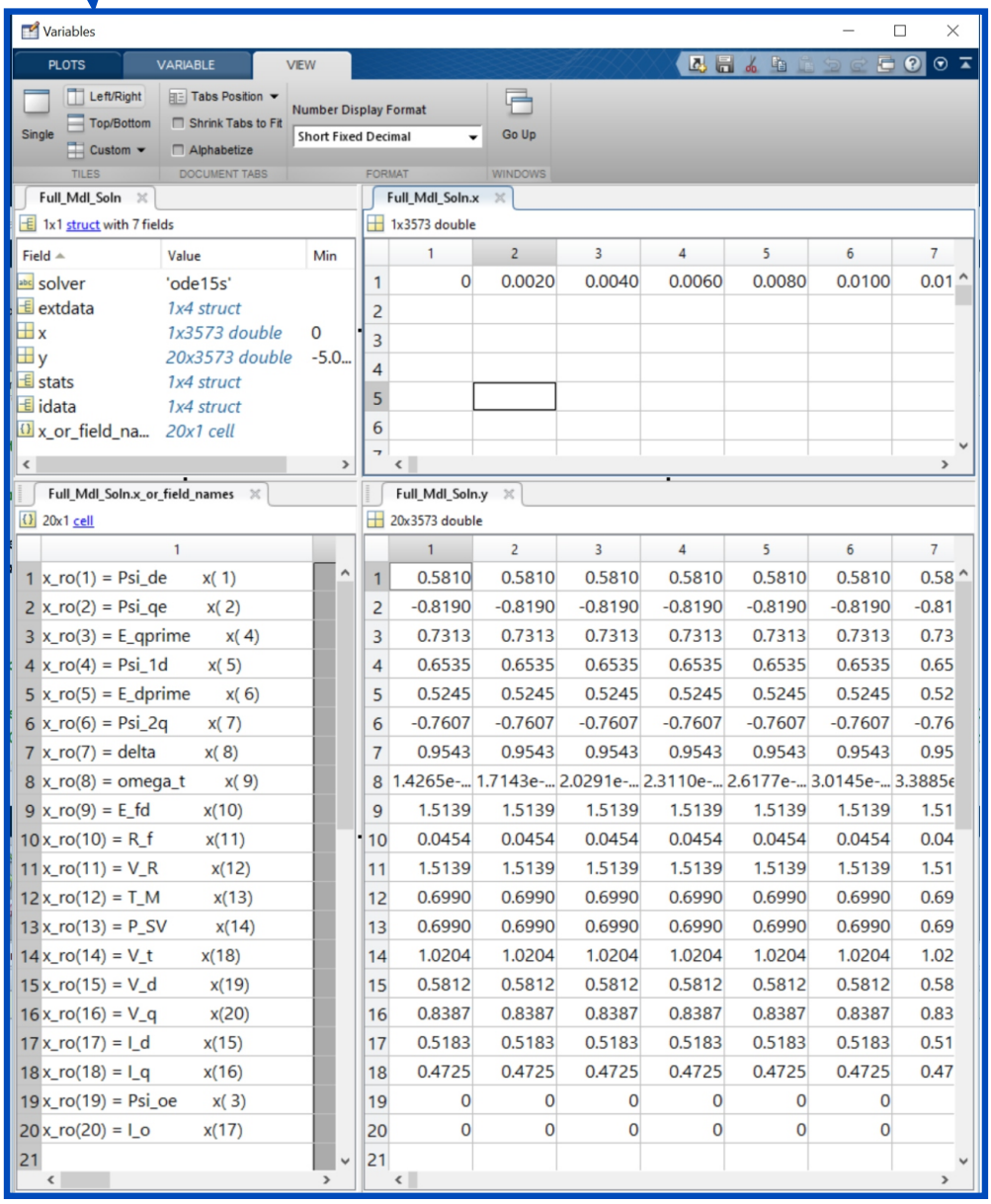

Figure 5.4: MATLAB ode15s structured array output example. The tab "Full_Mdl_Soln" shows the sub-array variable names, data types, and sizes. The tab "Full_Mdl_Soln.x" displays the time vector. The tab "Full_Mdl_Soln.x_or_field_names" displays the string array labeling each field. The tab "Full_Mdl_Soln.y" displays the integrated state variable at each time; the corresponding time is above; and the state variable name is to the left.

The terminal voltages, V_t, V_d, and V_q (Fig. 5.7), show markedly different transient response than the terminal currents. The transient response in the 0.05 s following the event is much less dramatic. The MTSM-14 and RedSysMdl-11 solutions track so closely during

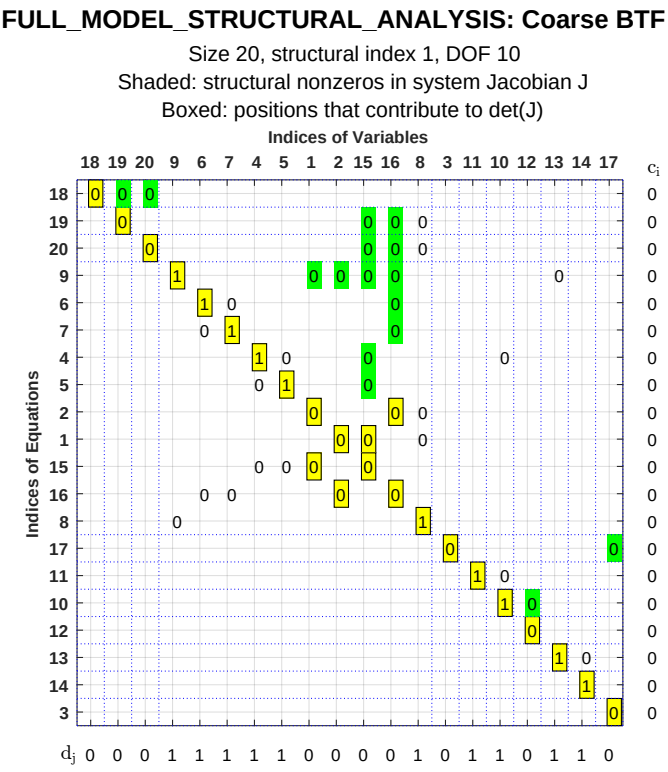

Figure 5.5: Sample MATLAB DAE structural analysis (DAESA) tool output. The row of numbers above the graph is the suggested new variable order; the column of numbers to the left is the suggested new equation order. The tool is useful for verifying that the DAE system is properly structured and is helpful in identifying errors in complex equation systems.

the dynamic response that they are nearly indistinguishable; thus the reduced order model is a very good representation of the voltage response. The voltages settle to new equilibrium values in about 6 s.

The mechanical system state variables are shown in Fig. 5.8. As expected, P_{SV} and T_M track very closely, with P_{SV} leading T_M slightly as would be expected because steam valve pressure delivers power to the shaft based upon governor feedback controls. The difference between T_M in the MTSM-14 and RedSysMdl-11 simulation is insignificant.

The excitation system state variables are shown in Fig. 5.9. The important feature to note in variables E_{fd}, V_R, and R_f is that RedSysMdl-11 produces results closely matching the full system model. The one minor but notable difference is that the RedSysMdl-11 simulation clips the pilot exciter voltage, V_R, in the 0.05 s following the disturbance.

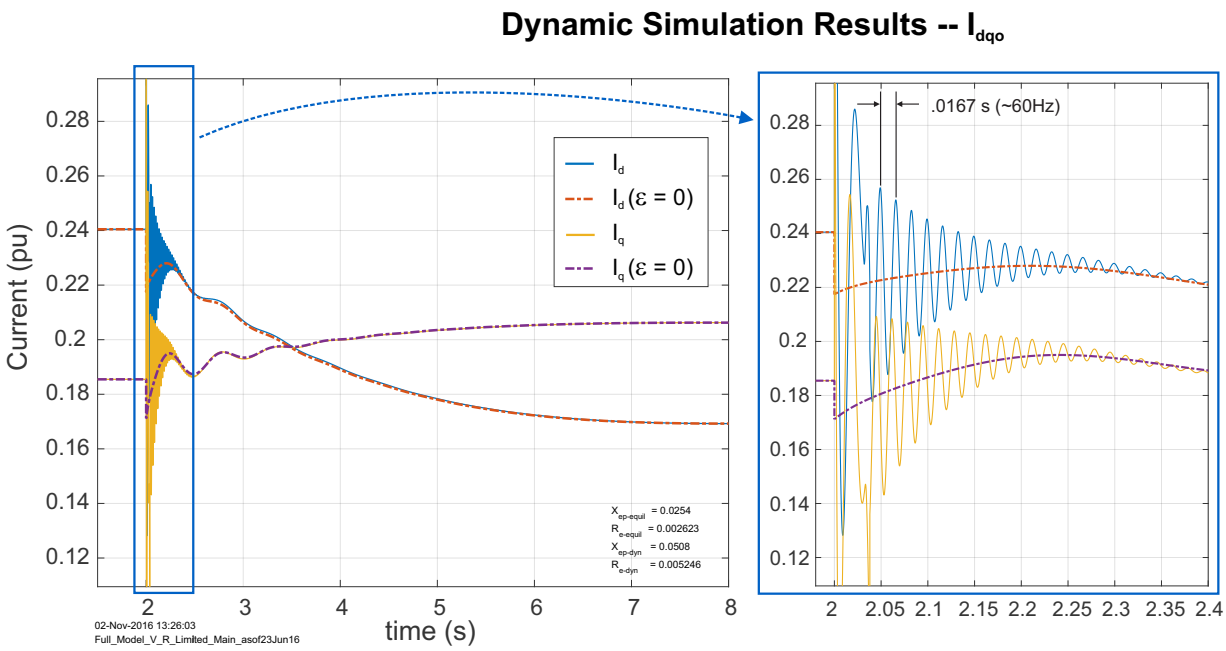

Figure 5.6: Simulation results – $\mathbf{I}_{dqo}$.

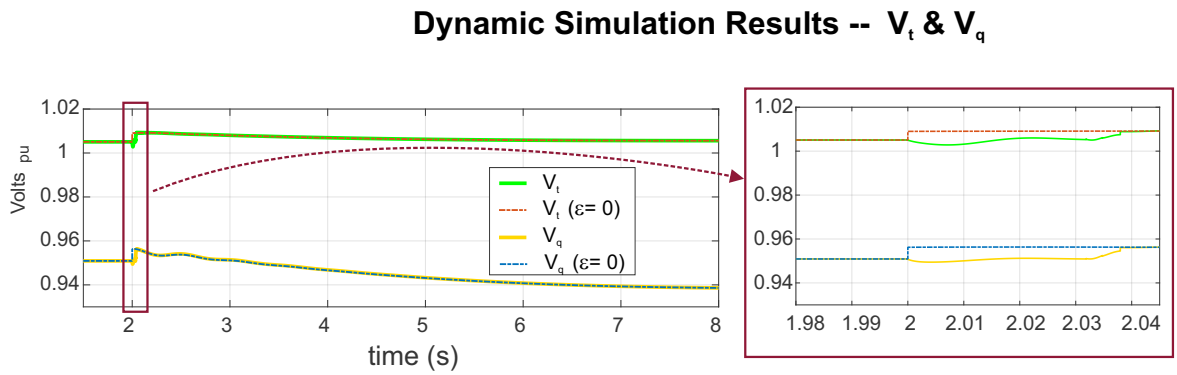

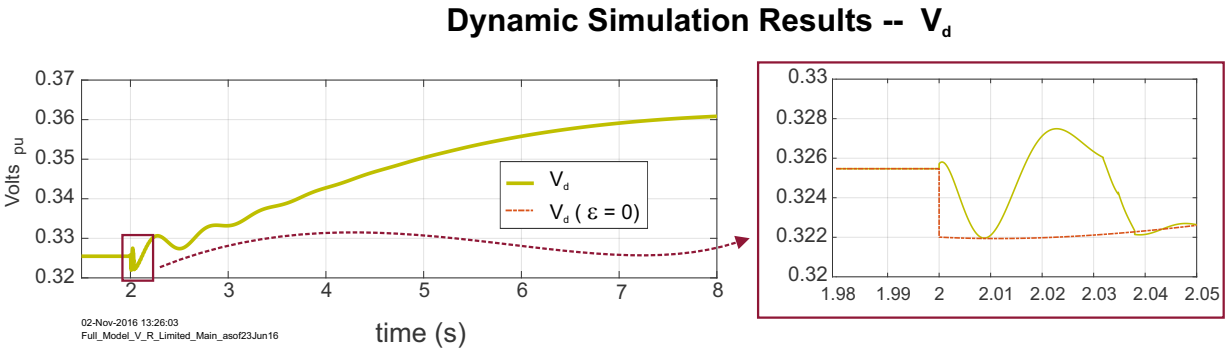

Figure 5.7: Simulation results – $\mathbf{V}_{dqo}$.

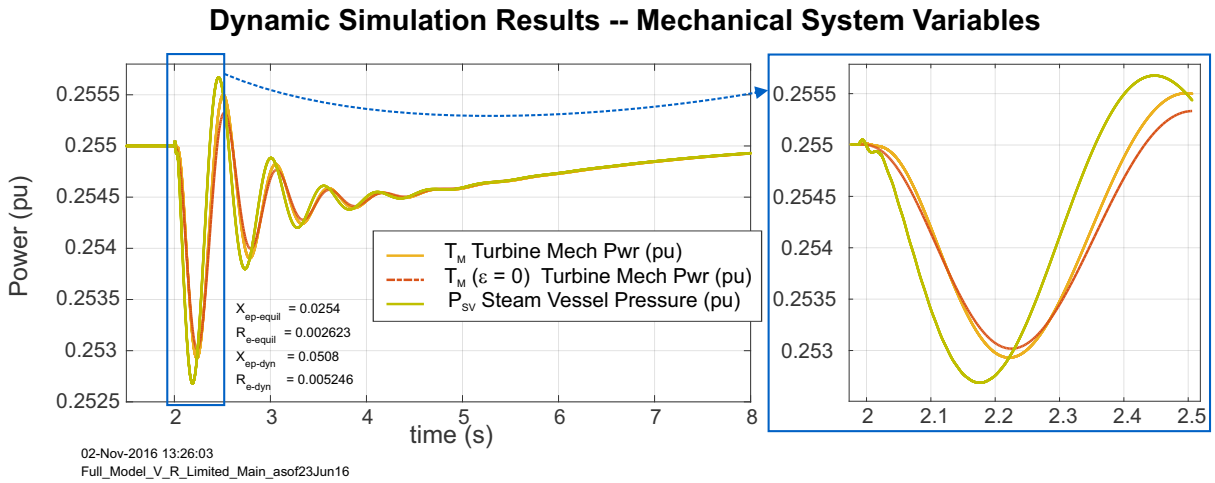

Figure 5.8: Simulation results – mechanical system variables.

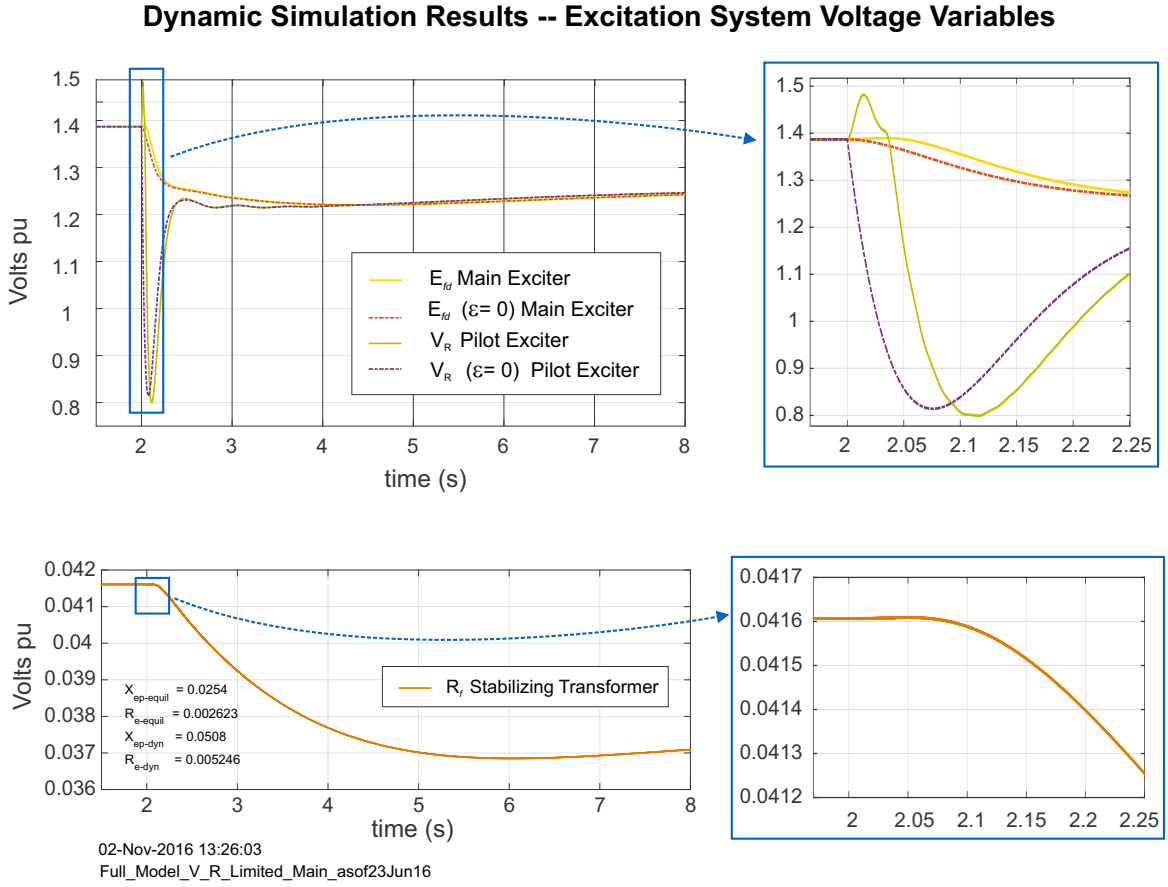

Figure 5.9: Simulation results – excitation system variables.

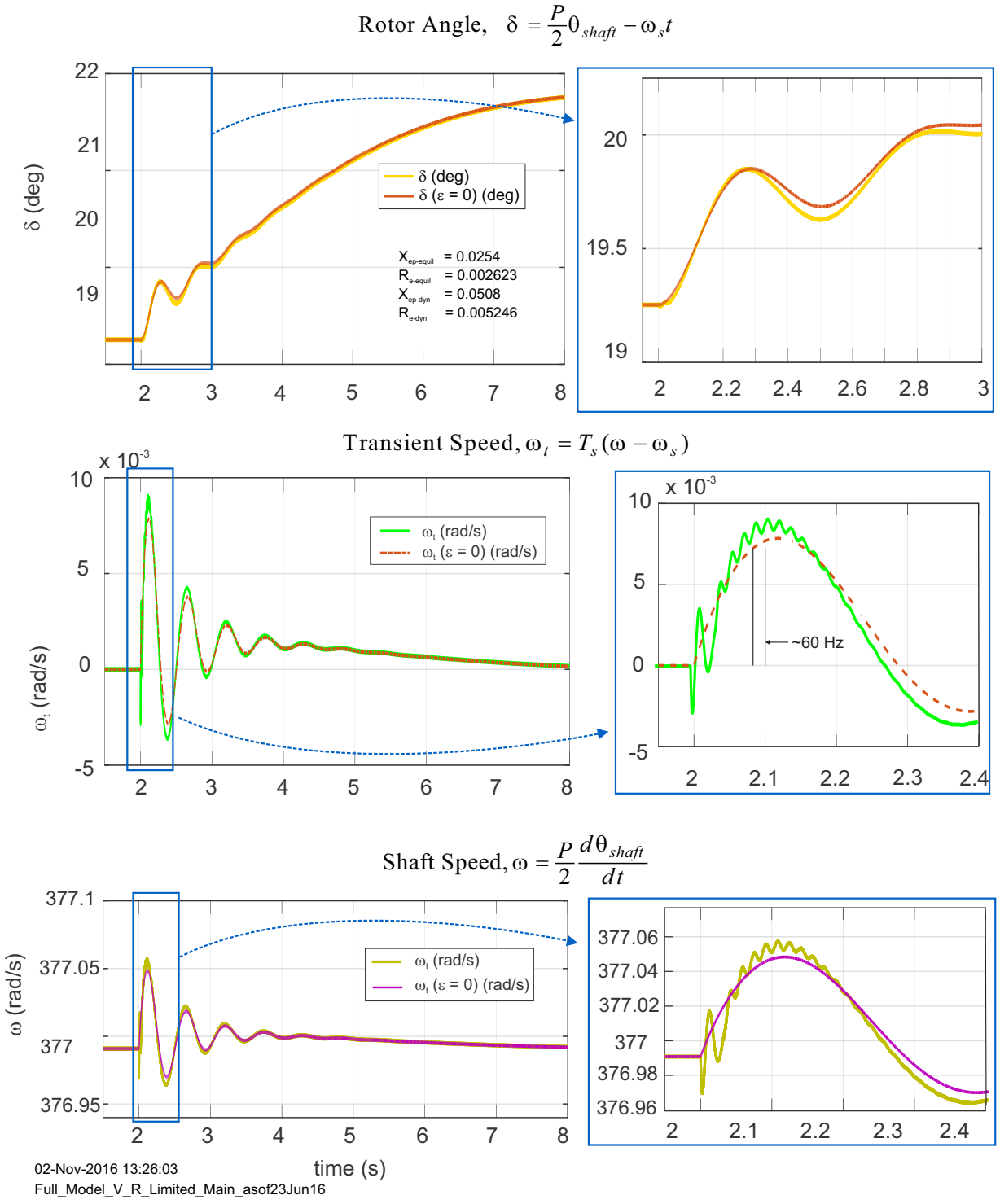

Figure 5.10: Simulation results – speed variables.

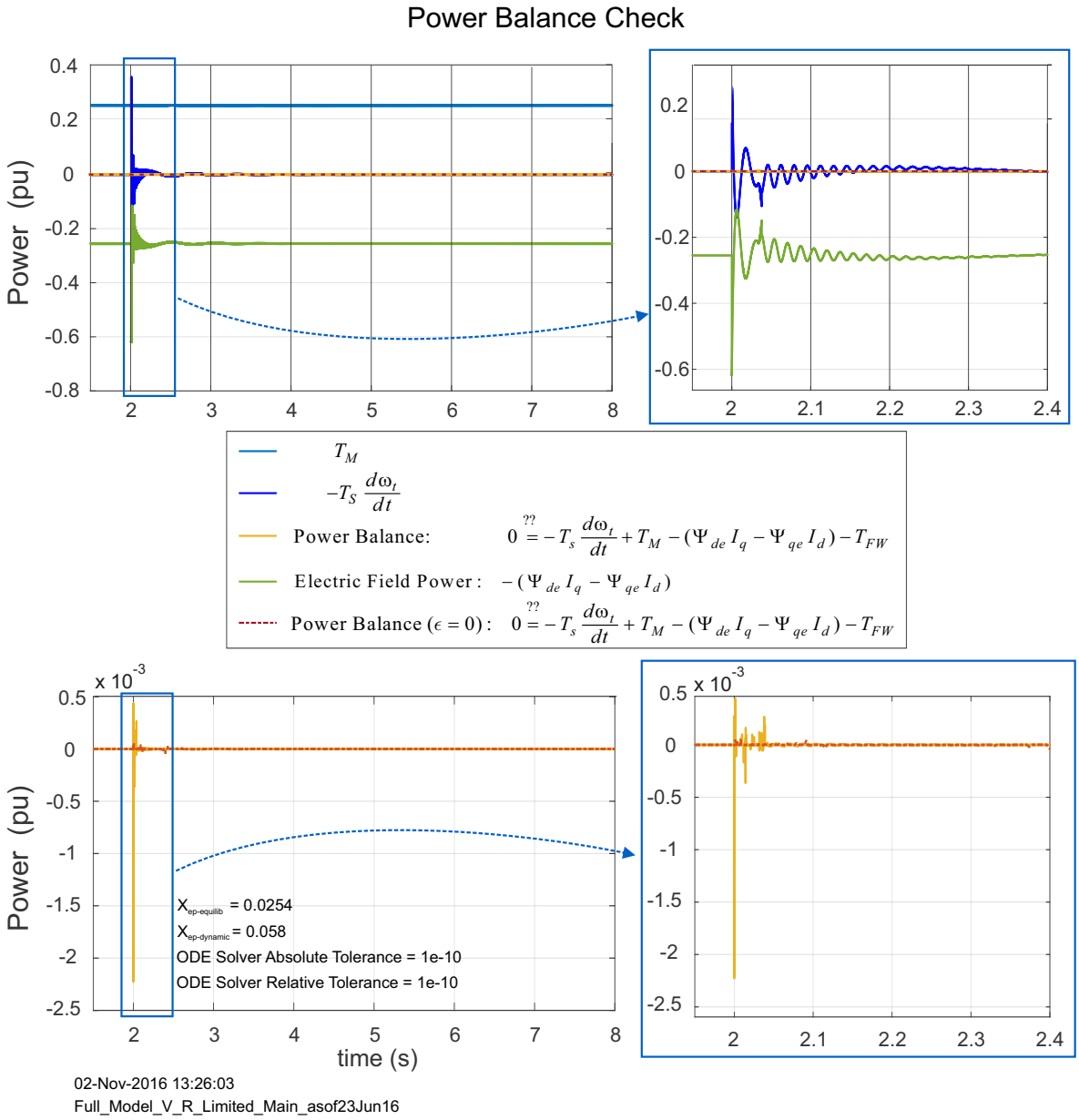

Figure 5.11: Simulation results – consistency check.

The speed-related state variables are shown in Fig. 5.10. The rotor angle, δ, transient response is essentially indistinguishable between the MTSM-14 and RedSysMdl-11 simulations. Similarly, ω and ω_t are nearly indistinguishable between the MTSM-14 and RedSysMdl-11 except in the first 0.25 s following the disturbance. In that 0.25 s in the MTSM-14 simulation results, ω and ω_t show an oscillation about the RedSysMdl-11 simulation results. The oscillation is $\sim$ 60 Hz and closely resembles a similar feature in the MTSM-14 I_{dq} results. Worth

noting, however, is that the magnitude peak change in ω during the transient response is very small (0.05 rad/s change on the 377 rad/s steady-state speed). Also worth noting are similarities between ω and ω_t; ω_t is normalized to 0.0 and has magnitude $\sim 10^{-3}$, and ω has its steady state value about 377 rad/s.

To verify that the MTSM-14 and RedSysMdl-11 simulations were correctly coded, Eq. (5.50) was checked for internal consistency and was found to be consistent (Fig. 5.11). The greatest mismatch was $\sim 10^{-3}$ immediately after disturbance and at better than $\sim 10^{-4}$ 0.1 s later.

5.3 RTDS Simulation Description

The Real-Time Digital Simulator (RTDS) is a digital system which models the power system based on an Electromagnetic Transients Program (EMTP) simulation approach. The RTDS can simulate any user-defined electrical system with complex electrical component models, such as transmission lines, generators and transformers. With the RTDS real-time simulator, commercial power equipment can be integrated into a closed-loop system for testing and characterization mimicking field conditions. We worked closely with the Information Trust Institute's Electric Grid Security Testbed to implement our simulation on their RTDS and SEL equipment pictured in Figs. 5.12 and 5.13 respectively.

The simulation was developed graphically through the RTDS Draft program and is shown in Fig. 5.14.

The RTDS synchronous machine component model MACV31 was used to implement the generator. The model is detailed in Fig. 5.15.

The RTDS component library did not have an appropriate native excitation system component. Using RTDS sub-component modeling tools, we implemented the excitation system detailed in Chapter 2. The RTDS simulation excitation system is detailed in Fig. 5.16.

Figure 5.12: RTDS equipment rack.

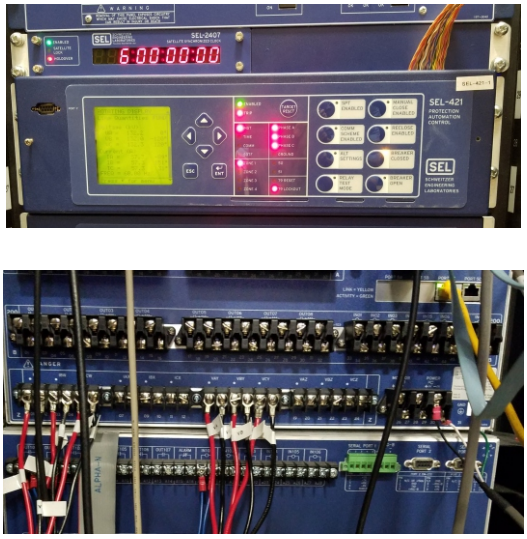

Figure 5.13: SEL-421 Protection, Automation, and Control System and SEL-2407, Satellite Synchronized Clock (front and back panels).

The RTDS component library did not have an appropriate mechanical control system component. Using RTDS sub-component modeling tools, we implemented the mechanical control system detailed in Chapter 2. The RTDS simulation mechanical control system is detailed in Fig. 5.17.

The transmission lines TL-1 and TL-2 were implemented using the RTDS component model TLINE. The model is detailed in Fig. 5.18.

The RTDS simulation is executed and controlled using the Runtime program. The simulation control panel and meters are shown in the boxed red area in Fig. 5.19. The simulation parameters P_C (Eq. 5.64 of Fig. 5.17b.) and V_{ref} (Eq. 5.56 of Fig. 5.16b.) are controlled via the slide switches in the center. The simulation execution occurs in multiple steps. The simulation starts in the "lock" mode to initialize the system; the lock mode is controlled via the toggle switch in the lower left-hand corner. When the meters have stabilized, the simulation can be toggled from the "lock" to the "free mode". When the meters have stabilized and the power meters are showing 140 MW (the transmission line surge impedance load),

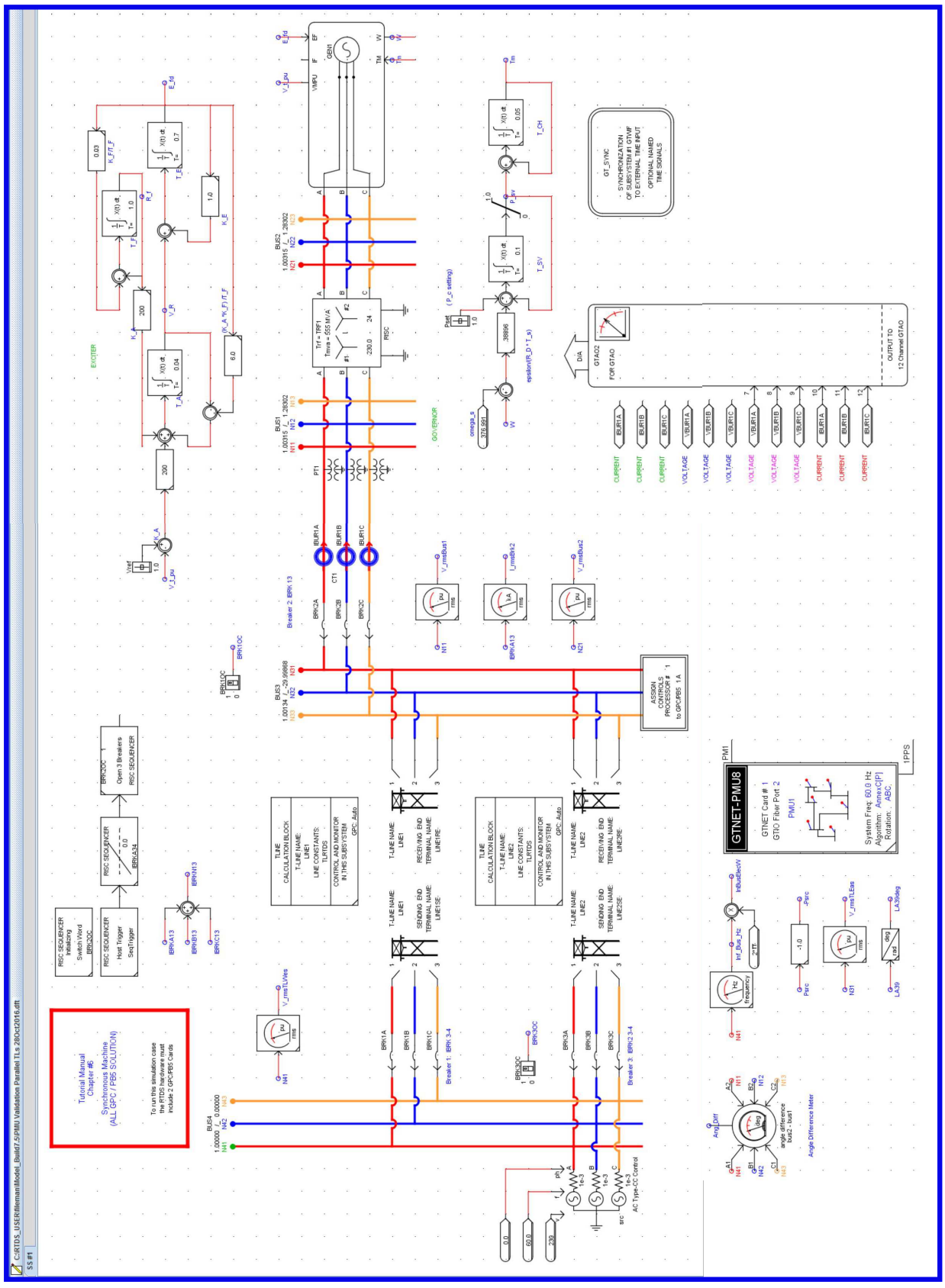

Figure 5.14: RTDS Draft 4.006.2 program simulation schematic.

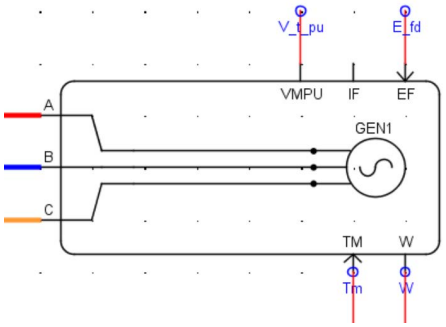

(a) Component model.

$$\varepsilon \frac{d\psi_d}{dt} = R_s\left(I_{d1}+I_{d2}\right) + \left(1+\frac{\varepsilon}{T_s}\omega_t\right)\psi_q + V_d \tag{5.42.2}$$

$$\varepsilon \frac{d\psi_q}{dt} = R_s\left(I_{q1}+I_{q2}\right) - \left(1+\frac{\varepsilon}{T_s}\omega_t\right)\psi_d + V_q \tag{5.43.2}$$

$$\varepsilon \frac{d\psi_o}{dt} = R_s\left(I_{o1}+I_{o2}\right) + V_o \tag{5.44.2}$$

(b) Stator winding equations.

$$T'_{do}\frac{dE'_q}{dt} = -E'_q - (X_d - X'_d)\cdot\left[\left(I_{d1}+I_{d2}\right) - \frac{X'_d - X''_d}{\left(X'_d - X_{\ell s}\right)^2}\left(\psi_{1d} + (X'_d - X_{\ell s})(I_{d1}+I_{d2}) - E'_q\right)\right] + E_{fd}, \tag{5.45.1}$$

$$T''_{do}\frac{d\psi_{1d}}{dt} = -\psi_{1d} + E'_q - (X'_d - X_{\ell s})(I_{d1}+I_{d2}) \tag{5.46.1}$$

$$T'_{qo}\frac{dE'_d}{dt} = -E'_d + (X_q - X'_q)\cdot\left[\left(I_{q1}+I_{q2}\right) - \frac{X'_q - X''_q}{\left(X'_q - X_{\ell s}\right)^2}\left(\psi_{2q} + (X'_q - X_{\ell s})(I_{q1}+I_{q2}) + E'_d\right)\right], \tag{5.47.1}$$

$$T''_{qo}\frac{d\psi_{2q}}{dt} = -\psi_{2q} - E'_d - (X'_q - X_{\ell s})(I_{q1}+I_{q2}) \tag{5.48.1}$$

(c) Rotor winding equations.

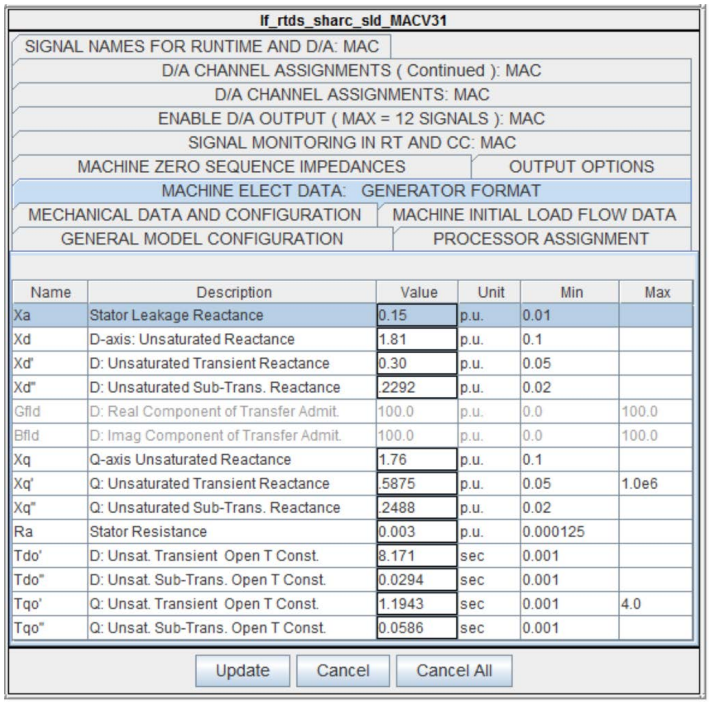

(d) Configuration menu.

Figure 5.15: RTDS Draft 4.006.2 generator component model MACV31 implementing Figs. 2.7 and 2.8.

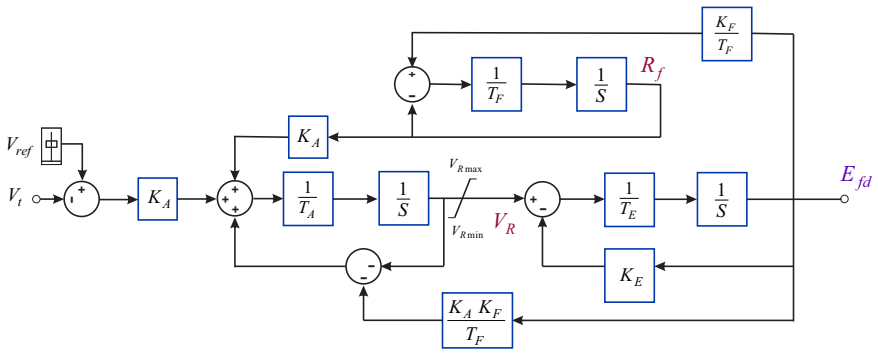

(a) Excitation system schematic diagram.

(5.54) $$T_E \frac{dE_{fd}}{dt} = -\left(K_E + S_E\left(E_{fd}\right)\right)E_{fd} + V_R$$ **Main Exciter**

(5.55) $$T_F \frac{dR_f}{dt} = -R_f + \frac{K_F}{T_F} E_{fd}$$ **Stabilizing Transformer**

(5.56) $$T_A \frac{dV_R}{dt} = -V_R + K_A R_f - \frac{K_A K_F}{T_F} E_{fd} + K_A\left(V_{ref} - V_t\right)$$ **Pilot Exciter**

(5.57) $$V_R^{\min} \le V_R \le V_R^{\max}$$ $-5.0 \le V_R \le 5.0$

(b) Excitation system equations.

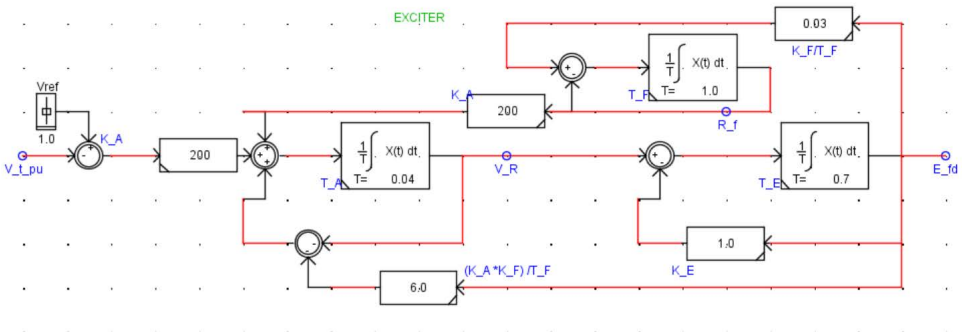

(c) RTDS Draft 4.006.2 excitation system implementation.

Parameter		Per unit value
K_A	Pilot exciter gain	200
K_E	Main exciter gain	1.00
K_F	Rate feedback amplifier gain	0.03
T_A	Pilot exciter time constant	0.04
T_E	Main exciter time constant	0.70
T_F	Rate feedback amplifier time constant	1.00
V_{ref}	Pilot exciter reference voltage	1.012

(d) Excitation system parameters.

Figure 5.16: RTDS Draft 4.006.2 exciter, implementing the exciter equations and parameter values in Fig. 2.10.

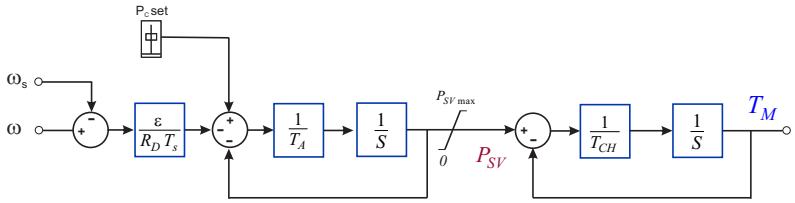

(a) Mechanical control system schematic diagram.

(5.63) $$T_{CH}\frac{dT_M}{dt} = -T_M + P_{SV}$$ **Single Stage Turbine Model**

(5.64) $$T_{SV}\frac{dP_{SV}}{dt} = -P_{SV} + P_C - \frac{\varepsilon}{R_D T_s}\omega_t$$ **Governor Model**

(5.65) $$0 \le P_{SV} \le P_{SV}^{\max}$$

(b) Mechanical control system equations.

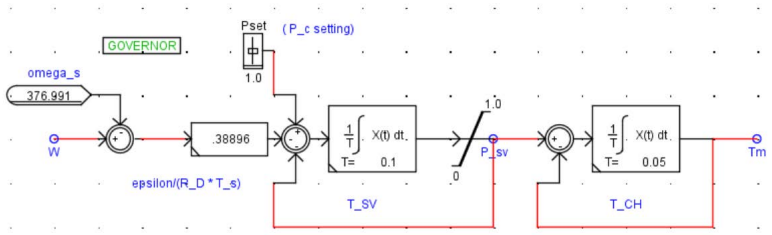

(c) RTDS Draft 4.006.2 mechanical control system implementation.

Parameter		Per unit value
T_{CH}	Steam chest time constant	0.05
T_s	Shaft mechanical time constant	0.1363
T_{FW}	Torque—friction and windage opposing prime mover;	0.0
T_{SV}	Steam valve time constant	0.10
R_D	Speed regulation quantity – also known as “droop” factor	0.05
P_C	Power change setting	0.255
ε	1 / ω_s	$\frac{1}{377\ (\text{rad/s})}$

(d) Mechanical control system parameters.

Figure 5.17: RTDS Draft 4.006.2 exciter, implementing the exciter equations and parameter values in Fig. 2.11.

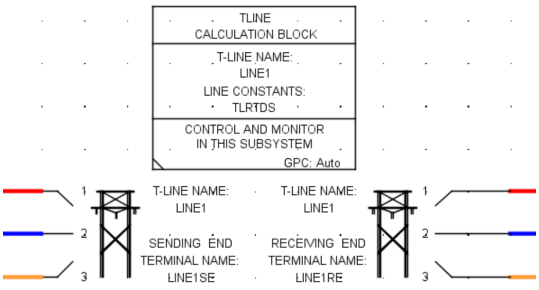

(a) Component model.

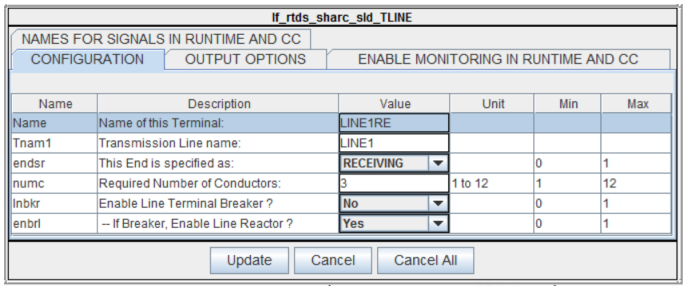

(b) Configuration menu.

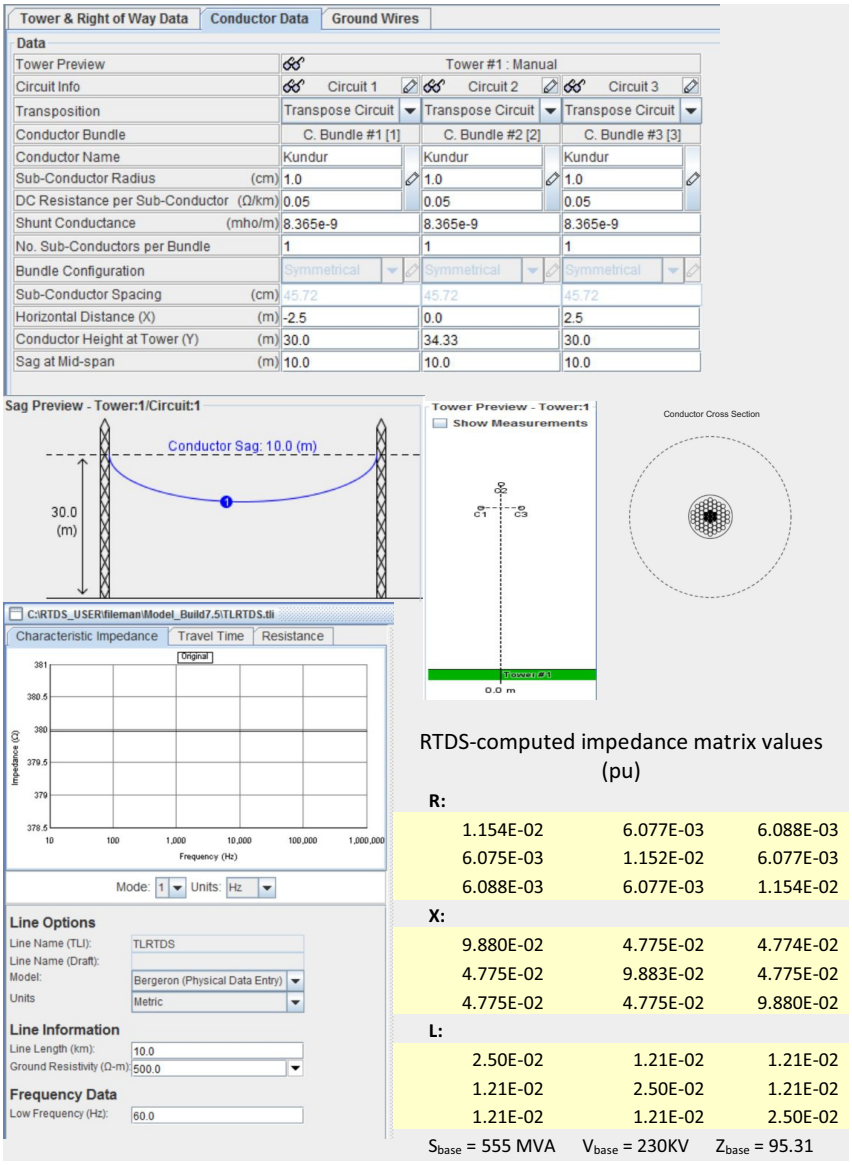

(c) Conductor configuration and computed transmission line parameters for identical transmission lines TL-1 and TL-2.

Figure 5.18: RTDS TLine v2 (2014), model lf_rtds_sharc_sld_TLine.

the disturbance is initiated using the red "Seq/Trigger" button in the lower left-hand corner. The simulation has a built-in delay of approximately 2 s after the "Seq/Trigger" button is pressed to accumulate pre-event steady-state data. The current flows in TL-1 and at the breaker adjacent to the generator's terminal connection are shown in Fig. 5.19.

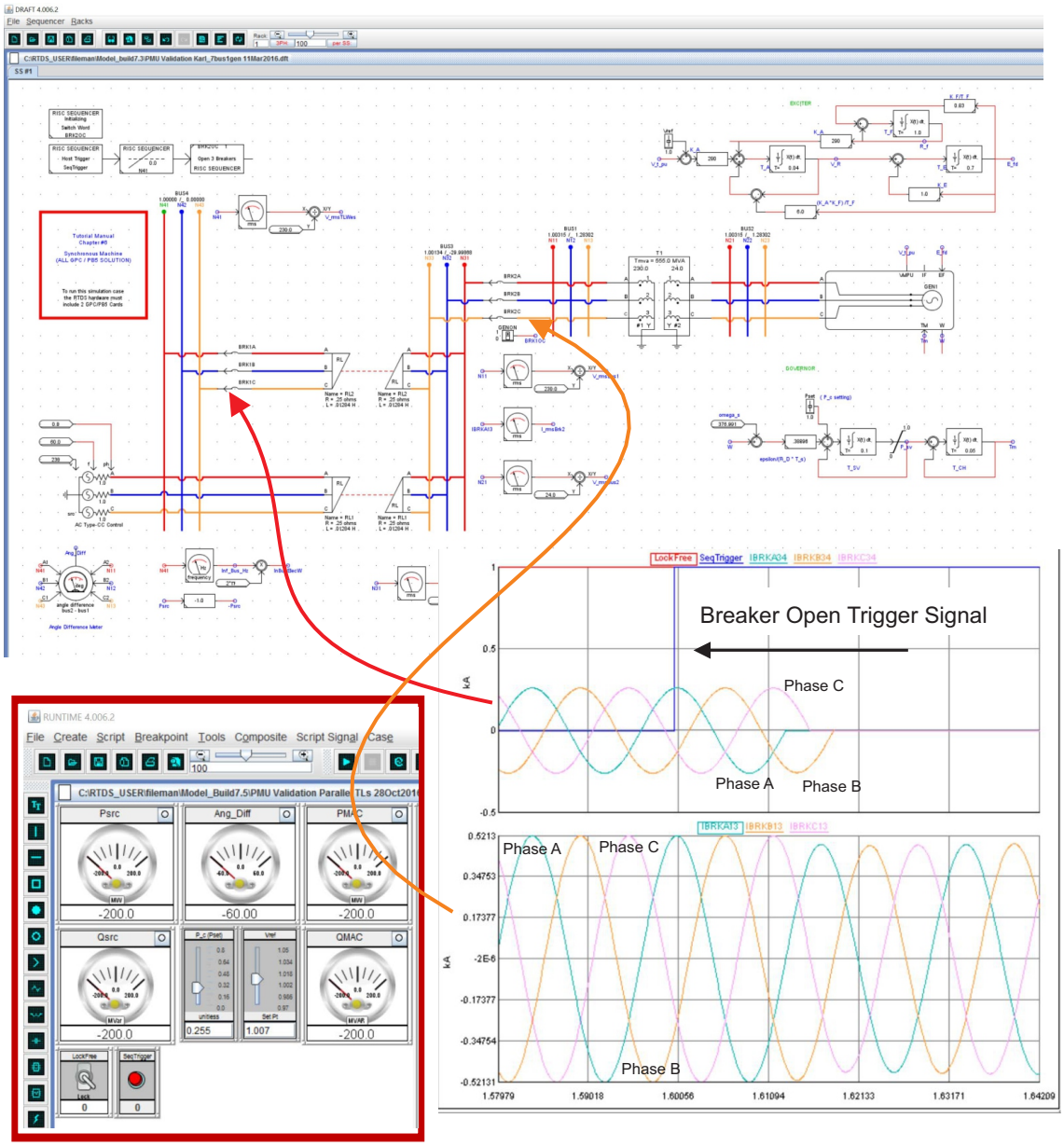

Figure 5.19: RTDS Runtime 4.006.2 controls and meters. RTDS current flows in the *abc* reference frame. The upper graph shows the TL-1 phase currents. The "a-phase" line opens when the current passes through 0.0 the second time. The lower plot shows the breaker current flows at the generator's terminal connections.

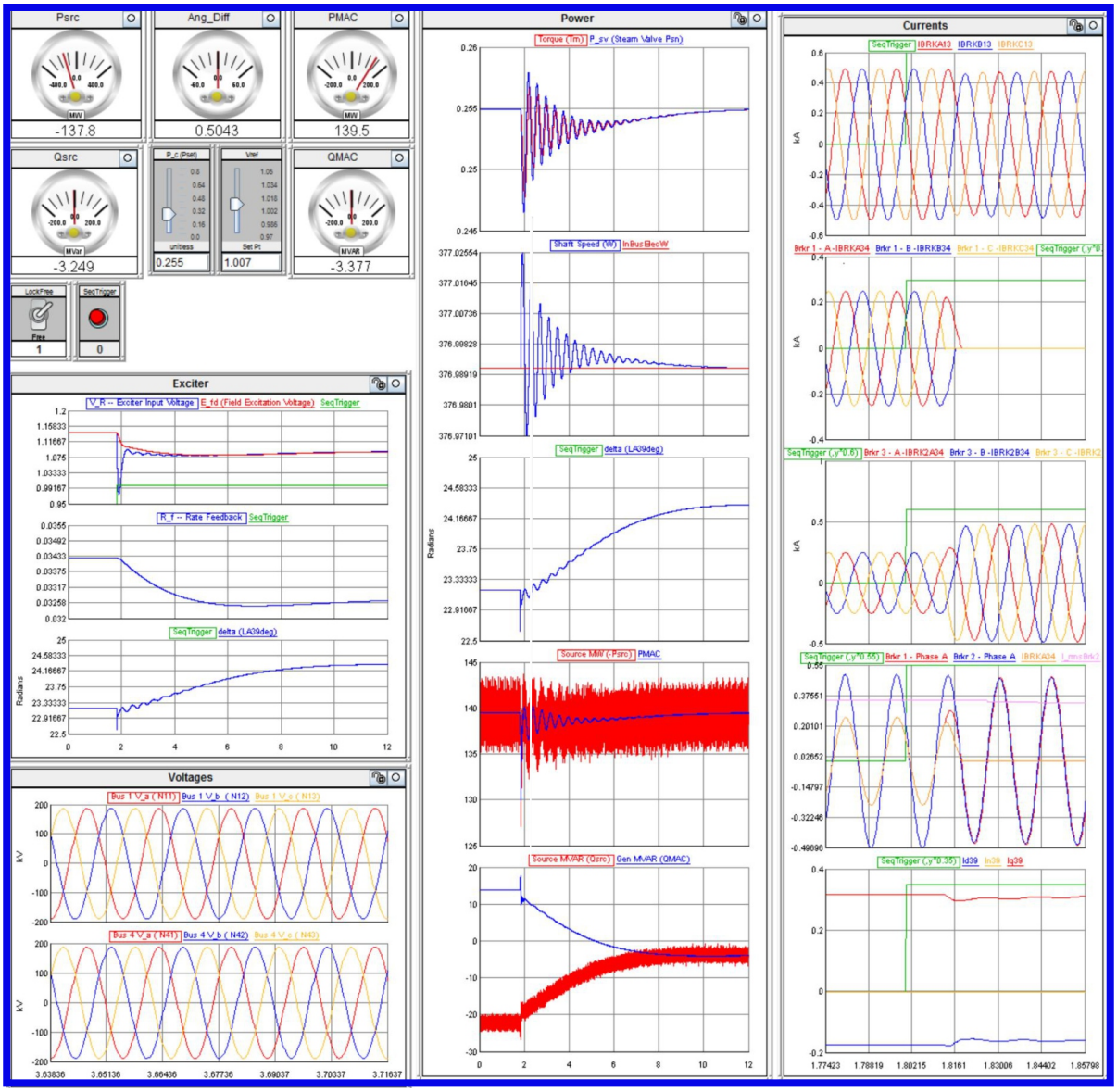

Figure 5.20: RTDS Runtime 4.006.2 control and simulation interface and data plots (1 of 2).

The full RTDS simulation output is shown in Figs 5.20 and 5.21.

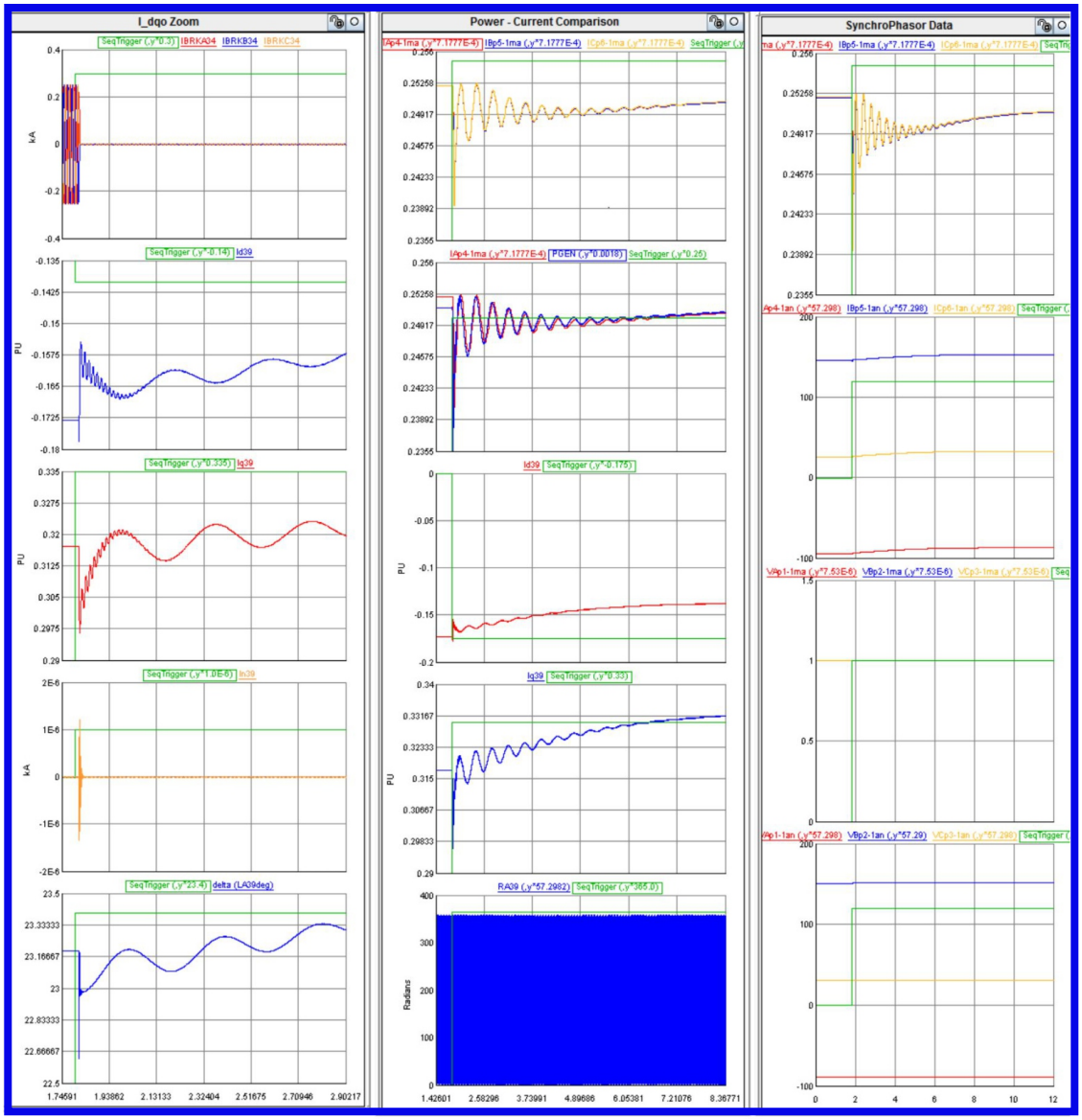

Figure 5.21: RTDS Runtime 4.006.2 control and simulation data plots (2 of 2).

5.4 Synchrophasor Results Analysis

The RTDS generated synchrophasor data plots are shown in Fig. 5.22. The plots show that the PMU measurements capture the disturbance event as evident in the current and voltage magnitude oscillations. The phase current (I_a, I_b, and I_c) magnitudes are essentially equal except immediately after the disturbance event when slight step differences are apparent.

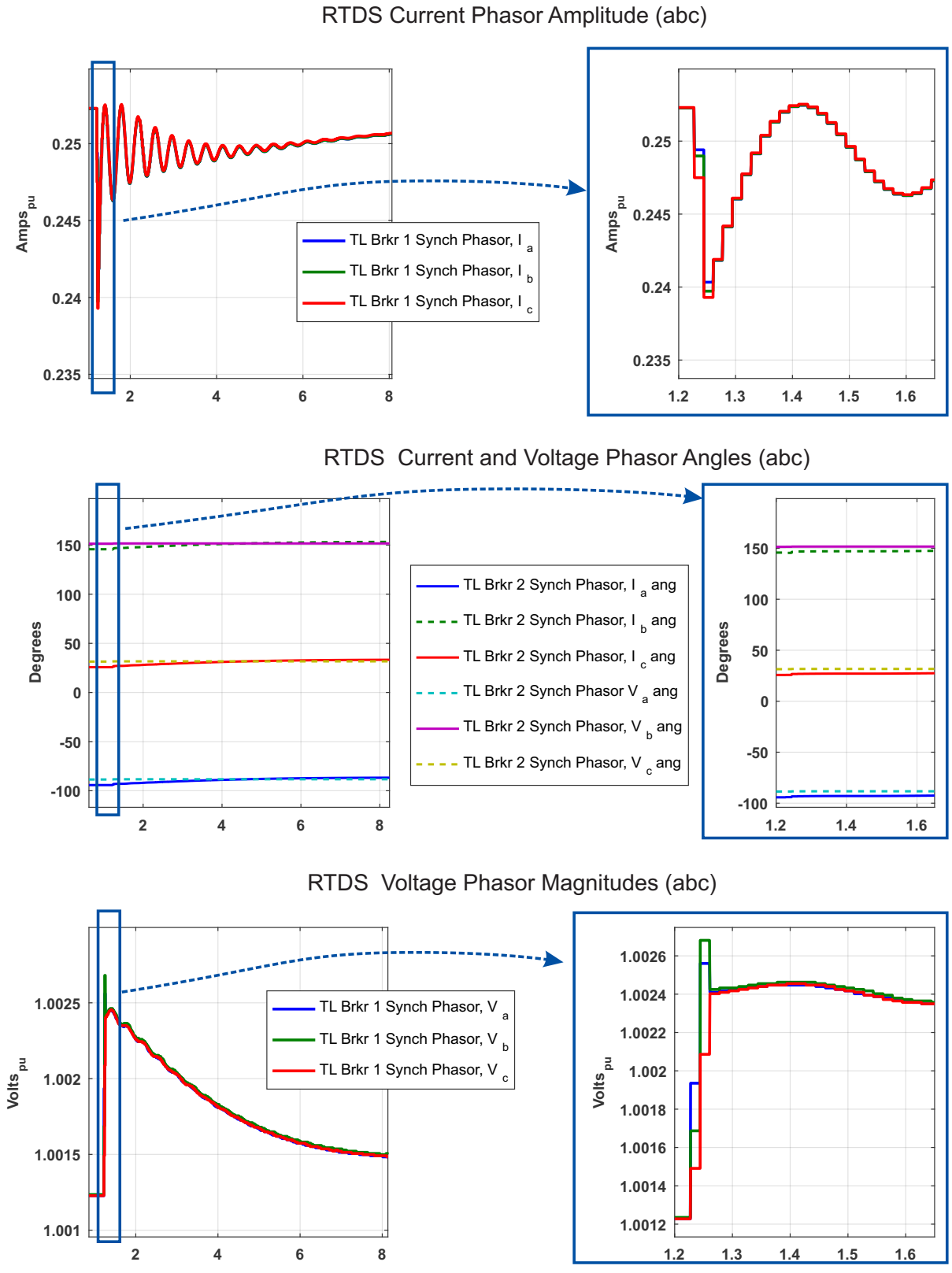

Figure 5.22: RTDS generated synchrophasor data.

Similarly, the three phase voltage (V_a, V_b, and V_c) magnitudes are also essentially equal except immediately after the disturbance event when slight step differences are apparent. As expected for a system operating at the surge impedance load (140 MW), the respective current and voltage phase angles are essentially identical. Also noteworthy is that neither the current nor the voltage phase capture the disturbance event.

From the plot overlaying current and power in per unit in second and third columns in Fig. 5.21, we observe that the current phasor magnitude oscillation tracks the systems real power oscillations. This indicates that PMU has indeed filtered out the higher frequency oscillations observed in the MATLAB simulation.

Chapter 6

Conclusions

This dissertation reports three investigative efforts exploring new ways of assessing power system stability with deliberate intent to leverage synchrophasor measurements. This concluding chapter briefly recaps the thesis and highlights key contributions. The first two efforts addressed power system steady-state stability – specifically methods for assessing system vulnerabilities arising from the phase angle difference between two buses connected by a transmission line. The third effort investigated a commercial PMU's synchrophasor measurements of a simulated disturbance of a single-machine, infinite bus system.

6.1 Contingency Factors

The first line of investigation extended existing steady-state distribution factor theory by developing the Line Outage Angle Factor (LOAF). Existing distribution factors (e.g. Line Outage Distribution Factor (LODF)) provided a computationally light linear method for estimating system-wide transmission line power flow changes as bus power injections (generation) and draws (loads) changed. The LOAF provides a computationally light linear approach to estimating system-wide bus angle difference changes (between transmission line-connected buses) when a transmission line is suddenly removed from service; bus power injections and draws are assumed to remain constant. The LOAF is particularly useful for transmission line loss contingency analysis – and in particular screening for transmission lines that, if lost from service, might cause unacceptable bus angle differences that jeopardize system stability. Contingency analysis using the LOAF distribution factors requires a

single base-case load flow analysis. From the base case, the power flow changes consequent to a transmission line loss can be calculated for any or all transmission lines based upon the full load flow analysis. The efficacy of LOAF-based contingency analysis was assessed using the WSCC 3-Machine, 9-bus Test System. The computed bus angle differences across transmission line-connected buses computed by LOAF distribution factors and full load flow solutions tracked closely. However, the computational effort using the LOAF distribution factors was an order of magnitude smaller than a full power flow solution – a clear advantage when computing a large number of line outage contingencies.

6.2 Thevenin Equivalents

The second investigative line explored developing a Thevenin equivalent model to be used in tandem with synchrophasor data streams to provide real-time bus angle difference information for buses connected by a transmission line. This effort explored multiple approaches.

First, we explored using real-world synchrophasor data from two buses connected by a transmission line. To fully determine the system mathematically, sequential current and voltage synchrophasor measurements from both buses were required. While this system can be mathematically modeled, the approach is limited by the nature of the data. The differences between sequential data pair values was so small that the numerical solution produced unacceptably erratic Thevenin equivalent parameter values. The resulting matrix condition numbers were on the order of 10^5 (1 is ideal), too high to reasonably expect a usable solution. Using multiple data sets to produce least square estimates of the Thevenin equivalent circuit parameters failed to significantly improve the quality of the results. We found that this approach to delivering the desired Thevenin equivalent works well on paper, but is problematic using real-world synchrophasor data. We concluded that the nature of synchrophasor data does not support computation from sequential measurements because of the very small differences between measurement values.

Next, we made model simplifying assumptions: (i) Thevenin equivalent source magnitudes constrained to 1 pu and (ii) transmission line resistance assumed to be zero. This approach involved algebraic manipulation of the system equations to solve for the remaining unknowns: the Thevenin source voltage angles and reactance at both buses. As the equation set involved quadratic equations at both buses, the solution set resulted in four possible solutions. However, sample calculations from real-world synchrophasor data showed that only one of the four solutions was consistent with other model constraints, i.e. power flow from bus 1 to bus 2 requires that $\delta_1 > \theta_1 > \theta_2 > \delta_2$. Beyond selecting the physically appropriate solution, this model was consistent with expected system behavior in every respect. The solution satisfied three KVL loop equations with small residuals – one through each source and its corresponding terminals and a loop around the total system. Additionally, the real and reactive powers computed at each source and terminal were consistent with expected real and reactive power flows. Further, the Thevenin equivalent solution showed results that varied no more quickly than the phasor measurements. Consequently, this model and Thevenin equivalent computational approach warrant further investigation for applications assessing power system stability.

The third approach endeavored to use a power flow solution-based Thevenin equivalent. A hybrid simulation using MATLAB in combination with PowerWorld via the Simulator Automation Server (SimAuto) data component object module was written to generate a series of power flow solutions emulating synchrophasor data at different system operating points. The test system was PowerWorld Corporation's 7-bus system (B7Flat). This simulation design enabled exploring the test system solution space to observe Thevenin equivalent solution evolution as the generations and loads were progressively increased until PowerWorld failed to find a solution. This approach delivered encouraging results on the test system. The closing effort along these lines examined using a Monte Carlo approach to introducing multiple random variations at power set points to evaluate the Thevenin equivalent sensitivity to local set point variations. Low sensitivities are necessary to validate that the inherently linear

Thevenin equivalent model (i) is useful in predicting bus voltage angle differences across a transmission line, (ii) is useful computing a Thevenin equivalent based upon variations about the normal system operating point, and (iii) shows acceptably linear behavior as the system is stressed to the point of failure. The Thevenin equivalents developed using the power flow solution Monte Carlo method show promise, but require further investigation to draw definitive conclusions.

6.3 Synchrophasor Data from Machine Transient Response

The third line of investigation sought to understand, from a practical perspective, the information that can be extracted from synchrophasor data streams produced during a synchronous generator's transition between steady-state operating conditions. The test system was a synchronous generator connected to an infinite bus by a pair of identical transmission lines. The disturbance event of interest occurred when one transmission line is suddenly opened, chosen because the system includes the phenomena of interest and the level of effort required to code a simulation is reasonable. To span the range from the strict mathematical model to the physical world the system was simulated using MATLAB and the Real-Time Digital Simulator (RTDS).

The MATLAB simulation was entirely our own work leveraging MATLAB based computational tools, which afforded complete control and knowledge of the code's inner workings. The simulation produced results consistent with expected system behavior. Significantly, the MATLAB simulation clearly showed the relationship between the three-damper-winding (14 dynamic states) and the reduced order model (11 dynamic states) simulation results. The overlayed simulation results clearly illustrate that the integral manifold approach to model reduction preserves the system transient response while eliminating the stator winding transients.

In contrast, the RTDS in tandem with the Schweitzer Engineering Laboratory's SEL-421 Protection, Automation, and Control System provided "real-world" synchrophasor data in the controlled laboratory environment. The RTDS simulator down-side is that the component simulation modules are in many respects "black boxes" with internal processes opaque to the user. Using the MATLAB and RTDS in parallel provided the ability to cross-check the simulation results. Considerable effort was expended harmonizing the two simulations so that their simulation results matched. Unfortunately, converging the transmission line models between the simulators was not completely successful. However, that shortfall did not prevent drawing useful conclusions from the simulation. We found that the RTDS-generated synchrophasor data stream was similar to the MATLAB reduced order model voltage and current generator terminal data in the *dqo* reference frame – reflecting parallel, but distinct, filtering processes. We also found that the PMU synchrophasor data filtered out many of the system oscillations observable in the MATLAB simulation.

References

[1] "Final report on the August 14, 2003 blackout in the United States and Canada: Causes and recommendations," Apr 2004. [Online]. Available: http://energy.gov/sites/prod/files/oeprod/DocumentsandMedia/BlackoutFinal-Web.pdf

[2] K. H. LaCommare and J. H. Eto, "Cost of power interruptions to electricity consumers in the United States (US)," *Energy*, vol. 31, no. 12, pp. 1845–1855, 2006.

[3] K. Moslehi and R. Kumar, "Smart grid - a reliability perspective," in *Proc. Innovative Smart Grid Technologies (ISGT)*, 2005, pp. 1–8.

[4] "Section 1301, Energy Independence and Security Act (EISA) of 2007 [Public Law 110-140-Dec 19, 2007]." [Online]. Available: http://www.oe.energy.gov/DocumentsandMedia

[5] D. Von Dollen, "Report to NIST on the smart grid interoperability standards roadmap," prepared by the Electric Power Research Institute, Tech. Rep., 2009.

[6] "2014 smart grid system report," August 2014, U.S. Department of Energy, accessed 11.11.2016. [Online]. Available: http://energy.gov/sites/prod/files/2014/08/f18/SmartGrid-SystemReport2014.pdf

[7] C. Gellings, "Estimating the costs and benefits of the smart grid," Electric Power Research Institute (EPRI), Tech. Rep., 2011.

[8] Smart Grid Interoperability Panels, "Introduction to NIST interagency report (NISTIR) 7628, guidelines for smart grid cyber security," 2010.

[9] H. Sandberg, A. Teixeira, and K. H. Johansson, "On security indices for state estimators in power networks," in *First Workshop on Secure Control Systems (SCS), Stockholm, 2010*, 2010.

[10] "Phasor measurement units in the North American power grid," Mar 2015, Internet, North American Synchrophasor Initiative (NASPI) Working Group. [Online]. Available: https://www.naspi.org/documents

[11] A. P. J. Thorp, *Synchronized Phasor Measurements and Their Applications*. Springer Science+Business Media, LLC, 2008.

[12] *IEEE Standard for Synchrophasor Measurements for Power Systems*, IEEE Std., Dec. 2011.

[13] F. F. Wu, K. Moslehi, and A. Bose, "Power system control centers: Past, present, and future," *Proceedings of the IEEE*, vol. 93, no. 11, pp. 1890–1908, 2005.

[14] C. A. MacArthur, "Transmission limitations computed by superposition," *Transactions of the American Institute of Electrical Engineers. Part III: Power Apparatus and Systems*, vol. 80, no. 3, pp. 827–831, Apr. 1961.

[15] P. W. Sauer, "On the formulation of power distribution factors for linear load flow methods," *IEEE Transactions on Power Apparatus and Systems*, vol. PAS-100, no. 2, pp. 764–770, Feb. 1981.

[16] A. Wood and B. Wollenberg, *Power Generation Operation and Control (2nd Edition)*. John Wiley & Sons,, 1996.

[17] Y. C. Chen, A. D. Domínguez-García, and P. W. Sauer, "Online computation of power system linear sensitivity distribution factors," in *Proc. IREP Symp. Bulk Power System Dynamics and Control - IX Optimization, Security and Control of the Emerging Power Grid (IREP)*, Aug 2013, pp. 1–4.

[18] Y. C. Chen, A. D. Domínguez-García, and P. W. Sauer, "Measurement-based estimation of linear sensitivity distribution factors and applications," *IEEE Transactions on Power Systems*, vol. 29, no. 3, pp. 1372–1382, May 2014.

[19] F. Aminifar, M. Fotuhi-Firuzabad, A. Safdarian, A. Davoudi, and M. Shahidehpour, "Synchrophasor measurement technology in power systems: Panorama and state-of-the-art," *IEEE Access*, vol. 2, pp. 1607–1628, Jan. 2014.

[20] A. G. Phadke, "Synchronized phasor measurements-a historical overview," in *Proc. Transmission and Distribution Conf. and Exhibition 2002: Asia Pacific. IEEE/PES*, vol. 1, Oct. 2002, pp. 476–479 vol.1.

[21] R. Gutman, P. P. Marchenko, and R. D. Dunlop, "Analytical development of loadability characteristics for EHV and UHV transmission lines," *IEEE Transactions on Power Apparatus and Systems*, vol. PAS-98, no. 2, pp. 606–617, Mar. 1979.

[22] D. H. Johnson, "Origins of the equivalent circuit concept: the current-source equivalent," *Proceedings of the IEEE*, vol. 91, no. 5, pp. 817–821, May 2003.

[23] K. J. Reinschke, "On network models and the symbolic solution of network equations," *Applied Mathematics and Computer Science*, vol. 11, no. 1, pp. 237–270, 2001.

[24] R. Hashemian, "Hybrid equivalent circuit, an alternative to Thevenin and Norton equivalents, its properties and applications," in *Proceedings Midwest Symposium on Circuits and Systems*, Aug. 2009, pp. 800–803.

[25] W. F. Pickard, "Nonlinear equivalent circuits for membranes," *Journal of Mathematical Biology*, vol. 21, no. 1, pp. 11–23, 1984.

[26] L. Ljung, "Perspectives on system identification," *Annual Reviews in Control*, vol. 34, no. 1, pp. 1–12, Apr. 2010.

[27] Z. Zhang, "Parameter estimation techniques: A tutorial with application to conic fitting," *Image and Vision Computing*, vol. 15, no. 1, pp. 59–76, 1997.

[28] K. Baker, "Singular value decomposition tutorial," Mar. 2005. [Online]. Available: https://www.researchgate.net/profile/Kirk_Baker/publication/246546380_Singular_Value_Decomposition_Tutorial/links/0912f512181fbbd809000000.pdf

[29] J. Shlens, "A tutorial on principal component analysis, 2005," 2010.

[30] S. Abdelkader, "Online Thevenin equivalent using local PMU measurements," in *International Conference on Renewable Energies and Power Quality*, Las Palmas de Gran Canaria (Spain), Apr. 2010, pp. 1–4.

[31] S. M. Abdelkader and D. J. Morrow, "Online tracking of Thevenin equivalent parameters using PMU measurements," *IEEE Transactions on Power Systems*, vol. 27, no. 2, pp. 975–983, May 2012.

[32] K. Vu, M. M. Begovic, D. Novosel, and M. M. Saha, "Use of local measurements to estimate voltage-stability margin," *IEEE Transactions on Power Systems*, vol. 14, no. 3, pp. 1029–1035, Aug. 1999.

[33] J. H. Liu and C. C. Chu, "Short-term voltage instability detections of wind generators using synchrophasors," in *Proceedings of the IEEE Power Engineering Society General Meeting*, Jul. 2014, pp. 1–5.

[34] S. J. S. Tsai and K. H. Wong, "Adaptive undervoltage load shedding relay design using Thevenin equivalent estimation," in *Proceedings of IEEE Power and Energy Society General Meeting*, Jul. 2008, pp. 1–8.

[35] P. Zhang, L. Min, and N. Zhang, "Method for voltage stability load shedding using local measurements," U.S. Patent 7 603 203, Oct 13, 2009. [Online]. Available: https://www.google.com/patents/US7603203

[36] R. Alammari, "Voltage stability margin identification using local measurements and linear Kalman filter," *Engineering Journal of the University of Qatar*, vol. 15, pp. 153–164, 2002.

[37] S. J. Tsai and K. H. Wong, "On-line estimation of Thevenin equivalent with varying system states," in *Proceedings of the IEEE Power and Energy Society General Meeting*, 2008, pp. 1–7.

[38] R. K. Mai, Z. Y. He, L. Fu, B. Kirby, and Z. Q. Bo, "A dynamic synchrophasor estimation algorithm for online application," *IEEE Transactions on Power Delivery*, vol. 25, no. 2, pp. 570–578, Apr. 2010.

[39] T. An, S. Zhou, J. Yu, W. Lu, and Y. Zhang, "Research on illed-conditioned equations in tracking Thevenin equivalent parameters with local measurements," in *Proceedings of the 2006 International Conference on Power System Technology.* IEEE, 2006, pp. 1–4.

[40] A. G. Phadke and B. Kasztenny, "Synchronized phasor and frequency measurement under transient conditions," *IEEE Transactions on Power Delivery*, vol. 24, no. 1, pp. 89–95, Jan. 2009.

[41] S. Das and T. Sidhu, "Detecting synchrophasors computed over fault/switching transients," *IET Generation, Transmission & Distribution*, vol. 8, no. 9, pp. 1616–1625, 2014, Institution of Engineering and Technology (IET).

[42] S. Das and T. Sidhu, "Robust algorithm to estimate fault synchrophasor from fault-transient synchrophasor in phasor data concentrator," *IET Generation, Transmission, and Distribution*, vol. 9, no. 2, pp. 124–132, 2015, Institution of Engineering and Technology (IET).

[43] P. W. Sauer and M. Pai, *Power System Dynamics and Stability.* Prentice Hall, 1998.

[44] P. M. Anderson and A. A. Fouad, *Power System Control and Stability.* Iowa State University Press, 1997.

[45] P. C. Krause, O. Wasynczuk, and S. D. Sudhoff, *Analysis of Electric Machinery and Drive Systems*, 2nd ed. John Wiley & Sons, 2002.

[46] P. W. Sauer, S. Ahmed-Zaid, and P. V. Kokotovic, "An integral manifold approach to reduced order dynamic modeling of synchronous machines," *IEEE Transactions on Power Systems*, vol. 3, no. 1, pp. 17–23, Feb. 1988.

[47] P. V. Kokotovic and P. W. Sauer, "Integral manifold as a tool for reduced-order modeling of nonlinear systems: A synchronous machine case study," *IEEE Transactions on Circuits and Systems*, vol. 36, no. 3, pp. 403–410, Mar. 1989.

[48] I. A. Hiskens, "Nonlinear dynamic model evaluation from disturbance measurements," in *IEEE Transactions on Power Systems*, vol. 16, no. 4, Nov. 2001, pp. 702–710.

[49] Z. Huang, P. Du, D. Kosterev, and S. Yang, "Generator dynamic model validation and parameter calibration using phasor measurements at the point of connection," *IEEE Transactions on Power Systems*, vol. 28, no. 2, pp. 1939–1949, May 2013.

[50] J. J. Grainger and W. D. Stevenson, *Power System Analysis.* McGraw-Hill, 1994.

[51] O. I. Elgerd, *Electric Energy Systems Theory: An Introduction.* McGraw-Hill, 1982.

[52] P. Kundur, N. J. Balu, and M. G. Lauby, *Power System Stability and Control*. McGraw-Hill New York, 1994.

[53] P. Sauer, "Applications of integral manifolds to power system studies," *Mathematical and Computer Modelling*, vol. 11, pp. 317 – 320, 1988. [Online]. Available: http://www.sciencedirect.com/science/article/pii/0895717788905067

[54] P. W. Sauer, K. E. Reinhard, and T. J. Overbye, "Extended factors for linear contingency analysis," in *Proc. 34th Annual Hawaii Int System Sciences Conf*, Jan. 2001, pp. 697–703.

[55] B. Stott and O. Alsac, "Fast decoupled load flow," *IEEE Transactions on Power Apparatus and Systems*, vol. PAS-93, no. 3, pp. 859–869, May 1974.

[56] K. E. Reinhard, P. W. Sauer, and A. D. Dominguez-Garcia, "On computing power system steady-state stability using synchrophasor data," in *Proceedings of the 46th Hawaii International Conference on System Sciences*. IEEE, Jan. 2013, pp. 2312–2318.

[57] H. P. St. Clair, "Practical concepts in capability and performance of transmission lines," *Part III Power Apparatus and Systems Transactions of the American Institute of Electrical Engineers*, vol. 72, no. 2, pp. 1152–1157, Dec. 1953.

[58] T. He, S. Kolluri, S. Mandal, F. Galvan, and P. Rastgoufard, *Applied Mathematics for Restructured Electric Power Systems: Optimization, Control, and Computational Intelligence*. Springer Science and Business Media, Inc., 2005, ch. Identification of Weak Locations in Bulk Transmission Systems Using Voltage Stability Margin Index, pp. 25–37.